Liquid Interface Deposition of Thin Films and van derWaals Heterostructures of Two-Dimensional Solids

MUHAMMAD ZULQURNAIN

CONFIDENTIAL INFORMATION

RESEARCH MASTERS THESIS

Liquid Interface Deposition of Thin Films and van der Waals Heterostructures of Two-Dimensional Solids

Author:
Muhammad ZULQURNAIN

Supervisors:
Dr. Michael HUNT and
Dr. Marek SZABLEWSKI

A thesis submitted in fulfillment of the requirements for the degree of Master of Science by Research

in the

Centre for Material Physics

November, 2017

Declaration of Authorship

I, Muhammad ZULQURNAIN, declare that this thesis titled, "Liquid Interface Deposition of Thin Films and van der Waals Heterostructures of Two-Dimensional Solids" and the work presented in it are my own. I confirm that:

- This work was done wholly while in candidature for a research degree at this University.
- I have acknowledged all main sources of assistance.
- Where the thesis is based on work done by myself jointly with others, I have made clear exactly what was done by others and what I have contributed myself.

"Width of life is more important than its length."

Ibn e Sina (Avicenna)

University of Durham

Abstract

Centre for Material Physics

Master of Science by Research

Liquid Interface Deposition of Thin Films and van der Waals Heterostructures of Two-Dimensional Solids

by Muhammad ZULQURNAIN

The scalable production of thin films of graphene and other two-dimensional materials is a key research challenge which needs to be addressed if the unique and desirable properties of these materials is to be exploited beyond the laboratory. In this report a brief overview of two-dimensional layered materials, their production and of heterostructures produced from them is presented. Experiments exploring the time and temperature dependence of shear exfoliation for the production of graphene suspensions, a key precursor for thin film and heterostructure fabrication are reported. It is concluded that, for shear exfoliation of graphene in an aqueous surfactant solution of Triton X-100 and ultra-high purity water, the graphene platelets formed consist predominantly of three layers (trilayer graphene). Data indicate that there is an initial decrease in platelet laterial size with exfoliation time, with the size then remaining constant (albeit with considerable scatter in the data). Preliminary measurements indicate that temperature is also found to influence shear exfoliation through viscosity of the solvent. Increasing viscosity is found to initially increase the concentration of shear exfoliated suspensions until the viscosity increases to a point where the minimum shear rate required for exfoliation cannot be met by the mixer employed, at which point exfoliation is suppressed and concentration decreases. Raman spectroscopy was employed to demonstrate that the shear exfoliation approach used for graphene was also applicable to MoS_2, $MoSe_2$ and WS_2. Langmuir-Blodgett deposition was used to deposit thin films of graphene, but the resultant films were found to be non-uniform and it was not possible to produce films from few layer transition metal dichalcogenides (TMDCs) by this route. To address this issue, a new technique was developed, termed 'Liquid Interface Deposition' (LID), which is described. The generic nature of the LID approach is demonstrated through the presentation of data from thin films derived from few layer suspensions of graphene, TMDCs and hexagonal boron nitride. A mechanism of thickness control is applied to films derived from suspensions of graphene trilayers, and films ranging from ~1 to ~5 trilayer units produced. The use of LID for the fabrication of heterostructures is demonstrated through the production of a graphene/MoS_2 heterostructure characterised by Raman and optical spectroscopies.

Acknowledgements

I am highly thankful to my supervisors **Dr Michael Hunt** and **Dr Marek Szablewski**, whose unconditional support and guidance always remained there for me. Without their encouragement and belief in my abilities, it wouldn't be possible produce the best work of my life. I will always be indebted to my colleagues *Mr Angus Mathieson, Miss Alina Talmantaite, Miss Aqsa Arshad, Mrs Taghreed al Sulaami and Mr Waris Ali*, whose support will endure as a precious asset for me. I would also express my gratitude to all of the technicians of the mechanical and electrical workshops for their assistance in the construction of the 3D motorised stage for the Raman spectrometer.

I am also grateful to my wife **Mrs Noseeqa Zulqurnain**. Her patience, care and support is a great share of this work. I will be thankful to all of those who have supported me in any way to produce this work and made it possible for me to contribute original knowledge to the vast field of science.

Contents

List of Figures

List of Tables

This work is dedicated to my parents, without their prayers it was certainly impossible to create such work. May they live long!

Chapter 1

Introduction to Graphene and other Two-Dimensional Materials

1.1 Introduction

Since its isolation in 2004, graphene has become one of the most studied nanomaterials [1]. It was originally thought that 2D materials cannot exist physically due to a rapid decrease in melting point with decreasing thickness leading to instability [2] as described by the Mermin-Wagner theorem [3, 4]. It was believed that such single crystalline layers existed only within bulk materials or could be grown upon matching crystal lattices (epitaxial growth) [5, 6]. However, in 2004, single layers of graphene were isolated by Geim and Novoselov [1], thus providing the missing piece in the puzzle of nanostructured carbon and resulted in the award of the Nobel Prize for Physics in 2010 [7]. This discovery revived the interest of researchers in the investigation of a whole family of layered materials analogous to graphene [8]. These materials include transition metal dichalcogenides (TMDCs) with stoichiometry MX_2, which consist of metal (M) atoms such as Mo, W, Nb, Re, Ni, or V etc; sandwiched between the chalcogen (X) atoms of S, Se, or Te [9], transition metal oxides such as MoO_3, La_2CuO_4, and vanadium oxide derivatives [10–12], insulating hexagonal boron nitride (*h*-BN) [13, 14], topological insulators such as Bi_2Te_3, Bi_2Se_3, Sb_2Te_3 and Sb_2Se_3 [15–18], metal monochalcogenides (MX: where M=Sn, Fe, Pb, Ge or Ga and X=O, S, Se or Te) [19–23], and other group IV-VI materials analogous to graphene such as silicene, germanene, stanene, and phosphorene [24–27]. In naturally occurring materials in this group there is a common bulk 3D structure made up of individual layers, which are stacked on top of each other, having van der Waals interactions between adjacent sheets and strong covalent bonding between the atoms of same layer. Their electronic structure is representative of all types of materials from insulators to superconductors [8].

The restriction of one of the dimensions of a bulk material to the nanoscale is responsible for the significantly different and distinct properties of 2D materials as compared with their corresponding bulk 3D "parent" materials [28]. The absence of interlayer forces, the geometry effect, and quantum confinement results in changes to their thermal [29] and electrical

conductivity, mechanical strength, chemical structure and optical properties [28, 30]. Furthermore, an exciting feature of these 2D materials is the 'possibility of tuning their properties', by applying external electric or magnetic fields, controlling the number of layers, or by fabricating new types of materials called van der Waals heterostructures, Figure1.1. By combining 'selected properties' of these solids by stacking monolayers of different 2D materials we can obtain purpose built structures with predetermined attributes and functionalities, to use in various applications and devices [31, 32]. The properties of such materials can be exploited in applications including optoelectronic devices [33], spintronics [8], catalysts [8], chemical and biological sensors [34], absorber materials for solar cells [32], supercapacitors [35] and lithium ion batteries[8]. We will discuss some of these materials and their properties in detail in this chapter.

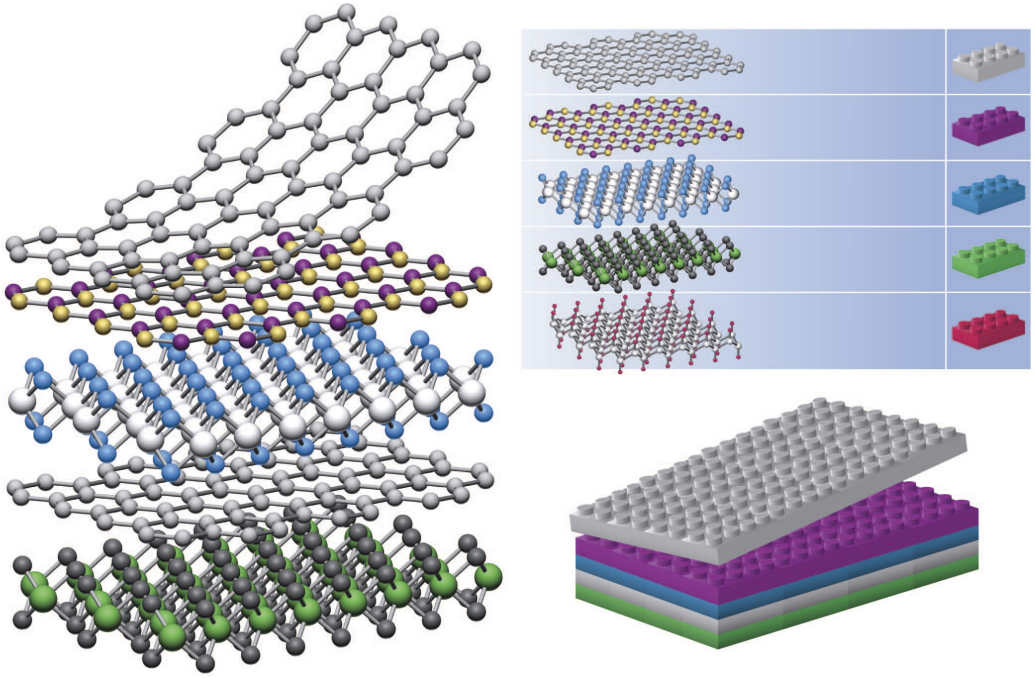

FIGURE 1.1: *Schematic of a van der Waals Heterostructure: The figure illustrates the arrangement of layers of different 2D materials analogous to Lego blocks stacked on top of each other* Image taken from Ref [31].

The production of these thin 2D layered materials (2DLMs) and van der Waals heterostructures (vdWHs) is a huge challenge. Although much effort is directed towards the scalable production of these vdWHs and significant progress has been made [31], fast and cost effective methods of fabrication of vdWHs are still required. Methods such as mechanical exfoliation, liquid phase exfoliation, chemical vapour deposition (CVD), surface segregation [36], and molecular beam epitaxy (MBE) [37] have been developed to acheive this purpose [8]. Furthermore, the transfer of exfoliated material to suitable substrates with fine control over the number of layers and structure is a major problem and is the focus of this work. In particular, a new technique which we term "Liquid Interface Deposition" has

been developed for scalable production of thin films and vdWHs. By adapting this method, industrial scale production will be possible and it will open new horizions for production of tailored functional materials on demand.

1.2 Two Dimensnional Materials

Two-dimensional materials have attracted the attention of many researchers and scientists because of their unique and different properties compared with their 3D counterparts, and their promise of a relatively easy route for assembly of complex nanoelectronic devices and structures like quantum wells, superlattices, multilayers and heterostructures [38]. In 2D materials one of the dimensions is ideally limited to the size of the constituent atoms of that material, however their few-layered structures (up to ≈10 layers) are also classed as 2D materials hence subject of study by nanomaterials' researchers. There are two main types of 2D material, the naturally existing 2D layered structures which can form a part of 3D bulk materials such as graphene, MoS_2, etc., and the 2D layers grown on suitable substrates for example, silicene, germanene, stanene etc.

1.2.1 Graphene

Graphene is a 2D material consisting of a symmetrical lattice of hexagonally arranged carbon atoms connected by strong covalent bonds and commonly referred to as a honeycomb structure. A graphene sheet can be rolled into cylindrical shapes thus forming carbon nanotubes (1D) and wrapped into spheres known as fullerenes (0D), Figure:1.2(a),(b),(c).

Stacked graphene sheets, held together by weak van der Waals interactions form a 3D bulk material known as 'graphite'. A number of different stacking arrangements are possible including hexagonal (AAA), Bernal (ABA), rhombohedral (ABC) and a highly deformed or turbostratic stacking , as shown in figure 1.2 (d),(e),(f) and (g) [42, 43]. The most common arrangement is Bernal (ABA) stacking, in which atoms at the corners of hexagons of one layer are located at vacant centres of hexagons of adjacent layers hence alternate layers are aligned with one another along z-axis resulting in the thermodynamically stable form of graphite [44, 45]. Thus, graphene can be regarded as the fundamental unit of all forms of graphitic material.

One of the earliest studies of the electronic structure of graphene was that of Wallace [46] about 70 years ago, at which point the independent existence of graphene was considered unrealistic because the thermodynamical existence of 2D materials was assumed to be impossible [2, 47]. Such theoretical investigations of the electronic band structure were primarily focussed on providing an understanding of the behaviour of graphite, as it was thought that weak interlayer interactions would not perturb the results obtained from graphene significantly [48, 49].

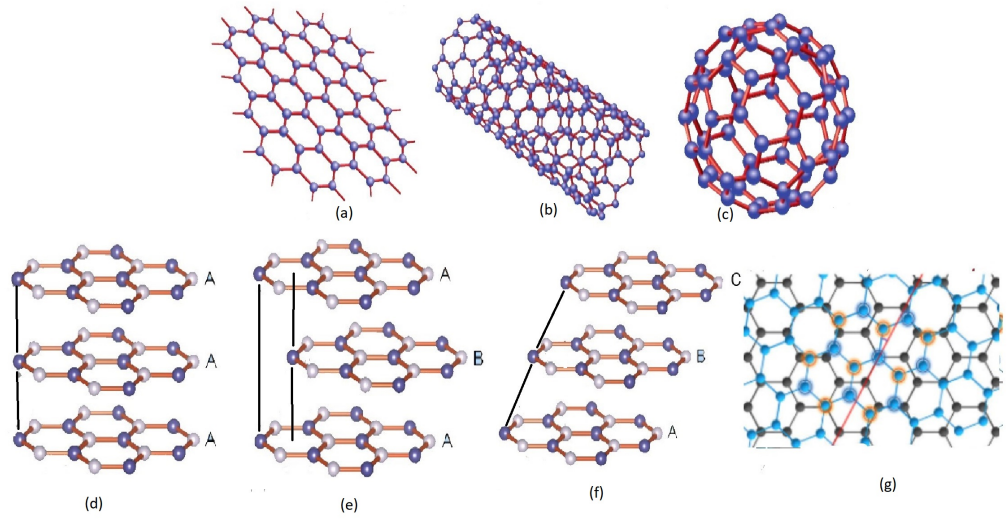

FIGURE 1.2: *Different allotropes of graphitic carbon: (a) A monolayer graphene (b) Cylindrically rolled sheet of graphene forming a 1D carbon nanotube (c) Spherically wrapped graphene sheet (including pentagons to give curvature at specific places in a graphene sheet, forming a 0D structure known as a 'fullerene'. (d) A highly symmetrical orientation of graphite layers with each atom of a nearby plane is in perfect alignment along the z-axis forming an hexagonal arrangement (AAA); (e) the well known Bernal stacking(ABA) arrangement of graphite layers in which every atom in first layer is aligned with corresponding atom in third layer, while adjacent layers are arranged in such a way that vacant centres of hexagons on one layer have a carbon atom from an hexagonal corner of the adjacent layer; (f) In rhombohedral (ABC) stacking of graphite layers the hexagons in each stacked layer are displaced forward resembling a stair, stepping upwards layer by layer resulting every 4^{th} layer aligned to first layer; (g) A top view of randomly rotated and translated layers showing the highly deformed graphitic structure known as turbostratic stacking.* Images adapted from Refs (a)(b)(c) [39], (d)(e)(f) [40], (g) [41].

1.2.1.1 Atomic and electronic structure of graphene

In a graphene layer carbon atoms are placed at each corner of a hexagon and connected by very strong in-plane covalent bonds. In order to understand the structure of graphene, an explanation of the origin of bonding between the constituent carbon atoms is necessary. The superposition of $2s$, $2p_x$ and $2p_y$ orbitals of carbon atoms in graphene results in the three equivalent orbitals (sp^2) and such mixing of orbitals is known as "sp^2 hybridisation". These sp^2 hybridised orbitals in a carbon atom make an angle of 120° with each other giving rise to trigonal planar geometry [50], Figure 1.3(a). The covalent bonds between carbon atoms of graphene are formed by overlapping of these sp^2 hybridised orbitals and referred to as 'σ-bonds', having a bond length of 1.42Å. The sp^2 hybridisation is responsible for the planar geometry of graphene and resulting covalent bonds define the hexagonal arrangement of carbon atoms, Figure 1.3(b), along with providing an extraordinary intra-planar strength to graphene sheets, making it the strongest material in nature [51]. The remaining unhybridised $2p_z$ orbital of each carbon atom, which lies perpendicular to the σ-bonds, overlap with each other forming a delocalised band of filled π orbitals called the valance band and the empty π^* anti-bonding orbital constitutes the conduction band [52].

Each carbon atom in a graphene sheet is shared by three hexagons, thus contributing 1/3 of

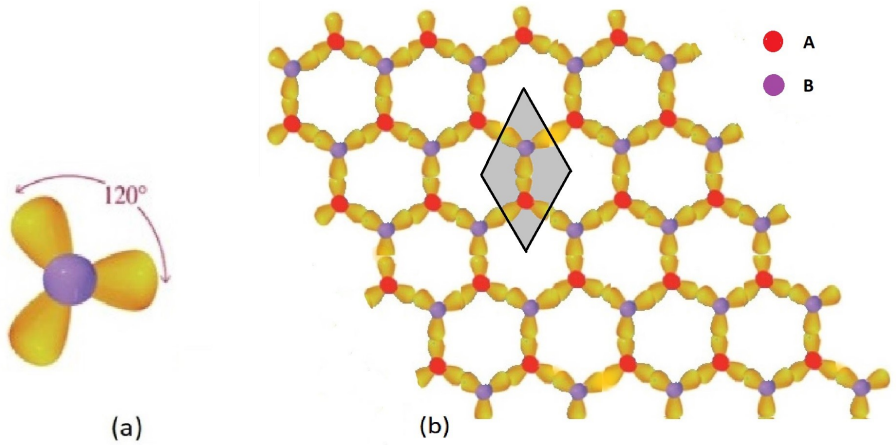

FIGURE 1.3: *(a) A sp^2 hybridised carbon atom (purple sphere) showing oriented sp^2 orbitals (yellow lobes) at 120° forming trigonal planar geometry (b) The overlapping of sp^2 orbitals of adjacent carbon atoms (purple and red spheres), forming σ-bonds leading to the hexagonal arrangements of carbon atoms hence resulting in planar geometry of graphene. The shaded area represents a unit cell of graphene comprised of two inequivalent carbon atoms A and B* Image adapted from[50].

each hexagon. Therefore, the unit mesh of graphene contains 6 x 1/3 = 2 atoms which can be regarded as occupying two interpenetrating sublattices, A and B, as shown by shaded area in figure 1.3(b). The honeycomb lattice is not a *Bravais Lattice* because the A and B atoms are not equivalent and one does not replace the other without breaking the lattice symmetry [50].

The lattice vectors $\mathbf{a}_1$ and $\mathbf{a}_2$ for the 2D primitive Bravais lattice shown in Figure 1.4(a) can be written as,

$$\mathbf{a}_1 = \frac{a}{2}(3i + \sqrt{3}j) \tag{1.1}$$

$$\mathbf{a}_2 = \frac{a}{2}(3i - \sqrt{3}j) \tag{1.2}$$

where i and j are unit vectors along x and y axis, and a is the spacing between adjacent carbon atoms and is represented by a nearest neighbour vector δ_n, where n=1,2,3. The corresponding reciprocal lattice vectors $\mathbf{b}_1$ and $\mathbf{b}_2$ are

$$\mathbf{b}_1 = \frac{2\pi}{3a}(i + \sqrt{3}j) \tag{1.3}$$

$$\mathbf{b}_2 = \frac{2\pi}{3a}(i - \sqrt{3}j) \tag{1.4}$$

The primitive cell of the graphene lattice is shown in figure 1.4(a) and the reciprocal lattice in figure 1.4(b) where the shaded region represents the first Brillouin Zone. Γ is the centre of Brillouin Zone (BZ) and K and K′ are two inequivalent points at the corners of first Brillouin Zone (their inequivalence arising from the two inequivalent sublattices in the conventional

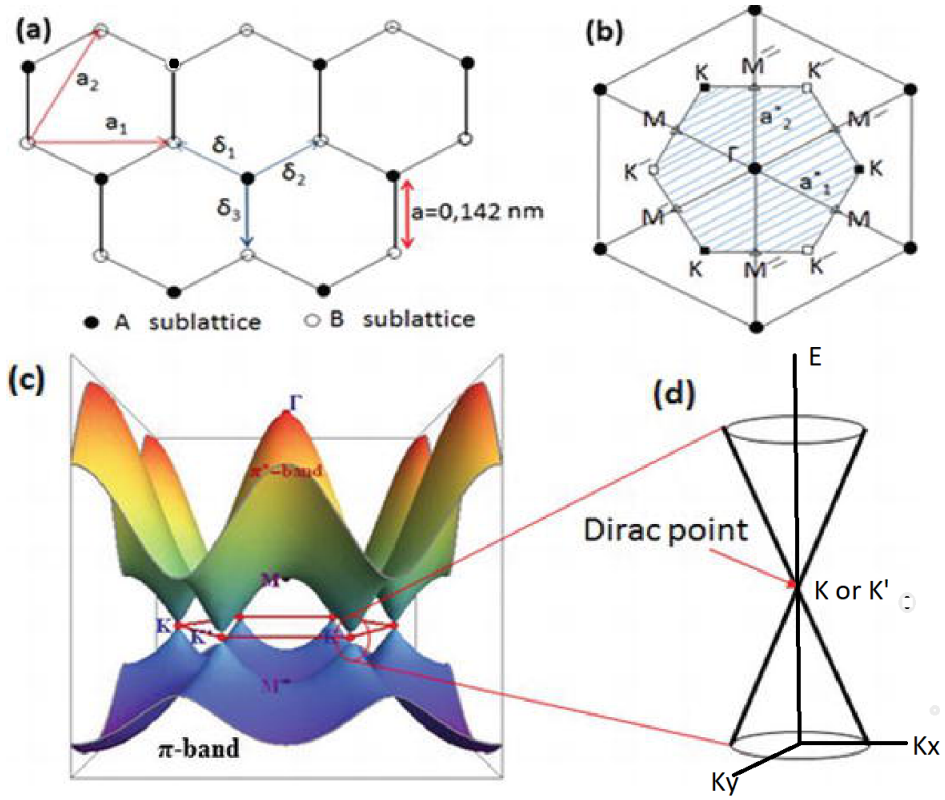

FIGURE 1.4: *(a) Hexagonal structure of graphene shown by inequvalent carbon atoms A (black) and B (white). (b) Reciprocal lattice of graphene in which the shaded region shows the first Brillouin Zone. (c) 3D electronic band structure of graphene shows high symmetry Dirac points. (d) Dirac cone showing linear dispersion relationship between energy and momentum* Image adapted from [53].

mesh). These points have a significant importance in understanding the electronic properties of graphene and are called the Dirac points [51]. Figures 1.4 (c) and (d) shows that valence and conduction bands are separated over the entire BZ except at six points (K and K') leading to a zero band gap and zero density of states at the Fermi level, in the absence of doping. This canonical type of band structure has conduction and valance bands which possess a linear electronic dispersion relation between energy $E(\mathbf{k})$and wave vector ($\mathbf{k}$) in momentum space,

$$E = \pm v_F \sqrt{(k_x^2 + k_y^2)}, \tag{1.5}$$

where k_x and k_y are the components of the momentum in the x and y directions of the 2D plane and v_F is the Fermi velocity. This dispersion relation implies that in graphene charge carriers (electrons or holes) behave like relativistic particles [51]. However, the Fermi velocity of 10^6 m/s is 300 times smaller than the speed of light in vacuum. These charge carriers are often termed as "Dirac fermions" since they are described by the Dirac equation instead of Schrödinger equation as is the case for charge carriers in conventional semiconductors [53, 54]. The electronic properties of graphene are dependent on these charge carriers, which behave like a 2D electron gas confined to move in the plane of the graphene

sheet with a mobility which reaches as high as 200,000 cm $^2V^{-1}s^{-1}$[55], making graphene an excellent conductor with conductivity six times higher than copper [1].

The unique electronic structure of graphene can also be determined through its behaviour towards incident radiation. A single layer of graphene absorbs around 2.3% of incident visible light irrespective of wavelength [53, 56] i.e., the amount of absorbance remains unchanged from 300 nm (ultraviolet) to 2500 nm (infra-red), resulting in near constant optical conductivity in that region of spectrum. Because absorbance is dependent on number of layers (n), measurement of optical absorbance is useful technique to determine the number of layers of a graphene [56]. As graphene is highly transparent, it is extremely difficult to locate graphene flakes, however choice of substrate can lead to a particular difference in opacity.

Another remarkable property of graphene is its mechanical strength, which makes graphene an exceptionally strong and robust material with estimated breaking strength of 42 N.m and Young's modulus of ≈1.0 TPa [57]. The shorter carbon-carbon σ-bonds in graphene as compared with those in diamond makes it harder than the latter [58]. Furthermore, a sheet of graphene can be stretched up to 20% thus making it the most elastic, flexible and strongest material in nature [57, 59].

Graphene can also be functionalized with other elements like fluorine to make fluorographene, hydrogen to make 'graphane' or 'graphone' and oxygen to make graphene oxide etc., in order to modify its properties for certain applications [60–62]. Moreover, graphene has very high thermal condictivity, in the range of 4.84 x $10^3 Wm^{-1}K^{-1}$ to 5.30 x $10^3 Wm^{-1}K^{-1}$ which makes it an efficient heat conductor [63]. Finally, graphene is highly impermeable and able to stop even the diffusion of helium gas, thus providing the thinnest known barrier between two regions [64].

1.2.1.2 Applications of graphene

Since graphene is among the lightest, strongest, thinnest, thermally and electrically conductive, most transparent, flexible, elastic, photoactive, stable, tunable and impermiable material, it has potentially huge industrial and laboratory applications including in ultra-fast electronics [65], energy generation and storage devices [66, 67], chemical sensors [68], hybrid materials [69] and optical devices [66]. By utilising different combinations of these properties and those of related 2D solids, "materials on demand" can in principle be acheived. For example, being transparent, conductive and flexible graphene can be used in strechable and transparent electrodes, displays, sensors, and other electronic devices [8, 70]. Graphene can be made luminiscent by introducing a band gap (by doping or applying external electrical field), and can be used for LEDs and other optoelectronic devices [39, 70]. It can be used in photo-voltaic devices such as photo-detectors, solar cells and touch screens [70]. Graphene oxide has been shown to have promise for filtering water [71]. Graphene can be tuned externally by electrical or magnetic fields for use in terahertz detection and frequency converter devices such as filters, modulators, switches, beamsplitters and polarizers [70]. Graphene based supercapacitors, batteries, transistors field emitters and resonators have already been reported [8, 33, 39, 52, 53, 59].

1.2.2 Hexagonal Boron Nitride

The atomic structure of 2D hexagonal boron nitrde (*h*-BN) resembles the crystal lattice of graphene. The boron and nitrogen atoms in 2D *h*-BN are analogous to the A and B carbon atoms in the graphene lattice and have strong covalent bonding in plane (bond length of 0.144 nm between B and N) and weak van der Waals forces between adjacent planes in the case of 3D *h*-BN, similar to that in graphite. There is a slight difference in the stacking order of 3D graphite and *h*-BN: crystalline graphite shows ABA (Bernal Stacking) while in *h*-BN boron and nitrogen atoms are arranged on top of each other following a AAA stacking order, figure 1.5. Nevertheless, despite a nearly identical atomic arrangement, the sublattices A and B in the unit cell of *h*-BN comprise atoms of different elements (i.e., B and N) leading to different on-site energy, consequently there is a wide band gap (5.9 eV) [72]. *h*-BN is hence an insulator with very different electronic and optical properties to graphene [73, 74]. The optical band gap of monolayer *h*-BN is 6.07 eV, slighly higher than the bulk because of the absence of interlayer forces [14].

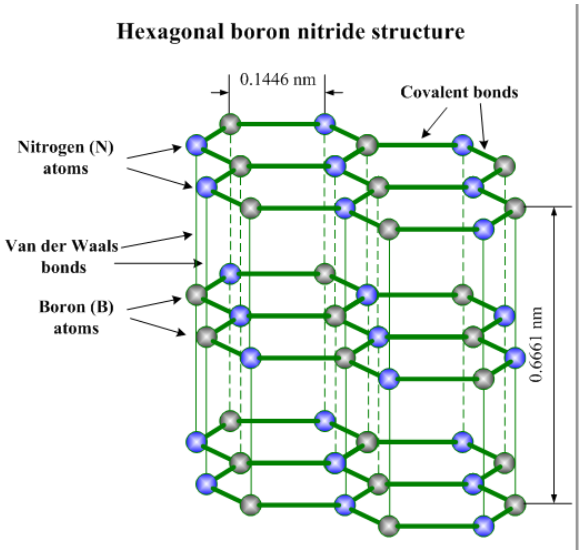

FIGURE 1.5: *The 3D structure of h-BN.* Image adapted from [31].

2D *h*-BN has a very smooth atomic surface, free of pin holes, dangling bonds and charge traps and, having a very wide band gap, low dielectric constant, high thermal conductivity, mechanical strength and temperature stability, therefore it has many promising applications [75]. Its excellent insulating property is perfect for stopping leakage of charge in electronic devices. A chemically stable and unreactive surface of *h*-BN provides an excellent platform for graphene based transistors with enhanced performance and stability [76]. Graphene transistors built on *h*-BN substrates have shown better on/off current ratio and mobility than those built on SiO_2 [75]. It also shows intense ultraviolet (UV) luminescence at room temperature, and thus can be used as a UV light emitter or UV laser [74]. Wang *et al*, in Ref [72] have discussed various prospective applications of graphene and *h*-BN heterostructures in detail.

1.2.3 Transition Metal dichalcoginides

Layered transition metal dichalcoginides belong to the class of materials with stoichiometry MX_2 (M= Mo, W, Ti, Zr, V, Nb, Ta; X=S, Se, Te) and form crystalline layered structures with in-plane covalent bonding and van der Waals attractions between adjacent layers. These materials can be metals, semi metals, semiconductors or insulators depending upon their geometry and hence possess diverse electronic and optical properties which enable their use in various applications such as lubrication [77], catalysts [78], photovoltaics [79], supercapacitors [80], rechargeable batteries [81], thermoelectric devices [82], solar cells and photodetectors [8, 83]. Although around 40 [8] different catagories of materials have been investigated in the literature, we shall discuss only briefly MoS_2, WS_2 and $MoSe_2$ in this work.

1.2.3.1 Molybdenum disulphide

Beyond graphene, molybdenum disulphide (MoS_2) is another extensively studied layered material because of its distinct optical properties. It exhibits strong absorption in the visible region of the spectrum making it a promising candidate for optoelectronic devices [84, 85]. It shows negligible photoluminescence (PL) in 3D bulk form but its monolayers and bilayers shows unexpectedly strong photoluminescence. This is due to a transition from an indirect band gap of 1.29 eV in the bulk to a direct band gap of 1.9 eV as the number of layers of MoS_2 are reduced to one, at which point photoluminescence efficiency is increased up to 10000 times [38, 85, 86]. The unit cell of MoS_2 is hexagonal in structure with a layer of Mo atoms sandwiched between two layers of sulphur (S) atoms, as shown in figure 1.6.

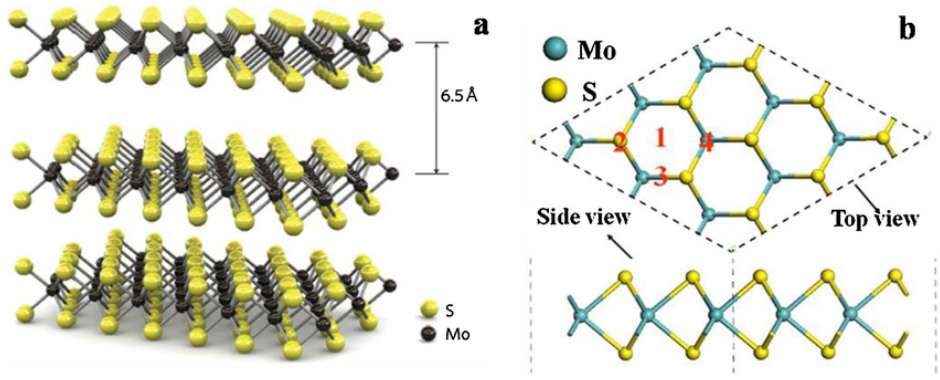

FIGURE 1.6: *(a) 3D layered structure of MoS_2, (b) Top view shows the hexagonal crystal lattice of MoS_2 (c) Side view of crystal lattice.* Image adapted from [87].

The exceptional PL and absorption properties of MoS_2 makes it an ideal material for photovoltaic and photocatalytic devices [85]. The prominent feature of atomically thin MoS_2 is that it becomes a direct band gap semiconductor whereas its bulk 3D state is an indirect gap material [88]. This behaviour is due to the variation in electronic structure of few layer MoS_2 originating from the characteristics of the d-electron orbitals which form the valance and conduction bands [85, 86]. In the bulk MoS_2 the direct energy gap is 1.8 eV between

valence and conduction bands at the K point, while the indirect energy gap of 1.29 eV is between the valance band maximum at the Γ point and the conduction minimum along the Γ - K direction at the Q-point of the BZ. In bulk MoS_2, the valence band and conduction band at the K point of the BZ are derived from localized d-orbitals at Mo atoms, which are located at the middle of two S atoms and are weakly influenced by interlayer interactions, hence remain unaffected by changes in interlayer distance. In contrast, the valence maximum at the Γ point of the BZ is derived from a linear combination of d-orbitals on Mo and p_z orbitals on S atoms, and due to greater spatial extent are more strongly dependent on interlayer distance [85].

As the thickness of MoS_2 decreases from bulk to monolayer quantum confinement, most strongly affecting the diffuse states of the (bulk) valance band maximum (VBM) and conduction band minimum (CBM) at Γ and Q, respectively, becomes more pronounced. This leads to a widening of the indirect band gap. The strongly localised conduction and valence band states at K are substantially less affected (with an increase in the direct gap of only 0.1 eV from bulk to monolayer). Hence, the indirect band gap eventually, in the monolayer limit, becomes larger than the direct band gap, figure 1.7 [85–87] and the material becomes direct gap [88–90]. In monolayers, the direct band gap gives rise to intense interband transitions by relaxation of excitons and emission of photons having energy lying in visible spectrum, hence defining the strong luminescence efficiency which is 10^4 times higher in monolayer MoS_2 than in the bulk material [38, 85].

This unique optical and electrical behaviour has been exploited in the construction of phototransistors. It is found that photocurrent generated by incident light is so rapid that it changes the ON/OFF state within 50 ms with a switching ratio of ~1 x 10^8. The photoresponsivity from a monolayer can be very high, up to 7.5 mA/W even when illuminated by a very low optical power of 80 μW, compared with 1 mA/W in a graphene based field effect transistor (FET) [92]. Recently, a photoresponsivity up to 880 A/W for monolayer MoS_2 phototransistors is reported in Ref [34] which is a 10^6 times improvement from the previously reported values, thus making MoS_2 better than graphene for uses in sensors, magnetic materials, phototransistors and photodetectors [34, 92–94].

1.2.3.2 Molybdenum diselenide and tungsten disulphide

$MoSe_2$ and WS_2 are other layered TMDCs having properties such as thermal stability and PL which can be tuned by varying thickness and temperature [95]. These materials are also indirect band gap semiconductors and belong to the family of TMDCs with crystal structures similar to MoS_2. Similar quantum confinement behaviour to that of MoS_2 can be seen in both of them, upon decreasing the number of layers to fewer than four. That is, the indirect band gap increases and becomes higher than the direct band gap (along K to K) in monolayers of these materials [95]. The crossover results in a change in energy gap for $MoSe_2$ and WS_2 from 1.1 eV and 1.3 eV in the bulk to 1.44 eV and 2.1 eV in monolayers respectively, figure 1.7. The direct band gap of these single layers matches well with the visible solar spectrum hence providing excellent materials for solar cells [91].

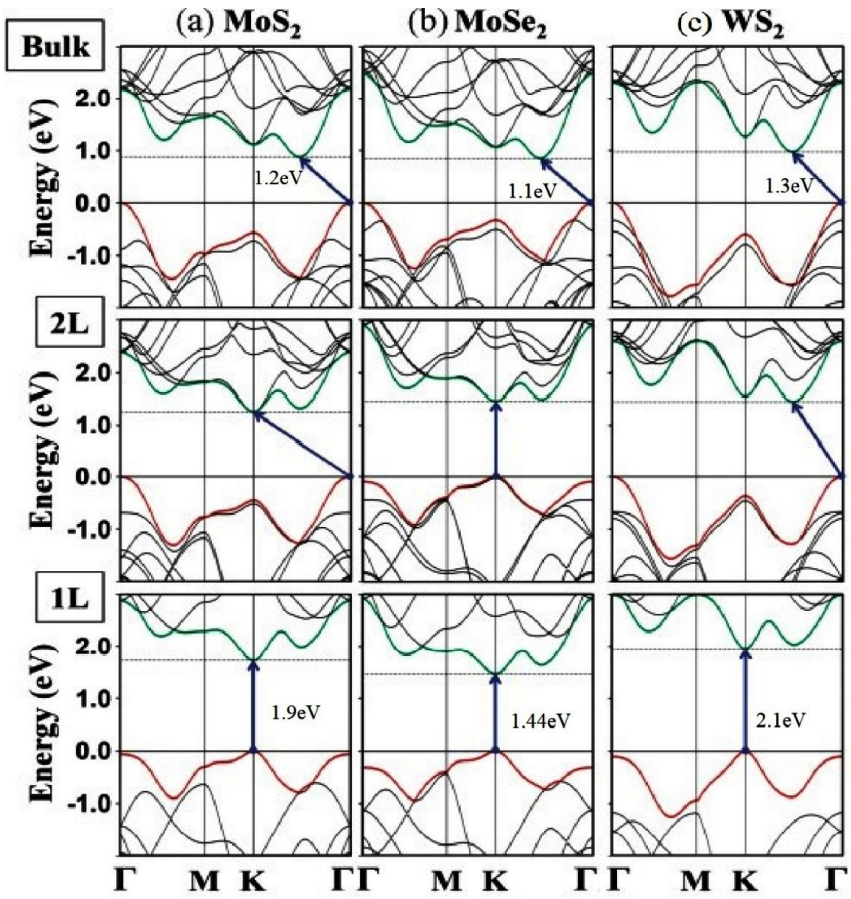

FIGURE 1.7: *Band structure of MoS_2, $MoSe_2$ and WS_2 from the bulk to bilayer (2L) and monolayer (1L). The horizontal lines represent the valence band maximum and the dotted line indicates the conduction band minimum. The solid arrows show the lowest energy transitions.* After Ref [91].

The striking difference between the bilayer band structure of MoS_2 and $MoSe_2$ can be seen when varing temperature from -195 to 178°C. The increase in temperature slightly expands the distance between the bilayers of $MoSe_2$ and this thermal decoupling gives rise to an easy bandgap crossover from indirect to direct gaps leading to degenerate direct and indirect bandgaps in $MoSe_2$, hence enhanced PL in bilayer $MoSe_2$ as compared to bilayer MoS_2. In contrast, this thermally driven bandgap degeneracy cannot be acheived (unless the layers are seperated physically) in bilayer MoS_2 where indirect and direct bandgaps are well apart. This unique difference makes $MoSe_2$ more efficient material for nanoscale photovolatic devices and photo catalysts than MoS_2 [38].

The properties of 2D TMDCs can also be modified by applying strain which alters the lattice symmetry and results in changes in effective masses, band gap energy and positions of conduction band minima and valance band maxima. The effect of compressive and tensile stresses on single layer MoS_2 results in changes in the value of lattice constant, a, which changes the position of VBM and CBM, hence it changes the behaviour of the monolayer from semiconductor to metallic [91].

1.2.4 Other Two-dimensional Solids

Apart from graphene and TMDCs there exists an extensive library of layered materials such as transition metal oxides (TMOs), chalcoginides, monochalcoginides, phosphorene, stanene, silicene and germanene. Analogous to graphene, the last four have gained particular attention of researchers because of their potential applications in batteries [26]. Their 2D sheets form buckled honeycomb structures instead of a planar hexagonal layer like graphene. Unlike graphene, silicene, germanene and stanene have no parent bulk crystalline structure and cannot be isolated like graphene but have to be grown on suitable substrates, while phosphorene can be seperated from its thermodynamically stable parent form of layered phosphorous, called black phosphorus. Balendhran *et al*, in Ref [24] have undertaken thorough investigations of their electronic, thermal and mechanical properties and possible applications.

The topological insulating effect, an unconventional quantum phase of matter, can be seen in Group V-VI chalcoginides such as Bi_2Te_3, Sb_2Te_3 and Bi_2Se_3, which are referred to as topological insulators. These unique materials have metallic surface states residing in the bulk insulating bandgap with conductive massless Dirac Fermions on their surface and have found applications in 2D quantum wells [18], low energy dissipation electronic devices and spintronics [15, 96]. Similarly, giant piezoelectric effects have been reported in monolayer Group IV monochalcogenides including SnSe, SnS, GeSe and GeS [97]. This unique property of these monochalcogenides along with their superior photosensitivity [22], high crystallinity and ability to withstand high strain [57, 98], has made them promising materials for applications in nano-sized integrated electromechanical and optical sensors, piezotronics and energy harvesting in portable electronic devices [22, 97].

1.3 Fabrication

Fabrication of 2D materials, particularly on an industrial scale, is extremelly challenging. Current approaches can be grouped into two types: Top-down approaches in which a 2D layer is directly isolated from its parent bulk material, which requires exfoliation, segregation and then deposition of flakes on an appropriate substrate and bottom-up approaches in which a 2D layer is directly grown on a suitable platform. Each method has its own benefits, and is selected on the basis of required properties and quality of the final 2D material. Figure 1.8 illustrates some of the fabrication approaches currently being used at industrial and laboratory scale.

1.3.1 Dry Exfoliation

Removal of layers from the bulk material directly by mechanical, electrical or Laser assistance is classed as dry exfoliation [99]. Procedures falling into this category are described below:

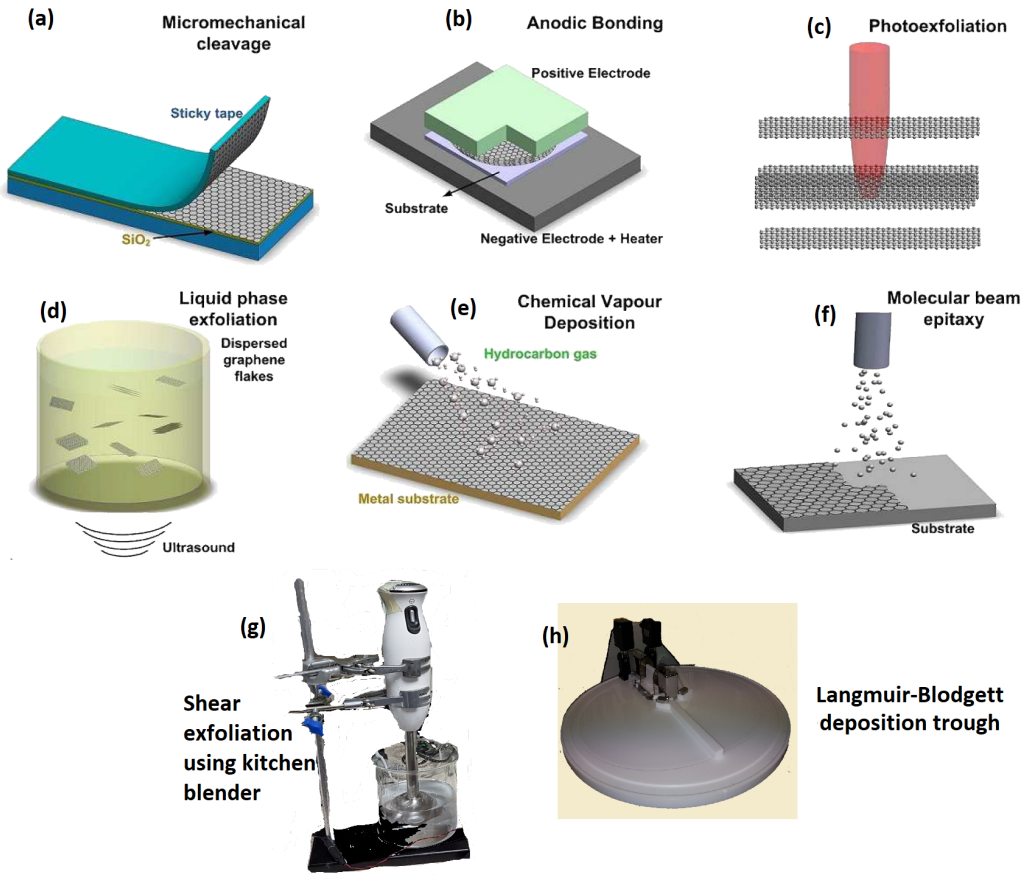

FIGURE 1.8: *Schematic illustration of some fabrication methods.* Image adapted Ref [99].

1.3.1.1 Micro-mechanical Exfoliation

The first method used for isolation of two-dimensional solids, pioneered in 2004 by Geim and Novoselov is micromechanical exfoliation, commonly termed the 'Scotch Tape' method [1]. In this relatively easy and cheap method, a flake of the bulk "parent" material is placed between two adhesive tape strips and the strips are gently pulled apart to seperate the layers. The process is repeated many times until few or monolayer platelets are formed which are then transfered by attaching tape to the substrate. After dissolving the tape by solvent such as acetone, the undissolved layer of graphene is left on the substrate for characterisation and application. Depending upon the initial size of the crystal, various sizes of flakes in a range from nanometers to a few micrometers are obtained in this way, which are inherently defect free. However, this laborious method is very time consuming and not suitable for production at industrial level because of the very low yield [99].

1.3.1.2 Anodic Bonding

Anodic bonding is mainly used at an industrial scale for protecting glass from humidity or contamination [100, 101] and is also known as the field assisted glass-silicon sealing. In the conventional form of this process, a layer of silicon is coated on the glass surface at high temperature ($\sim$ 200°C for 10-20 mins) and an external electric field (0.5 kV to 2 kV) applied. The positive terminal of the D.C. power supply is connected to the silicon wafer and negative terminal to the glass substrate. Under the influence of the high temperature and electric field Na_2O impurities in the glass decompose into Na^+ and O^{2-} ions. Na^+ ions are then attracted towards the negative terminal because of their increased mobility leaving behind O^{2-} ions on the surface of glass, creating an electric field at the glass surface. The silicon layer is then pulled toward the glass by this electric field and attached to its surface. This technique has recently been adopted by Ref [102] for graphene deposition on glass by replacing silicon with graphite. Single layer graphene with flake size up to 1 mm has been successfully attached to the glass surface using this method. The number of layers deposited on the substrate can be controlled by selecting optimum values for temperature and voltage.

Although high quality graphene flakes can be produced the method cannot be adopted for industrial scale production. Firstly, this method can only be employed for depositing graphene on borosilicate glass. Secondly, it is very difficult to spot graphene on glass due to its transparent nature. Furthermore, doping could be induced in the graphene sheets during treatment. Finally, the yield is dependent on the intial area covered by graphite. However this method may be suitable for studying the optical properties of graphene [102, 103], and can be adapted for deposition of other 2D layered materials [104].

1.3.1.3 Photoexfoliation

The detachment of layers from the surface of layered material by irradiation is termed photoexfoliation. In this less established exfoliation process a laser is usually employed. The specific energy of laser pulses are used to seperate layers from the bulk material in vacuum or under an inert atmosphere. The number of exfoliated layers can be controlled by the energy of the laser hence samples from monolayer to a few layers can be obtained [99].

1.3.2 Surface Growth

2D materials can be grown on surfaces of metals/insulators using solid, liquid or gaseous precursors, by adopting different techniques such as Chemical Vapour Deposition (CVD), Pulsed Laser Deposition (PLD), Molecular Beam Epitaxy (MBE), Plasma Enhanced Chemical Vapour Deposition (PECVD), Epitaxial Growth (EG) and Chemical synthesis [99]. These approaches are discussed breifly.

1.3.2.1 Chemical Vapour Deposition

Chemical Vapour Deposition is a well developed process widely used at industrial scale for the deposition of thin films (mainly multilayers), in which a substrate (often catalytic) is

exposed to gaseous precursors. In recent years, this process has been extensively explored by scientists for deposition of single or few-layer graphene and other 2D materials. The selection of precursors and substrate is highly dependent on the required quality of the 2D material, cost and application of the grown material. In this method, the precursors decompose on the surface of a selected substrate at high temperature in order to grow a thin film, whereas any by-products evaporate. The as-grown layers may then be transferred to other substrates or onto different layers for production of heterostructures, or used directly in device construction. A detailed discussion of CVD is beyond the scope of this thesis and the reader is referred to the review of Bonaccorso *et al* [99].

Copper(Cu) is commonly used as the substrate for growth of graphene because of its cost and the ease with which its surface composition can be modified by electropolishing, acid and/or plasma etching. Furthermore, uniform thickness control of graphene is possible because of the low solubility of carbon in Cu compared with other transition metals such as Ni and Co. Methane is usually used as the precursor for growth of graphene on Cu, which is undertaken at elevated temperature ($\sim$ 1000°C) in a furnance under either atmospheric or low pressure conditions. The growth process is close to being self limited depending on conditions, as further growth is suppressed once the Cu surface is fully covered with graphene [105]. CVD is highly sensitive, as slight fluctuations in temperature or variations in pressure or quantity of gas can change the grain size or thickness of the layer. In principle, large area graphene samples can be grown, but apart from monolayers, nearly 5% of bilayers and trilayers are also found. Furthermore, the difference in thermal expansion of Cu and C gives rise to "wrinkle" or "pleat" defects mainly upon cooling [106] resulting in film quality below that of exfoliated graphene. Moreover the graphene produced by this method is polycrystaline and dependent on the grain size of the substrate underneath, which strongly effects the electronic properties, especially mobility of electrons in graphene [107].

Growth of other 2D materials by CVD is also possible Ref [14, 53] but the selection of substrate, precursors and growth conditions is more challenging and specific to the material chosen. Hence, this approach is less developed for materials beyond graphene.

1.3.2.2 Epitaxial Growth

Epitaxial growth includes precipitation, liquid phase epitaxy, vapour phase epitaxy, and Molecular Beam Epitaxy (MBE) [99]. The most straightforward form of epitaxial growth is via decomposition of the surface of a material, which has been demonstrated for the sublimation of Si from SiC [108]. In this approach a single crystal of SiC is annealed at high temperature in vacuum ($\sim$ 1500 – 2000°C) typically after a suitable surface pre-treatment. The process is highly dependent on temperature, heating rate and pressure. The growth of graphene islands start at multiple locations on the SiC crystal which join together, hence a non homogeneous layer appears with grain boundary defects. Although this method produces an epitaxial layer on a semi-insulating substrate suitable for device fabrication, it requires significant energy input and the use of expensive substrates. Hence, it is likely only to be of use in a limited range of high-value applications. Moreover, such an approach is not readily generalised to the production of other 2D materials.

Similarly, MBE is a method of growing high-quality epitaxial films of semiconductors, metals, or insulators with sub monolayer control under Ultra High Vacuum (UHV) conditions. In this method, ultrapure precursors are heated to create a beam of atoms or molecules in a gaseous state, which then impinge on a substrate, typically held at elevated temperature, to grow the required film. The low pressures (typically $< 10^{-11}$ mbar) and automated control of shutters governing exposure of the substrate to the atomic/molecular beam allow the reproducible and controlled fabrication of monolayers, thin films and heterostructures [8, 109]. Successful homogeneous growth of graphene on *h*-BN is reported by Ref [110] and remarkably high mobility was observed. Growth of other 2D materials such as silicene, $MoTe_2$ and Bi_2Se_3 using MBE is also reported in Ref [111–113] which shows the generalisability of this method. However, the requirement for epitaxy, cleanliness and the specialised appratus required also limits this approach to niche high-value applications.

1.3.3 Liquid Phase Exfoliation

Liquid phase exfoliation is generally performed in two ways; sonication and shear exfoliation which are discussed below.

1.3.3.1 Sonication

Monolayer and few-layer materials may be exfoliated from bulk precursors in liquid environments by ultrasonic waves. A bulk layered material (e.g, graphite flakes) is dispersed in a stabilizing liquid, followed by sonication. The resulting suspensions are washed and exfoliated flakes are segregated, usually by centrifugation. The stabilizing liquid is necessary to keep the graphene flakes from re-aggregation and to ensure that they spread throughout the liquid to make an homogenous suspension [114–116]. Such liquids may be solvents (e.g., Benzyl Benzoate, etc.) [117], binary solvents (such as dimethylformamide (DMF) and n-butylalcohol(NBA) in a ratio 1:3) [115], aqueous surfactant solutions (e.g., sodium dodecylbenzene sulfonate and deionized water, etc.) [114] or a polymer (such as polyvinylpyrrolidone, etc.) [116]. Although sonication gives better yield as compared with the methods discussed earlier, it is an highly time consuming, slow and lengthy process with sonication times up to 460 hours reported [118]. Thus the process is energy inefficient. Furthermore, more rigorous sonication increases the edge-defects in the resulting flakes [117, 118] and reduces the flake size [118]. However, it is relatively simple and low cost, with high yield compared with methods such as CVD, MBE and Anodic Bonding.

1.3.3.2 Shear Exfoliation

Shear exfoliation is another approach for exfoliating layered materials in a liquid medium. A high shear mixer or blender is used for exfoliation, instead of a sonicator. This approach has been the most successful method reported for the production of large quantiites of dispersed graphene and other 2D materials in suspensions at industrial level so far [119–121], providing defect-free suspensions in large quantities (100s of litres [119]) for thin film and

heterostructure production [122]. Moreover, the approach is rapid and has low energy input making it attractive from the viewpoint of efficiency. Any instument which can produce a high shear rate, $>10^4 s^{-1}$, is perfect for accomplishing the job, thus even a simple kitchen blender which can produce shear rates greater than the required minimum is capable of producing large quantities of exfoliated materials, as shown by Paton *et al* in Ref [119].

Shear mixing is also achieved in the presence of stabilizing liquid similar to that required for sonication, which can be a solvent, surfactant or polymer. A solvent is chosen in a way that its surface energy should approximately match that of the layered material in order to disperse it homogenously and stop it from aggregating. Hernandez *et al* [117] has explored the best solvent for this purpose and found benzyl benzoate, NMP (1-Methyl-2-pyrrolidinone), GBL (γ-Butyrolactone) are the best solvents to obtain a high yield of graphene. The concentration of suspensions of graphene obtained by shear exfoliation is only limited by the initial volume of graphite C_i, mixing volume V , mixing time t, rotational speed N and the diameter of rotor/stator D. Paton *et al* [119] have empirically determined expressions for the concentration of graphene suspensions:

$$C \propto C_i t^{\tau} N^n D^d V^v \tag{1.6}$$

and for commercial production of graphene the rate of production $P_R = VC/t$ is given by,

$$P_R \propto C_i t^{\tau-1} N^n D^d V^{v+1} \tag{1.7}$$

where τ, n, d, and v are exponents of mixing time (t), mixing speed (N), rotor diameter (D) and mixing volume (V), respectively. The value of these exponents can be determined by varying the associated parameter while keeping the other parameters described in equations 1.6 and 1.7 constant. The determination of these exponential values is crucial for the estimation of concentration of dispersed material and the rate of production.

Similarly, an aqueous surfactant solution can be used as a stabilizing liquid for exfoliation. Surfactants are amiphilic molecules having a hydrophilic (water attracting) and a hydrophobic (water repelling) end, while graphite is hydrophobic in plane and hydrophilic at the edges. Exfoliation of graphite in the presence of a surfactant results in adsorption of the hydrophobic end of the surfactant on the graphite plane while the hydrophilic end remains in the water creating a repulsion which prevent graphene flakes from re-aggregating. A comparative study on the effect of different surfactants is performed in Ref [123], which shows that nonionic surfactants yield better concentrations than the ionic surfactants.

Before using graphene flakes in applications or deposition of films, solvents or surfactants along with unexfoliated material must be removed. Unexfoliated heavier flakes usually settle out of suspension after some time and can be separated from the thinner flakes by ultracentrifugation. Solvents can be removed by vacuum filtration and may evaporate on deposition [117] , while surfactants having high boiling points are less likely to be removed without employing further cleaning methods. For this purpose suspensions are centrifuged again at higher speeds which seperates even thinner flakes from aqueous suspensions. The aqueous surfactant solution is removed and the flakes are resuspended in ultra high purity

(UHP) water by sonication and centrifuged again for more cleaning, this process is repeated until all surfactant is removed. A great advantage of liquid phase exfoliation is that it is easily generalisable to a range of different 2D materials, the only requirement being that there is a suitable parent material from which layers can be exfoliated and that the layers are stable in the chosen liquid. The remaining flakes are resuspended in a solvent and can be deposited on the suitable substrate by different techniques such as vacuum filtration, Langmuir-Blodgett assembly [124], the Langmuir Schaefer method [125], drop-casting, or our newly adapted inverse dipping liquid interface technique. Film deposition techniques, employing a suitable suspension of 2D material as a precursor are described in detail in the following sections of this chapter.

1.3.4 Langmiur-Blodgett/Schaefer Deposition

A wide range of applications of graphene require large area continuous, transparent and conductive films. The Langmuir-Blodgett (LB) and Langmuir-Schaefer (LS) deposition methods are mature techniques for deposition of mono or few-layer thin films on solid substrates at the liquid-air interface. The liquid is often the ultra high purity water and is known as the subphase. A comprehensive discussion of these techniques is provided in the book by Petty [126].

In these techniques, the material which is to be deposited is spread with the help of a micro syringe as a solution in a volatile solvent (which is less dense than water), on the surface of a body of water, followed by compression of material (after evaporation of the solvent) using barriers to acheive a solid continuous film at the air-water interface (figure 1.8). The solvent should be insoluble in water, having low boiling point, and evaporates from the water surface leaving behind floating hydrophobic flakes at the surface, which are deposited upon lowering a hydrophobic substrate into the water. The phase of the film is continuously monitored during compression by using Whilhelmy plates dipped into the water surface hanging on an electronic balance (which measures the surface pressure). An isotherm is plotted between surface area and surface pressure during the compression. The isotherm indicates the gradual change in the phase of film on the surface of the water from gaseous state to liquid state, which turns into a solid film upon evaporation of solvent and further compression. The process of achieving the solid film can be aided by adding more material and slowly opening and closing the barriers. When the isotherm indicates the presence of a solid layer at the air-water interface, a substrate is moved vertically through this interface to transfer the film in case of LB assembly, while a horizontal substrate is moved through the interface when employing the LS approach. Both approaches have been successfully employed to produce graphene films [124, 125].

Before deposition, a clean hydrophilic or hydrophobic substrate is prepared [127]. A hydrophilic substrate is used to attach the hydrophilic side of the film and thus in LB deposition it is lifted upwards through the subphase once the film has reached the solid state after compression. In the case of exfoliated graphene in the presence of surfactant, the surfactant molecules are also deposited along with the graphene flakes. The adsorption of surfactant

molecules on flake's surface as discussed previously, is in such a position that their hydrophilic ends are under water which assists deposition on the hydrophilic substrate when moving through water into air. Conversely, a hydrophobic substrate can be moved from air into water, which is suitable for materials suspended in solvents.

1.3.5 Liquid Interface Deposition

Surfactant suspensions are good for stabilizing graphene and other 2D materials, but if the surfactant is deposited along with the flakes of these materials in production of thin films their presence will alter the properties of that film and may not be desirable. Therefore, thorough washing is required before deposition which introduces problems including material loss and re-aggregation. Moreover, most approaches to surfactant removal are time consuming and inefficient. To overcome the disadvantages associated with other deposition methods a novel approach to the controllable formation and deposition of monolayer and few-layer films of two-dimensional solids and heterostructures derived from them, termed 'Liquid Interface Deposition' (LID) was developed within the author's research group (in conjunction with A.G. Mathieson, M. Szablewski and M.R.C. Hunt). Evaluation and optimisation of this technique forms the basis of the experimental work reported in this thesis.

The LID technique enables deposition of films and heterostructures of two-dimensional materials on almost any solid substrate without prior surface treatment, starting with a solution or liquid suspension (with or without surfactant) of thin platelets of the two-dimensional solid(s). The technique is applicable to any two-dimensional solid(s) which can dispersed in either suspension or solution form with or without surfactant, and therefore includes the vast majority of those materials which do not require a substrate for stablity (e.g., graphene, TMDCs, *h*-BN etc.). The LID method performs three roles: (1) the assembly of a thickness-controlled film from platelets of a two-dimensional solid at the interface of two immiscible liquids, which can then be readily transferred onto a substrate through dipping, casting (pouring) or a freezing-based approach, as described below; (2) the removal of platelets of undesirable (e.g., multilayer) thickness from the film, if present in the initial suspension; (3) the removal of any surfactants and selected non-covalently bound contaminants from the platelets, forming a 'clean', uncontaminated film or heterostructure of the two-dimensional solid(s). The method has the advantages over other approaches to thin film and heterostructure production described in this Chapter in that it is readily scaled to mass production, has a low energy budget, requires little specialised equipment or knowledge, and can be adapted to ensure minimum waste and environmental impact. The key to this process is the formation of an interface between two immiscible liquids: the suspension containing thin platelets of the two-dimensional solid and a second 'separation solvent'. The latter is chosen such that (1) it is immiscible with the liquid component of the solution or suspension (water in the case of aqueous supsensions/solutions); (2) it has a density both greater than that of liquid component of the solution or suspension and such that the buoyancy of platelets larger than a chosen thickness would be insufficient to prevent their separation

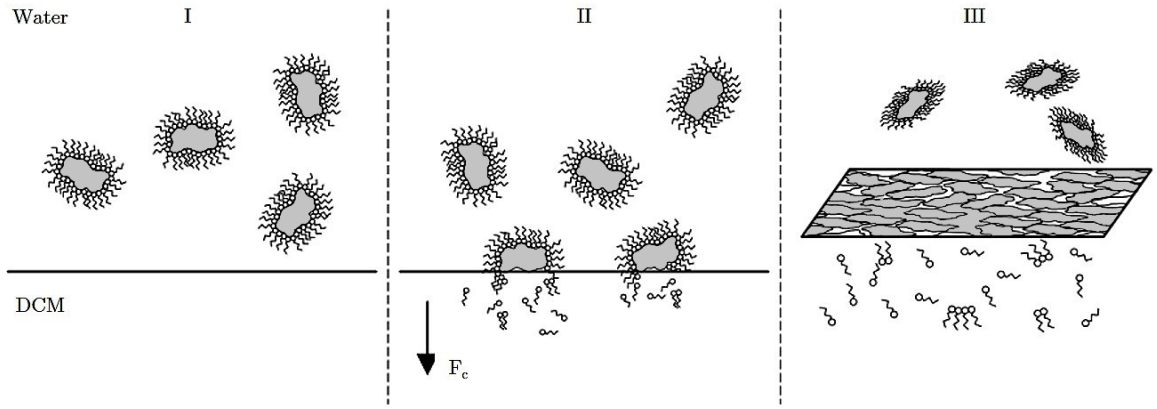

FIGURE 1.9: *Left side of figure, (I), illustrates a suspension of 2D material before centrifugation where flakes are in the water/surfactant solution. The middle, (II), shows the second stage, demonstrating the effect of centrifugation. The centrifugal force (F_c) draws the platelets to the solvent/water interface. Upon contact with the solvent, the Triton X-100 is stripped from the platelets and dissolves into the solvent, leaving clean platelets at the interface. The right side of figure, (III), illustrates the final stage where surfactant free platelets accumulate at the interface forming a continuous film.* [122].

to the solvent; (3) it possesses a separation coefficient (K_p) for any surfactant or other non-covalently bound contaminant which is large (≳5×) compared with that of the liquid component of the solution/suspension. For aqueous solutions of platelets of two-dimensional solids dichloromethane (DCM) was selected as meeting this condition. Upon centrifugation, platelets of the 2D material migrate towards the interface and those which are sufficiently buoyant (i.e., below a certain thickness) assemble at the interface to form a continuous thin film, the extent of which is determined by the concentration of the suspension. Figure 1.9 illustrates the whole process of cleaning and assembling of flakes at boundries of both liquids, where the flakes are forming continuous film at liquid interface. Platelets or re-aggregated material of sufficient thickness to be insufficiently buoyant to prevent separation into the dense 'separation solvent' are removed from the interface to settle at the bottom of the centrifuge tube. Any surfactant or contaminant present within the platelets at the film interface is removed due to their greater affinity for the separation solvent. As a result a clean monolayer or few layer film of the two dimensional solid assembles at the liquid-liquid interface, the thickness of which can be controlled by concentration of the suspension and by selection of separation solvent. Once formed at the interface between the two immiscible liquids the film can be transferred to a variety of substrates, both hydrophobic and hyrophilic (including glass, oxidised silicon wafers, copper foil, aluminium foil and plastic), by a variety of techniques including dipping, pouring/casting, or freeze-transfer. LID can be used to prepare vdWHs easily, as second or subsequent layers of other materials can be deposited by following the same procedure.

1.3.6 Critical Evaluation of Exfoliation Methods

A general idea of the different methods for producing thin films, monolayers and heterostructures of two-dimensional solids and their performances is given in Table 1.1.

Technique	Production Rate	Quality	Flake size/Area	Thickness Control
Scotch Tape	Very Slow	Very High	Small	No
Anodic Bonding	Very Slow	High	Small	Yes
CVD	Slow	Medium	Large	Self limited
MBE	Slow	High	Medium	Yes
LS/LB	Slow	Low	Large	Yes
LID	Fast	Medium	Large	Yes

TABLE 1.1: Comparison of different film deposition techniques

Briefly, we can deduce that the dry exfoliation methods have the advantage of providing graphene of very high quality and purity, and, due to the low complexity, they are perfect for laboratory research. However, the size of the flakes, controllability and production rate are too poor to use this method for industrial production. On the other hand, the growth of 2D materials on surfaces by CVD or MBE allows a large size sample growth with a high controllability, but their expense makes these methods applicable only for high-value applications at smaller scale. Higher quality films can be developed by using MBE than those by CVD. LB/LS deposition techniques can be used to deposit large area films at industrial scale, however, as the surfactant cannot be completely removed from the flakes used to develop the films they may not reflect the intrinsic properties of the materials used. In constrast, LID is a fast and scalable process which can remove surfactant completely from the exfoliated flakes. Flake size in LS/LB and LID are dependent on those of the precursor. As reported later, shear exfoliation of graphene results in reduction of flake size with increasing exfoliation time, which indicates that a careful study of precursor formation is required in the optimisation of films produced by liquid deposition techniques.

1.4 Van der Waals Heterostructures

"Conventional" semiconductor heterostructures usually require stringent matching of the crystal lattices of the materials at the heterojunction, strongly limiting the range of such interfaces which may be fabricated. However, the properties of many two-dimensional solids open the possibility of circumventing this restriction. The strong covalent bonds within the plane of the 2D material provides strength to the layer in two dimensions while weak and non-directional interactions between the layers hold adjacent layers together irrespective of size or lattice mismatch forming a van der Waals heterostructures (vdWH) such as proposed by Geim and Grigorieva in 2013 [31].

As discussed earlier, the portfolio of 2D materials is broad and there are rich and varied properties possessed by these fascinating materials. For example, graphene on one hand is

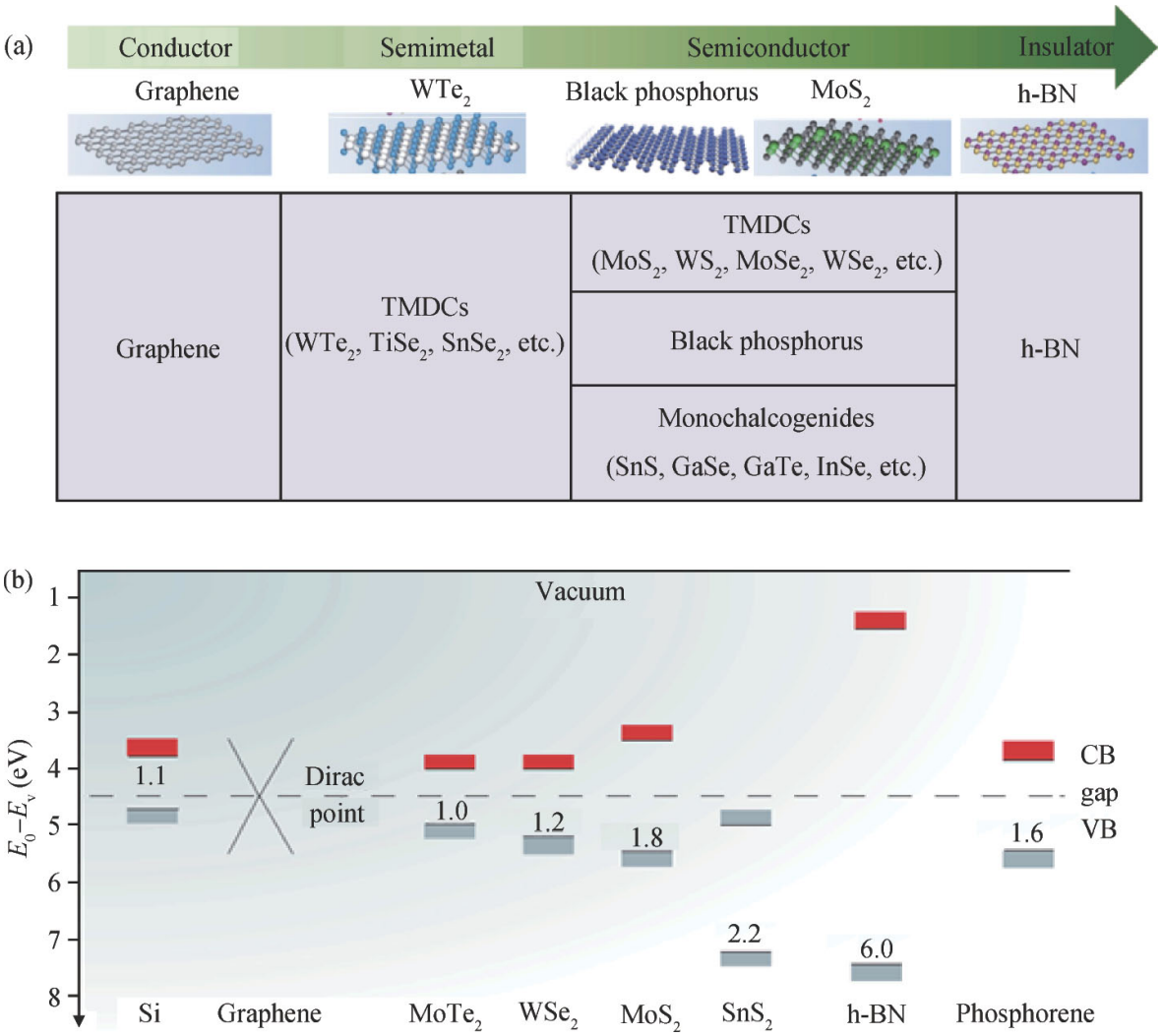

FIGURE 1.10: *(a) A library of two dimensional materials with their properties. (b)Enegry gap of 2D materials as compared with Si* [128].

a material that is mechanically very strong, relatively transparent, and an exceptional conductor while on the other hand, *h*-BN is an insulator, and MoS_2, $MoSe_2$ and WS_2 are indirect band gap semiconductors, figure 1.10. The extensive library of these 2DLMs with their wide range of properties provides the platform to explore applications by combining them in a single unit in the form of a vdWH thus resulting in "materials on demand" with full control over their properties. The fabrication of such structures at atomic level is challenging, with MBE and micromechanical exfoliation techniques having been employed so far to create these vdWHs [31].

1.4.1 Fabrication

Until now, there has not been a single method capable of fabricating vdWHs of 2DLMs with large area [128], although devices have been constructed at laboratory scale. The two primary approaches that have been previously employed for fabricating van der Waals heterostructures are mechanical transfer of exfoliated two-dimensional flakes, coupled with

precise alignment and directly growing the two-dimensional materials in the required order on a substrate. These techniques are discussed in recent reviews of vdWHs [128, 129].

1.4.2 Applications

There is huge potential for applications of vdWHs, which provide a route to engineering a device at atomic level which is both ultrathin and has unique properties. New devices based on large-scale heterostructures are still in the future. However, the wide opportunities for developing new devices have been explored in laboratories. For example, vdWHs of graphene and *h*-BN have been created by using six alternating layers of bilayer graphene and *h*-BN to create nanoscale capacitive devices [130]. Such a combination of insulator and conductors can be used to produce tunnelling transistors [131]. *h*-BN is particularly, appealing due to its large band gap (6.0 eV [128]), its high breakdown field and low number of impurity states [132]. These heterostructures can be used in production of logic gates [32], memory devices [133], radio frequency oscillators [134] and resonant tunnelling electric diodes [135]. Graphene–WSe_2–graphene heterostructures can be used in photodetection devices [136].

TMDCs and black phosphorus based heterostructures with various combinations have been used to build photo detectors, in order to achieve better performance in responsivity and detectivity. High photo detecting performance can be acheived by making heterojunctions, such as MoS_2/WSe_2, black phosphorus/MoS_2, MoS_2/WS_2, and GaTe/ MoS_2 [137]. Increased light absorption is seen in MoS_2-graphene-WSe_2 heterostructures [138].

Chapter 2

Characterisation Techniques

In order to thoroughly investigate and understand the properties, structure and quality of nanomaterials a wide range of characterisation techniques can be employed. These include Raman spectroscopy, optical absorption and emission spectroscopy, transmission electron microscopy, Auger electron microscopy, scanning electron microscopy, low energy electron diffraction, electron back-scatter diffraction, X-ray photoelectron spectroscopy, atomic force microscopy and X-ray reflectivity etc. However, none of these techniques on its own is sufficient to provide the information to fully characterise a nanomaterial and a multi-technique approach is almost always required. In this chapter an introduction to the experimental techniques used to characterise the samples produced in this thesis is provided. An overview of the basic principles and the theoretical background of each technique is presented and the use of each technique for the study of graphene and other two-dimensional layered materials is described.

2.1 Raman Spectroscopy

When photons interact with a material, they may be reflected, transmitted, absorbed or scattered. The light scattering process can provide valuable information about a sample. If the scattering does not involve any transfer of energy between the incident photon and the molecule, it is known as elastic, or Rayleigh, scattering. Conversely, if any change in the energy of photon occurs during the scattering process, this phenomenon is termed as inelastic scattering, or the Raman effect, and provides the basis of Raman spectroscopy. In Raman spectroscopy, the sample under investigation is irradiated by a single frequency source of light (usually a laser). Any difference in the energy of scattered beam from the incident beam can be detected by a spectrometer.

The idea of inelastic scattering of light was first proposed by Smekal [139] in 1923, and the first experimental observation was reported by the Indian scientists Raman and Krishnan in 1928 [140]. As a result of Raman's observations, he was awarded the Nobel Prize

in Physics in 1930, and the phenomenon is referred to as Raman scattering [141]. After the development of laser sources for use with Raman Spectroscopy in 1962 [142], it has become a widespread and versatile analytical tool for non-destructive characterisation of materials, which can provide information on the chemical structure, composition, vibrational and electronic states of a solid, liquid or gaseous sample.

2.1.1 The Raman Shift

As mentioned in section 2.1, there are two types of scattering as a result of interaction of photons and a material. In Raman scattering, the interaction of light with a molecule, or solid results in the distortion (polarization) of the cloud of electrons around the atomic nuclei to form a short-lived state called a 'virtual state', as shown (ν_0) in figure 2.1. This is an unstable state, the lifetime of which is short enough to avoid violating Heisenberg's Uncertainity Principle. There is a probability that the molecule or solid is left in an excited state after the scattering process, resulting in a change in photon energy (as shown by (ν_{nm}) in figure 2.1 where, m and n are different vibrational states of the ground electronic state). This change in energy can result from absorption or emission of one or more quanta of energy associated with a fundamental excitation of the molecule or solid, known as anti-Stokes or Stokes scattering respectively. Such fundamental excitations can be phonons/molecular vibrations, rotations, plasmons satisfying the Raman selection rule that the excitation is associated with a time-dependent variation in polarizability. Note that Raman spectroscopy can be regarded as complemetary to infra-red spectroscopy, in which a time-dependent dipole moment couples excitations with a photon field leading to absorption.

In Raman scattering, the incident light frequency, ν_0, is selected in such a way (i.e., $\nu_0 \ll \nu'$) that it remains much smaller than the energy difference between two real electronic states ΔE. This is referred as a non-resonant Raman scattering, which is a weak process, as about one in 10^6 - 10^8 photons is Raman scattered. The difference in frequency from the incident radiation arising as a result of Stokes or anti- Stokes lines is referred as the Raman frequency or Raman shift. The change in energy of scattered photon originates from the change in energy of the molecule or solid, therefore the vibrational energies of the molecule can be measured directly from the Raman shift [143].

2.1.2 Resonance Raman Scattering

Resonance Raman (RR) scattering occurs when a laser beam frequency lies in the vicinity of the vibrational levels of the excited electronic state, in that case the so called 'virtual state' (ν'_0) lies between the continua of these vibrational levels, figure 2.1. The RR scattering process must not be confused with absorption, where a transition occurs between the real (quantized) electronic states of the molecule or solid and is shown by a pure electronic transition of energy, ΔE, in figure 2.1. In the decay of a pure electronic transition, between a real excited electronic state and the lowest vibrational level of the ground electronic state the phenomenon of fluorescence is observed instead as shown in figure 2.1. The RR scattering is a fast process, as the lifetime of the excited state in RR is very short ($\sim 10^{-14}$s) as

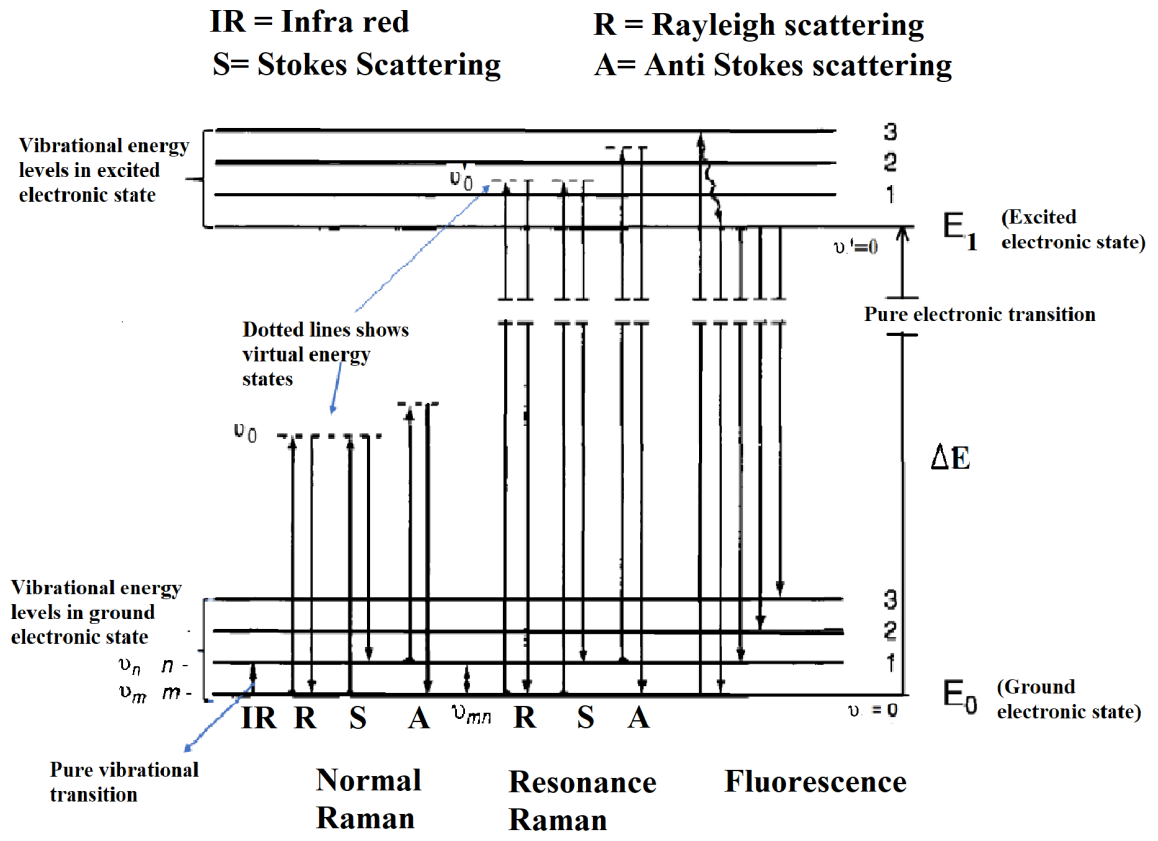

FIGURE 2.1: *Figure illustrates the origin of non-resonant Raman, Resonance Raman and Fluorescence processes.* Image adapted from section 1.4 of Ref [144].

compared to the slower fluorescence process which has a much longer lifetime (~ 10^{-8}s to 10^{-5} s). The RR scattering process enhances the number of scattered photons by up to 10^3 - 10^5 compared with non-resonant Raman scattering [141, 144]. Due to the resonance effect the Raman signal from even a single layer of graphene becomes detectable [145].

2.1.3 The Raman Spectrum of Graphene

Raman spectroscopy has been established as the most powerful and non-destructive tool, for determining the structure of graphene. We can get a wide range of information about the number of layers, thickness, doping level, and defects by understanding the Raman spectrum of graphene.

2.1.3.1 Phonon dispersion in graphene

In order to fully interpret the Raman spectra of graphene, let us first consider phonon dispersion in this material. The unit cell of graphene consists of two inequivalent carbon atoms (located at site A and B figure 1.4), having three vibrational degrees of freedom per atom, which gives rise to six phonon branches. Three of the branches describe acoustic (A) or in-phase and the other three optical (O) or out-of-phase vibrational modes of these atoms.

Further, each mode is categorised into longitudinal (L) or transverse (T) motion according to whether the atomic vibrations are parallel with or perpendicular to, the carbon - carbon direction, respectively. One vibration from each transverse mode is perpendicular to the plane of the carbon - carbon bonds or graphene plane and is thus regarded as an out-of-plane mode and described as an out-of-plane transverse optical phonon (oTO) or an out-of-plane transverse acoustic phonon (oTA). The vibration of the two atoms in each mode can be in parallel with carbon-carbon bonds in the graphene plane giving rise to longitudinal acoustic phonons (LA) and longitudinal optical phonons (LO) which are in-plane. In-plane vibrations perpendicular to the carbon-carbon direction from each mode comprise the in-plane transverse acoustic phonons (iTA) and in-plane transverse optical phonons (iTO). The atomic vibrational modes, Raman spectrum and associated phonon dispersion spectrum for monolayer graphene is illustrated in figure 2.2(a)(c).

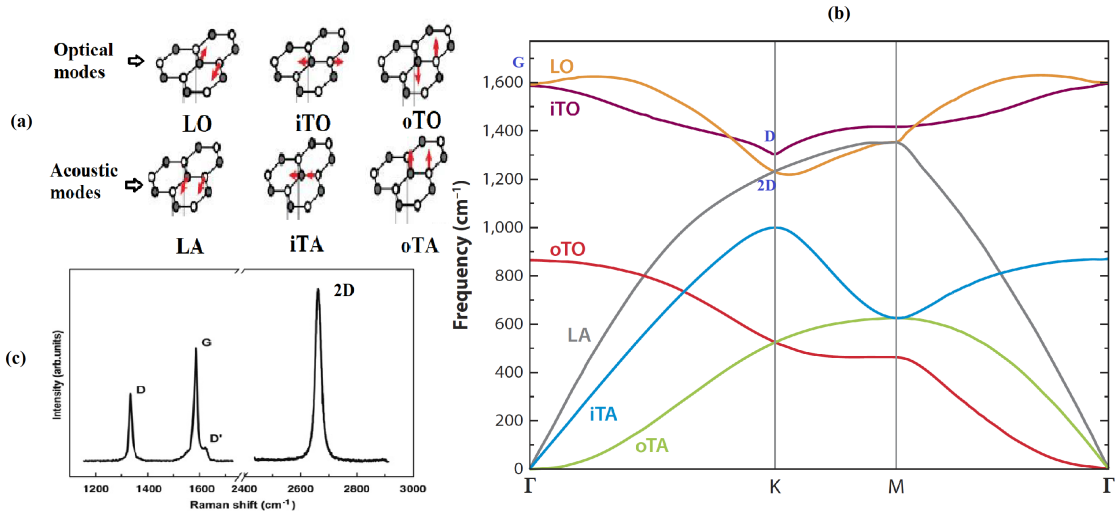

FIGURE 2.2: *(a) Atomic vibrational modes in graphene; (b) Calculated phonon dispersion of graphene; (c) Raman spectrum of graphene showing G, D, D′ and 2D bands.* Image adapted from Ref [145–147]

The prominent bands in the Raman spectrum of pristine graphene are the *G* band and the 2*D* band, which can be seen at approximately 1582 cm^{-1} and 2700 cm^{-1} respectively as shown in figure 2.2. Two other bands, the *D* and *D′* bands, are associated with defects in graphene and are not observed in pristine samples. These defects can originate from dangling bonds, edges, randomly distributed charges on the surface of the sample or doping [148–150]. The *G* band can be assigned to the in-plane modes iTO and LO (which arise from streching of σ-bonds), which are degenerate at the Γ point of the Brillouin Zone. The *G* band arises from a normal first order resonant Raman scattering process, figure 2.3 (a). The phonon modes around the K point are of particular interest because they give rise to the *D* and 2*D* peaks. The 2*D* peak is associated with the LO and LA phonon branches, which meet each other at the K point of the BZ, resulting in a doubly degenerate phonon mode [145, 146].

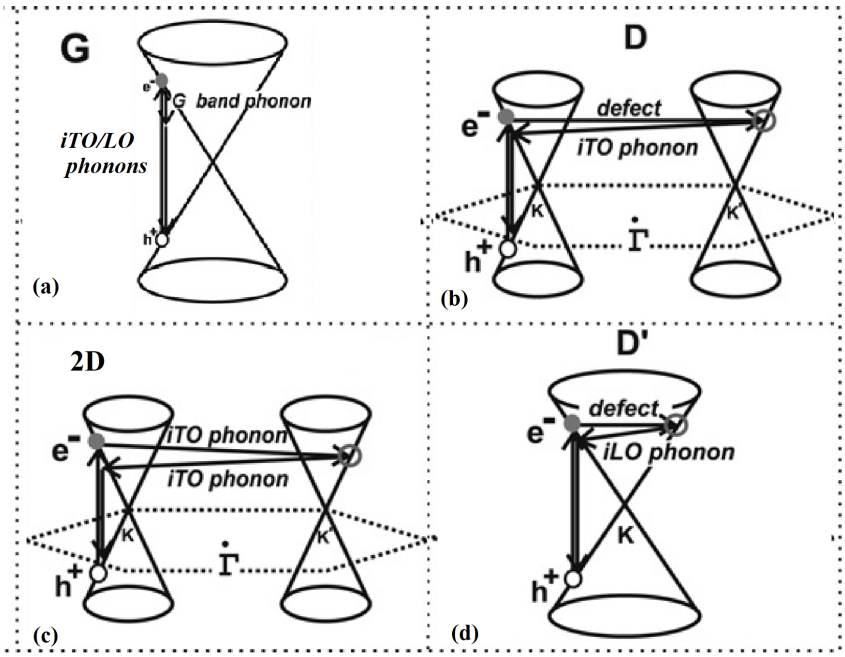

FIGURE 2.3: *(a) A first order Raman process in graphene giving rise to the G-peak, due to scattering of a photon by iTO and LO phonons; (b) The mechanism of the DR process originating from elastic scattering from a defect at the K point of the BZ followed by inelastic scattering byan iTO phonon at K', resulting in the D-peak; (c) The DR process for the 2D-peak arises from inelastic scattering of two iTO phonons at the K and K' points of the BZ; (d) The intravalley DR scattering process involving a defect and iLO phonon.* Image adapted from Ref [146].

2.1.3.2 Double Resonance Process in Graphene

The *D*-peak (~1350cm^{-1}) is only visible in the Raman spectrum of graphene when a defect is introduced in the crystal lattice. The peak arises due to a double resonance (DR) Raman scattering process involving one iTO phonon and one crystal defect near the K point. The iTO branch phonon (which originates from the breathing mode of six carbon atoms) is non-degenerate. By examination of two inequivalent Dirac cones located at the K and K' points of the Brillouin Zone, figure 2.3(b), we can describe the DR process in four steps:

1. The DR event starts from the excitation of electron by the incident photon, from a real electronic state to another real electronic state leading to the creation of electron - hole pair, shown by the up arrow in the left cone in figure 2.3(b).

2. The excited electron is scattered elastically by a defect in the crystal to another electronic state in an equivalent Dirac cone (intervalley scattering) as shown by the right arrow in the figure.

3. The electron is inelastically scattered back to the original valley by an electron-phonon interaction and the process is shown by left arrow in the figure.

4. Finally, the emission of a photon takes place and the electron recombines with the hole as shown by the down arrow in left cone.

Two seperate events take place in this DR process, one is an elastic scattering event caused by a defect of the crystal and the other an inelastic event caused by electron-phonon interactions. The process is doubly resonant as two of the intermediate states correspond to real electronically excited states within the graphene. The DR process leading to the 2*D* band is similar as that for the *D* band except that both scattering events are inelastic, caused by interaction of electron with two phonons of equal and opposite wavevector as shown in figure 2.3(c). Due to the different scattering mechanisms, the *G* band and 2*D* band can be present in the graphene spectrum even if the *D* band is abscent. The symmetry that exist between the conduction and valance bands can lead also to triply resonant (TR) scattering for the 2*D* band and has been suggested as the origin of the intensity of the 2*D* band compared with the *G* band in graphene monolayers [43]. Another weak feature due to disorder in graphene is termed the *D*' band, which appears at 1620cm^{-1}. It also originates from a DR process, but in this case an electron is scattered into a state within the same Dirac cone (intravalley scattering) around the K or K' point. This process also involves one defect and one iLO phonon, as illustrated in figure 2.3(d).

More complex DR processes occur in the bi and tri-layered graphene as compared with monolayer graphene. For a typical graphene monolayer, a narrow single Lorentzian profile can be fitted to the 2*D* peak [151]. The 2*D* band splits into four components for bilayer graphene since the band structure now allows four different DR scattering processes. For tri-layer graphene , fifteen transitions are possible, many of which are very close in energy resulting in a minimum of six peaks for a correct description of the lineshape.

2.1.3.3 The Quality of Graphene

Information about the quality of a graphene sample can be obtained from the intensities and profiles of the peaks described above. For example, the intensities of the *D* and *G* peaks could be useful in approximating the flake size of graphene [152, 153]. Assuming the intensity of the *D* peak is arises only from edge defects, Tuinstra and Koenig [153] noted that the ratio of the intensities of the *D* and *G* peaks, I_D/I_G varied inversely with the grain size, which could be used to determine the size of crystallites by the following relationship:

$$L_a = (2.4 \times 10^{-10})\lambda_{laser}^4 (I_D/I_G)^{-1}, \tag{2.1}$$

where L_a is the mean diameter of the grain in two-dimensions, I_D is the intensity of *D* peak, I_G is intensity of the *G* peak and λ_{laser} is the wavelength of the excitation laser. Similarly, the intensity, profile and the shift in frequency of the 2*D* peak is helpful in deciding the number of layers and stacking order [146, 151, 154]. The 2*D* peak in pristene graphene is roughly four times as intense as the *G* peak so the ratio of intensities of the 2*D* and *G* peaks (i.e., I_{2D}/I_G) has been suggested as being useful in identification of monolayer material. However, the presence of defects can alter the 2*D* to *G* ratio as can uncontrolled doping in pristene samples [155], therefore it is recommended to use line shape rather than the intensity to explore layer thickness [152]. One way in which the 2D peak can be used to determine the number of layers in a graphene sample is via the FWHM (full width at half

maximum). The FWHM value for monolayer graphene, as calculated by Park *et al* [156], is 24 cm^{-1}, which becomes almost double (50 cm^{-1}) for the 2*D* peak for the bilayer graphene. As described in section 2.1.3.2, the 2*D* peak for bilayer can be fitted with four Lorentzians, however two of the components are degenerate therefore three are sufficient to describe the bilayer and five for the corresponding trilayer [156]. Indeed, using the 2*D* lineshape, it is possible to identify samples with up to five layers of graphene with Raman spectroscopy. However, above five layers the change in electronic structure is small, so material containing more than five layers is indistinguishable from graphite [147, 151]. In the case of a randomly stacked structure (turbostratic graphite), the reduction in interlayer interaction between the graphene planes diminishes the spliting of the 2*D*-band leading to a much smaller I_{2D}/I_G ratio and a 2*D* peak, which can be fitted by a single Lorentzian as in monolayer graphene, but with a larger FWHM (~ 45-60 cm^{-1}) [150]. Furthermore, the electron-phonon interaction depends on the energy and momenta of the electrons and phonons, therefore the relative intensities of different components of the 2D band are also dependent on excitation energy.

Raman spectroscopy can probe disorder through defect-activated features, arising from symmetry breaking in the lattice as described above for the *D* band. Different types of defects can occur such as edges, grain boundaries, vacancies, intercalated atoms, as well as changes in carbon hybridisation states, e.g. from sp^2 to sp^3. The nature and quantity of defects depends strongly on the method by which the graphene is produced. In general, it is difficult to determine the precise nature of the defects in a graphene sample from Raman scattering, since all break symmetry. However Eckman *et al* [157] have shown that the ratio of the defect-related *D* and *D'* band intensities can differentiate between edge, vacancy and hybridisation defects.

2.1.4 The Raman Spectrum of MoS_2 and other TMDC

In recent years, Raman spectroscopy has been developed as a reliable characterisation tool for other 2D materials, beyond graphene. The Raman spectra of TMDCs show well defined Raman fingerprints.

Recalling the structure of MoS_2 described in section 1.2.3.1 in chapter 1, the unit cell of MoS_2 is hexagonal, with a layer of Mo atoms sandwiched between the two layers of sulphur (S) atoms. Interaction with the laser beam gives rise to four Raman active modes for MoS_2, which are present at 32 cm^{-1}, 286 cm^{-1}, 383 cm^{-1} and 408 cm^{-1}, which are labeled by symmetry as E^2_{2g}, E_{1g}, E^1_{2g} and A_{1g} respectively [158]. The energy, width, and amplitude of these vibrational modes are strongly effected by the change in thickness of exfoliated MoS_2, thus providing a reliable means to determine the exact number of layers in MoS_2 flakes [159].

It can be seen in figure 2.4(b), that the clear Raman peaks for in-plane E^1_{2g} and the out-of-plane A_{1g} vibrational modes are present at all thicknesses (from bulk to monolayer) of MoS_2. As the thickness of the sample is increased, the E^1_{2g} line is redshifted while the A_{1g} mode is blueshifted, and the rate of change in frequency is double for A_{1g} as that for E^1_{2g}. This results in an increase in separation between the modes from 19 cm^{-1} to 25 cm^{-1} in going from the monolayer to the bulk MoS_2, respectively [159, 160]. The changes in the position of

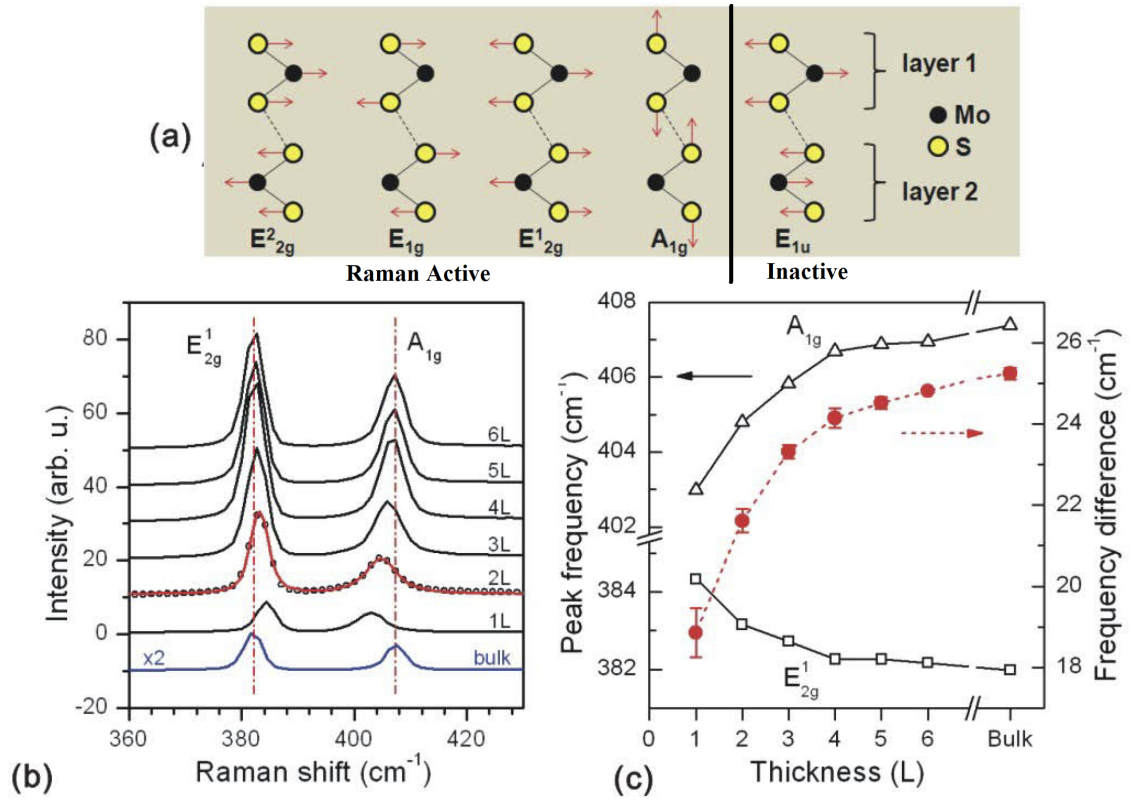

FIGURE 2.4: *(a) Different atomic vibrational modes of MoS_2; (b) Raman spectra of MoS_2 with varing thickness, clearly showing the shift in frequency depending on thickness; (c) Frequencies of E^1_{2g}andA_{1g} Raman modes (left vertical axis) and their difference (right vertical axis) as a function of thickness.* Image adapted from Ref [159].

Raman peaks with the number of layers described above are most readily observed when using a 532 nm or shorter wavelength excitation. At very low frequences, it is observed that the E^2_{2g} shifts progressively from 32 cm^{-1} in the bulk to 23 cm^{-1} in a single layer of MoS_2 [160, 161]. However, such low frequencies are below cut off of the filters used in many Raman spectrometers, including that in our work. Therefore, it can be concluded that the frequencies of the E^1_{2g} and A_{1g} lines can be used as a key indicator to identify the number of layers in few layer (up to four) MoS_2 samples.

The A_{1g} peak in $MoSe_2$, at 240 cm^{-1}, is about 150 cm^{-1} lower than that of MoS_2 and is also sensitive to the number of layers in a sample. A single Raman peak for monolayer and bilayer $MoSe_2$ appears, as shown in figure 2.5, which splits into two for three and four layer material, and three Raman lines appear for five layers of $MoSe_2$. The Se atoms in all layers oscillate in phase with respect to the corresponding centre Mo atom, which does not move in the A_{1g} mode. The splitting occurs due to a variation in the number of phase shifts (of 180°) between the layers. The increase in frequency for increasing number of layers is due to interlayer interactions. Contrary to the MoS_2 Raman spectrum, the in-plane E^1_{2g} mode for $MoSe_2$ appears at higher frequencies, to the right hand side of the A_{1g} mode, at 287.2 cm^{-1} for the monolayer and 285.9 cm^{-1} for the bilayer, with a decrease in intensity with increasing number of layers. However, this mode shows same redshift in frequency with increasing

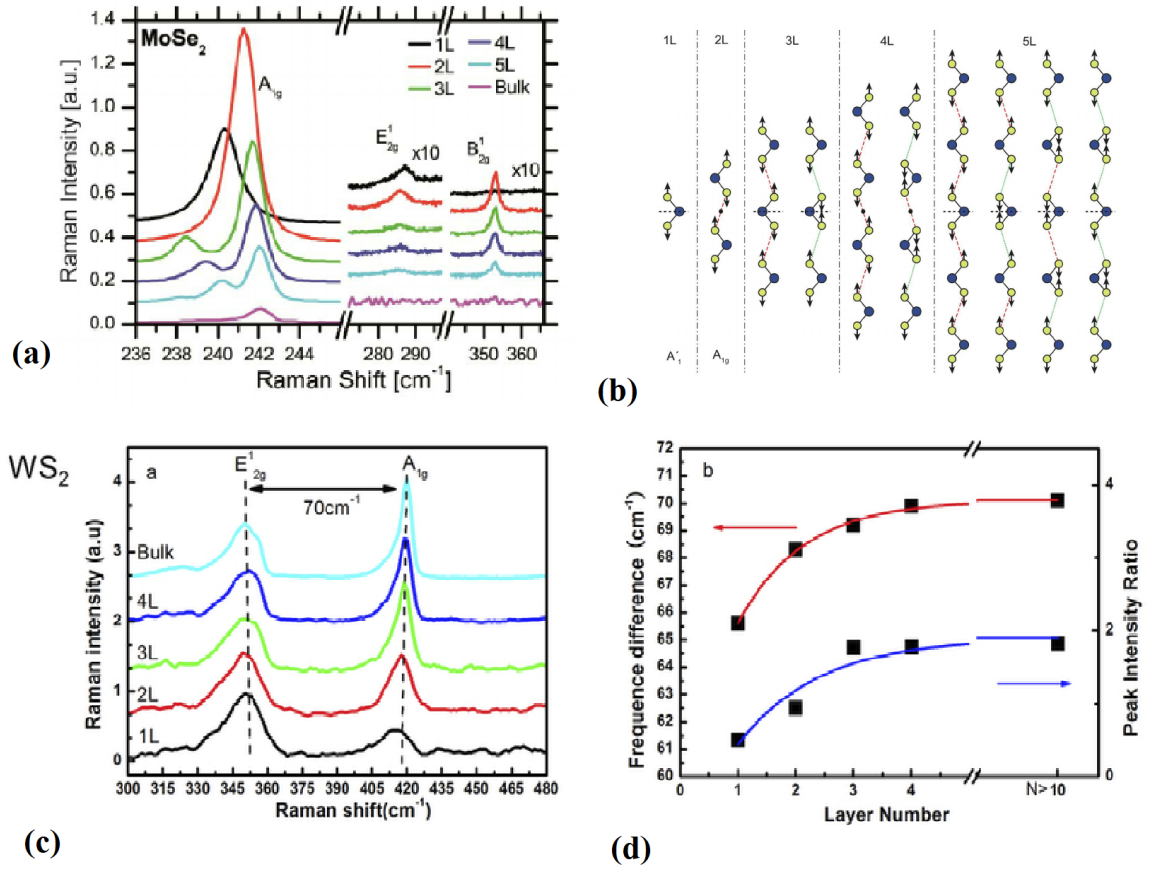

FIGURE 2.5: *(a) Raman spectra of the bulk and few layer $MoSe_2$ shows the shift in frequency and intensity of A_{1g} mode as function of layer thickness; (b) Schematic illustration of the Raman active out-of-plane mode A_{1g} in 1 to 5 layers of $MoSe_2$; (c) Raman spectra of bulk and few layer WS_2; (d) The frequency difference (red) of E^1_{2g}andA_{1g} Raman modes (left vertical axis) and their peak intensity ratio (blue line read w.r.t right vertical axis) as a function of layer thickness in WS_2.* Image adapted from Ref [161, 162]

number of layers as that in MoS_2. The breakdown in translational symmetry in few layer $MoSe_2$ results in the activation of another peak at 353 cm^{-1} (B^1_{2g} mode), as compared to the corresponding bulk material, where this mode is inactive [161].

Similarly, in WS_2, the E^1_{2g} mode appears at 350 cm^{-1} and the A_{1g} mode at 420 cm^{-1} with a frequency difference of around 70 cm^{-1} in the bulk material. Decreasing the number of layers produces a negligible shift in the frequency of the E^1_{2g} mode, while a redshift in the frequency of A_{1g} is seen, as shown in figure 2.5(c). That leads to a frequency difference of 65.5 cm^{-1}, 68.3 cm^{-1}, and 69.2 cm^{-1} for monolayer, bilayer and trilayer, respectively. This frequency difference becomes constant (70 cm^{-1}) above four layers. The ratios of the intensities of A_{1g} and E^1_{2g} peaks are 0.5, 1.0 and 1.8 for monolayer, bilayer and trilayers, which can also be used as an indicator to determine the number of layers in the sample under investigation. The difference in frequencies and the ratio of intensities of A_{1g} and E^1_{2g} mode as a function of number of layers are shown in figure2.5(d) [162].

2.1.5 RM-1 Raman Spectrometer

Figure 2.6 shows the top view of the Raman spectrometer (RM-1) used for Raman characterisation of the samples presented in this work. This spectrometer is equipped with a 200 mW green laser (532 nm), a 10x objective lens (which demagnifies the laser beam at the sample), an adjustable moving stage (which moves along the lens axis, and is used to get the best focus of the laser on sample) and optical components to collect and process the scattered light. The intensity of the laser beam can be varied manually from the laser beam power supply. The scattered beam is analysed by a thermoelectrically cooled CCD spectrometer with a resolution of 12 cm^{-}1. The laser beam diameter at the sample position was measured

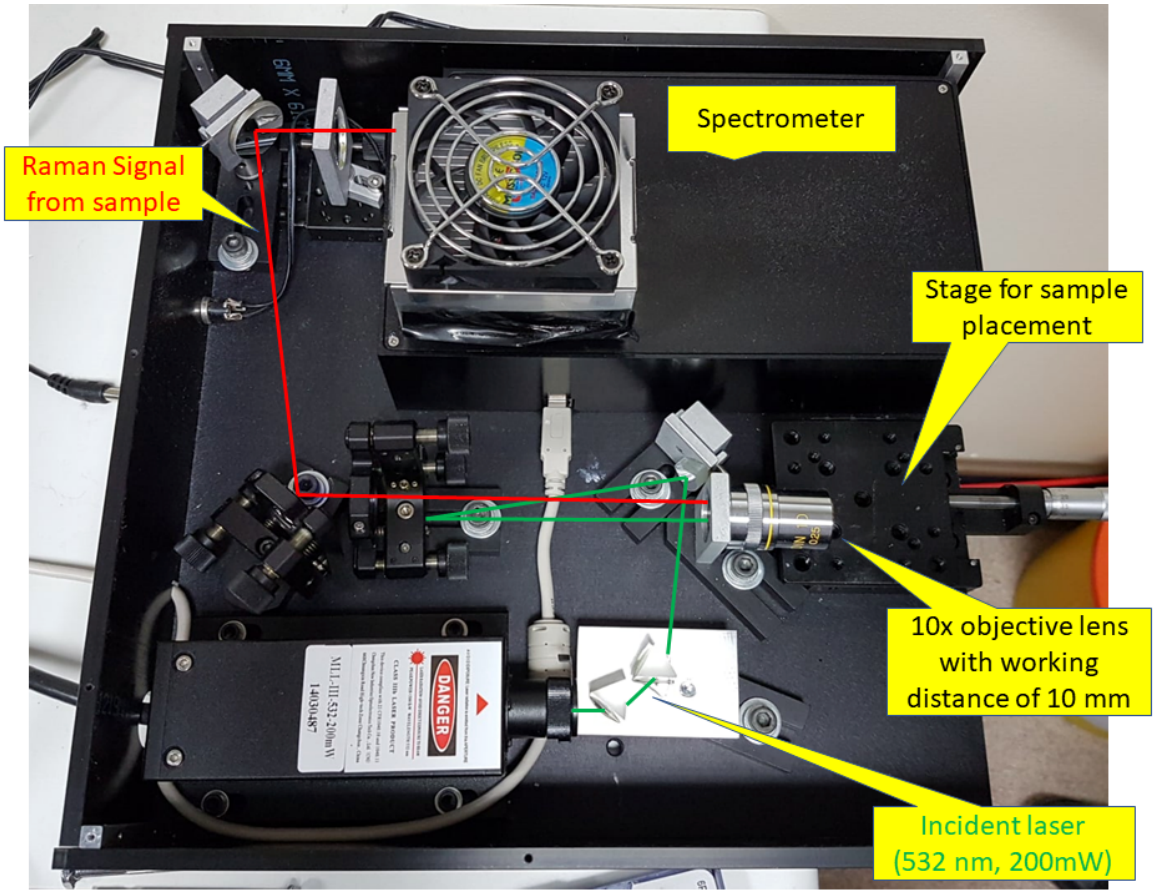

FIGURE 2.6: *Top view of Raman spectrometer (RM-1) with cover removed.* Image adapted from Ref [163].

to be ≈0.02 cm and , under typical operating conditions the laser power density at the sample was about 1.5×10^{4} W cm^{-2}, which is comparable to values reported in the literature. The Raman spectrometer was calibrated every few weeks by taking the spectrum of a SiC sample, which was then compared with the standard SiC spectrum from the literature. A second order polynomial equation is obtained after comparison and applied to the data measured for all of the samples presented in this work.

2.1.6 Construction of a 3D motorised stage and sample holders for the Raman Spectrometer

The RM-1 Raman spectrometer was upgraded by adding a motorised stage in order to probe several areas of a sample and obtain a clear picture of the uniformity of thin films and heterostructures. Originally the spectrometer stage was capable only of movement along the axis of the objective lens, under manual control, to assist in focusing the laser light on the samples and no other motion was possible. This was a major restriction in investigating the uniformity and extent of any deposited material or to locate small flakes or islands. Therefore, an important task was the construction of new stage. The stage was designed to be flexible in terms of sample type and size, with a requirement that both solid and liquid samples (the latter held in a cuvette) be measured. Solid samples could range from thin films and foils a few square mm in area to films deposited on glass slides. It was therefore decided that two multipurpose sample holders would be built, one of which capable of carrying a standard microscope glass slide, with both having multiple tapped holes through which copper-berylluim springs could be mounted to clamp samples in the vertical orientation required by the spectrometer design.

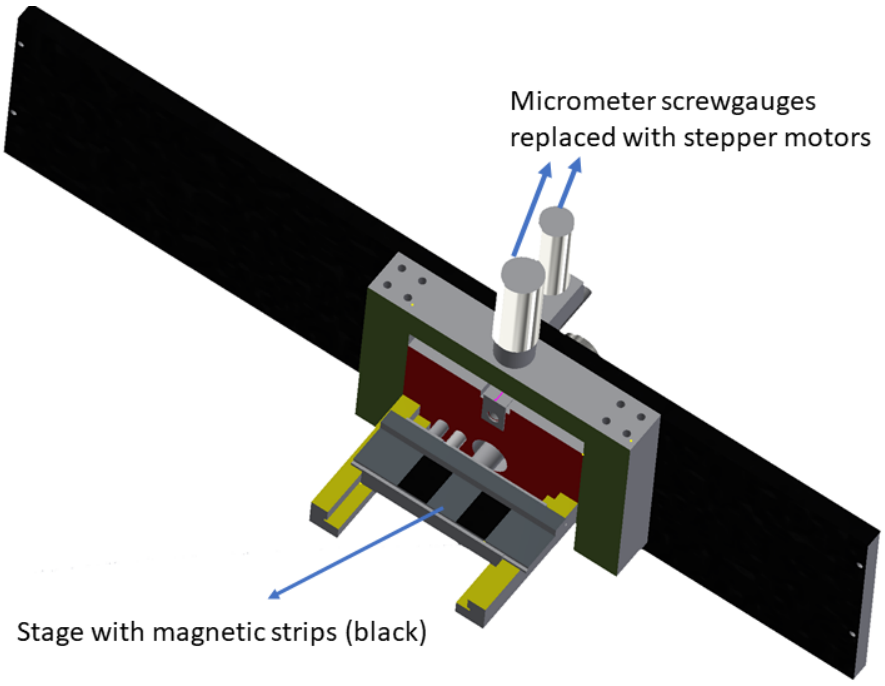

FIGURE 2.7: *The original design of 3D moving stage made in Autodesk Inventor. Micrometers were replaced with stepper motors in the final design.*

A three-axis stage with stepper motors driving the axes perpendicular to the direction of the incident laser beam in which the sample holders could be held with the magnet were designed using Autodesk Inventor figure 2.7. Components were fabricated by the Mechanical workshop in the Physics Department of Durham University and a stepper motor controller built by the Electrical Engineering Workshop also within the Physics Department. Once the components were fabricated the stage was assembled, mounted on the spectrometer (figure

2.8) and tested. The vertical motion could move the sample with a minimum step size of 0.155 ±0.0005μm and a coarser step of 3.75 ±0.25μm horizontally. Given that the demagnification with the 10x objective lens reduces the laser beam to only ~ 200μm in diameter (a much larger footprint than in a commercial Raman microscope) such a step size is small enough not to limit the spatial resolution which can be achieved with the modified spectrometer.

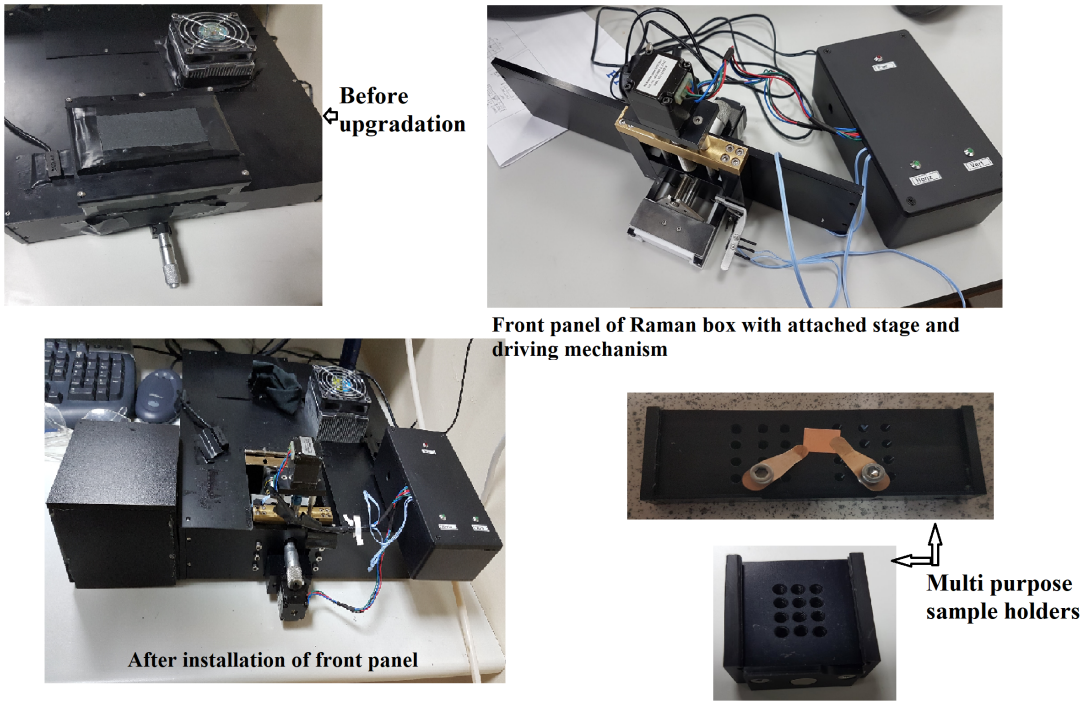

FIGURE 2.8: *Different stages of upgrade of the Raman spectrometer and the sample holders.*

2.2 Ultraviolet-visible Spectroscopy

Ultraviolet-visible (UV-vis) spectroscopy refers to absorption spectroscopy in the ultraviolet-visible spectral region. Interaction of photons having an energy corresponding to the difference between two real electronic states or the bandgap between valence and conduction band of a molecule or solid, leads to the creation of an excited state by absorbing the photon. The process is referred to as "absorption", and it is the change in intensity of a beam passing through the material which is measured in absorption spectroscopy. The emission of a photon by relaxation of molecule from its excited state to the ground state is 'Photoluminescence (PL)'. The energy of the emitted photon depends on the energy gap of the material, and by measuring the frequency of emitted radiation the band gap energy could be determined.

2.2.1 Photoluminescense in Few layer TMDCs

As described in chapter 1, layered TMDCs show a transition from indirect bandgap to direct band gap semiconductors upon reducing their thickness from the bulk to the monolayer

of the corresponding material. The monolayers of these materials exhibit strong PL, which changes inversely with the number of layers and diminishes in their bulk materials [85, 161, 162], therefore PL also provides another indicator for the thickness in the layered TMDCs. The PL originates from direct gap excitonic transitions between the maxima of split valence bands (v_1, v_2) and the minimum of the conduction band, all of which are located at the K point of the Brillouin Zone, and labelled as A and B in the literature.

In bulk MoS_2, no PL is observable, as compared to its mono and bilayers which show significant PL. The PL spectrum of suspended monolayer samples show a single narrow feature of width (~50 meV) centered at an energy of 1.90 eV. In contrast, few layer samples display multiple emission peaks (A, B). Peak A of few layer samples coincides with the monolayer peak A while Peak B lies about 150 meV above peak A. Peak A redshifts and broadens slightly with an increasing number of layers [85, 86] figure 2.9(a). In bulk

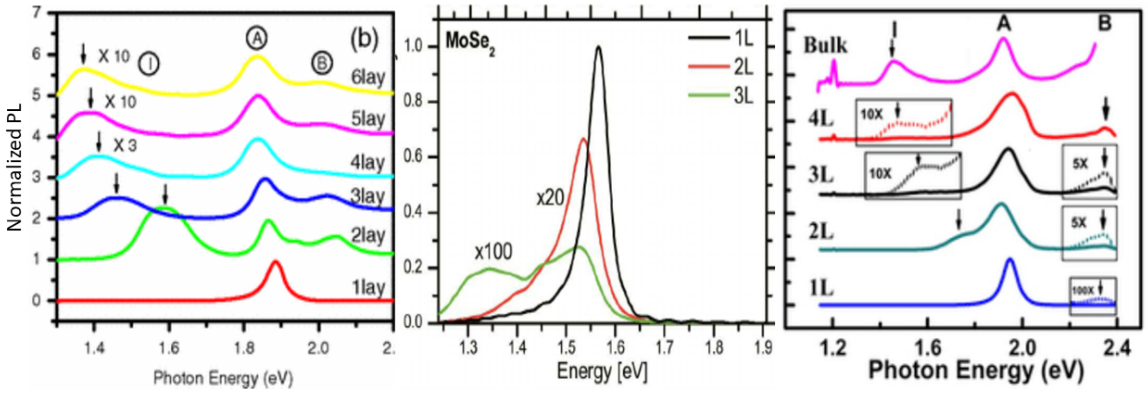

FIGURE 2.9: *(a) Photoluminescence of MoS_2 from monolayer to 6 layers; (b) Photoluminescence of mono, bi, and tri layer $MoSe_2$; (c) Photoluminescence of WS_2 as a function of the number of layers (d).* Image adapted from Refs [85, 161, 162]

$MoSe_2$ the indirect gap energy (1.1 eV) is in the near-infrared region, with the direct A and B excitations at higher energy (1.57 eV (790 nm) and 1.82 eV (682 nm)). The observed PL emission from monolayer and bilayer $MoSe_2$ exhibit prominent maxima at 1.57 eV (792 nm) and 1.5 eV (807 nm), respectively. For the monolayer the PL intensity is in excellent agreement with the known direct A exciton in the corresponding bulk material. PL intensities from the monolayer material are 10 - 20 times stronger than those of the bilayer material. The emission from the trilayer material shows two broad maxima at 1.53 and 1.3 eV (812 and 922 nm) which arise from the spliting of the valence band [161] figure 2.9(b).

Similarly, WS_2 also shows strong PL as the thickness decreases from the bulk material (where extremely weak PL is observed) to the monolayer. Monolayer WS_2 has much brighter PL, double in intensity, as compared to its bilayer. In contrast to MoS_2 monolayers, both A and B peaks appear in PL from the monolayer of WS_2. This is due to the splitting of the valence band (by 0.43 eV) in monolayer of WS_2 [162] figure 2.9(c).

2.2.2 Absorption Spectrum

If the energy of an incident photon matches the energy difference, ΔE, between the ground and excited states of a molecule or solid, the photon may be absorbed and promotes the molecule or solid to an excited state. Hence, when a beam of light with a wide range a frequencies, from the ultraviolet to visible region of spectrum, passes through a solid, liquid or gas, measurement of the attenuation of that beam as a function of frequency provides a measurement of the photon-energy dependent absorption of the sample. The resulting spectrum therefore measures transitions from the ground state to excited state(s) while, in constrast, photoluminescence deals with transitions from the excited state to the ground state.

By measuring the absorption one can determine the concentrations of liquid solutions or dispersions of 2DLMs through using the Beer-Lambert Law, which states that the concentration of a substance in solution is directly proportional to the 'absorbance ', A, of the solution. Mathematically, we can write this as:

$$A = \alpha \times C \times l, \tag{2.2}$$

where α is the absorption coefficient, C is concentration and l is the path length of the cell (aliquot). The law is only true for monochromatic light, that is light of a single wavelength or a narrow band of wavelengths, and provided that the physical or chemical state of the substance does not change with concentration. When monochromatic radiation passes through a homogeneous solution in a cell, the intensity of the emitted radiation depends upon the thickness (l) and the concentration (C) of the solution.

Experimental measurements are usually made in terms of transmittance (T) which is the ratio between the intensity of the incident radiation I and the intensity of the transmitted radiation I_0, and expressed as a percentage ($\%T$). If all of the incident radiation is passed through the sample and zero absorption has occurred, transmittance will be 100% while the value of absorbance will be 2 for 1% transmission of radiation and could be infinite for zero percent transmittance of radiation. The relation between absorbance and transmittance is:

$$A = log_{10}\frac{I_0}{I} = log_{10}\frac{100}{T} \tag{2.3}$$

or it can be written simply as $A = 2 - log_{10}\%T$ and used for calculation of absorbance from the percentage transmittance. The liquid suspension of the 2DLM(s) is usually put in a cuvette and placed in the path of the incident radiation and detector. The intensity of transmitted radiation from the solvent is measured and stored internally in the spectrometer for background subtraction.

2.2.3 UV-vis spectrometer

Figure 2.10(a) shows the UV-3600 spectrophotometer used for the measurement of absorption and transmission spectra of samples presented in this work. The spectrophotometer is capable of measuring a broad range spectrum from 165 nm to 3300 nm. This spectrometer

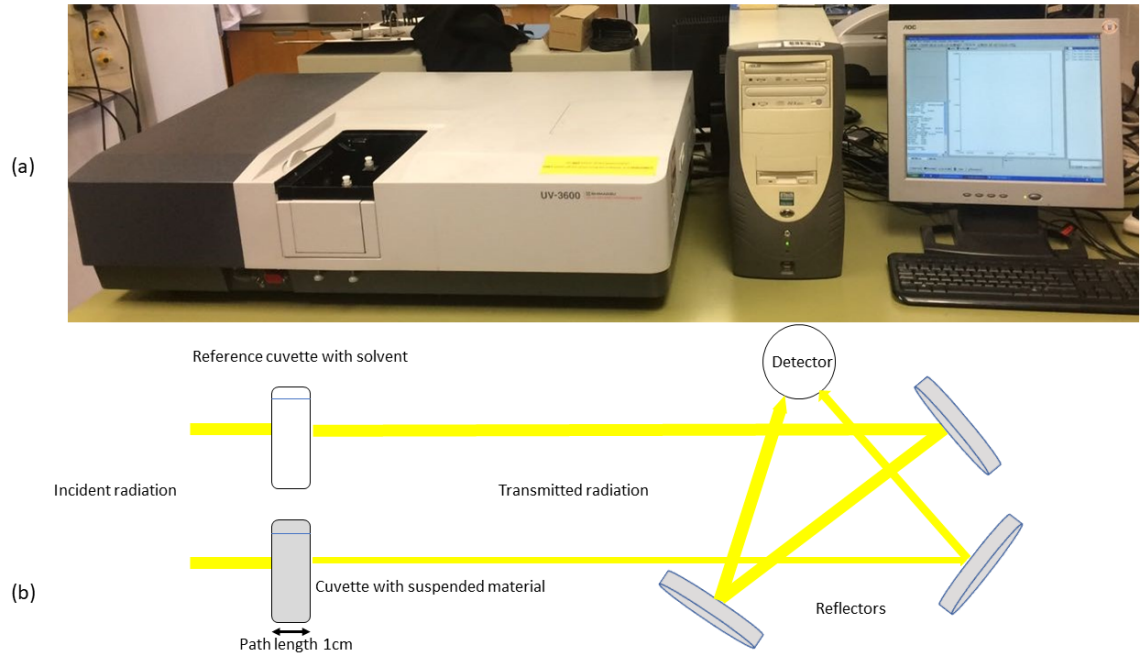

FIGURE 2.10: *(a) UV-3600 UV-VIS-NIR Spectrophotometer; (b) Schematic illustration of the spectrometer operating principle.*

uses a photomultiplier tube (PMT), InGaAs detector and PbS detector for measurement of UV-visible (165 - 750 nm), near infrared region (NIR, 750 - 1600 nm) and IR (1600 - 3300 nm) light, respectively. The spectrophotometer comes with wide range of accessories to measure the transmittance and reflectance of radiation through solid films and liquid suspensions or solutions. The data is plotted in specialised LabView software via an attached computer system. Figure 2.10(b) presents a schematic illustration of the operation of the spectrometer. The incident beam is split into two equivalent beams by optical components (not shown) and passes through two compartments. One of these compartments contains a cuvette with the reference solvent for background substraction, while the other contains a cuvette in which the suspension is placed. The spectrometer measures the diffrential intensity between the transmitted beams and absorbance can be measured using equation 2.3. With knowledge of the absorption coefficient of the 2DLM at a particular wavelength, its concentration in the suspension can be found.

2.3 Scanning Electron Microscopy (SEM)

In 1926, Busch showed that electric and magnetic fields could act as lenses for charged particles, thus providing the basis for electron microscopy. The first true SEM was described and developed in 1942 by Zworykin, who showed that secondary electrons (SE) provided topographic contrast and successfully achieved a resolution of 50 nm. Further improvements were made in subsequent years leading towards the development of first commercial SEM which had three magnetic lenses and a Everhart-Thornley detector (ETD) for secondary electrons, in 1965. Modern SEMs are not very different from this first instrument [164].

The SEM is one of the most versatile instruments in material science, being employed for the examination and analysis of microstructures in vast and diverse fields such as scientific and medical research, forensic investigations and semiconductor quality control. A modern SEM provides an image resolution from around 1 nm to 10 nm, having large depth of focus ($\sim$ 2μm) which can be used for 3D imaging of the sample [165]. It is primarily used to study the surface, or near surface, structure of a sample using a beam of medium energy (1-50 keV) electrons, which is rastered along orthognal directions by driving electromagnetic coils (scan coils) [166]. A schematic diagram showing the major components in a SEM, is given in figure 2.11.

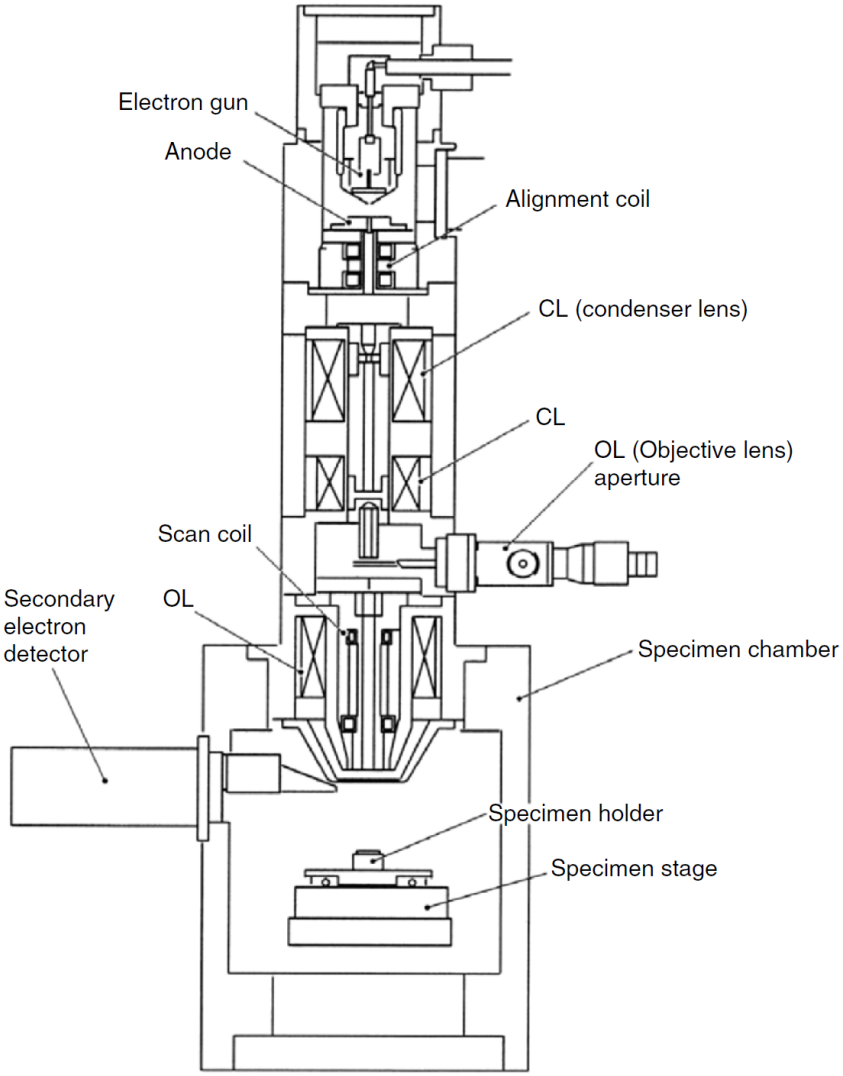

FIGURE 2.11: *Schematic diagram of a scanning electron microscope.* Image adapted from Ref [163].

A conventional SEM comprises an electron gun and a series of electromagnetic lenses (two condenser and one objective lens) and apertures, assembled in a column structure as shown in figure 2.11. A tungsten filament, or else a LaB_6 or Schottky emitter, or a tungsten

field-emission tip is usually used as the electron source. The electrons are accelerated by a rotationally symmetric electric field generated through the magnetic lenses, after this the accelerated beam passes through the objective lens which demagnifies the electron beam to between ~2 nm to 10 nm in diameter (to determine the maximum possible resolution) until it hits the specimen [167]. The interaction of the beam with the specimen produces a number of signals, such as secondary electrons (SE), backscattered electrons (BSE), X-rays, specimen current, Auger electrons, cathodoluminescence (CL) and electron-beam induced conductivity (EBIC), (figure 2.12(a)). The region within the material where the beam interacts is known as the interaction volume (figure 2.12(b)). This volume is pear-shaped and its size depends on a number of factors including the beam energy, spot size, angle of incidence and the material. Its size usually decreases with increasing atomic number in the sample and increases with increasing incident beam energy. The main SEM imaging methods involve the detection, collection, amplification and conversion of the signals into a visual image, derived from secondary electrons (SE) and backscattered electrons (BSE) originating within the first 2 μm of the sample surface, details of which are given in next sections.

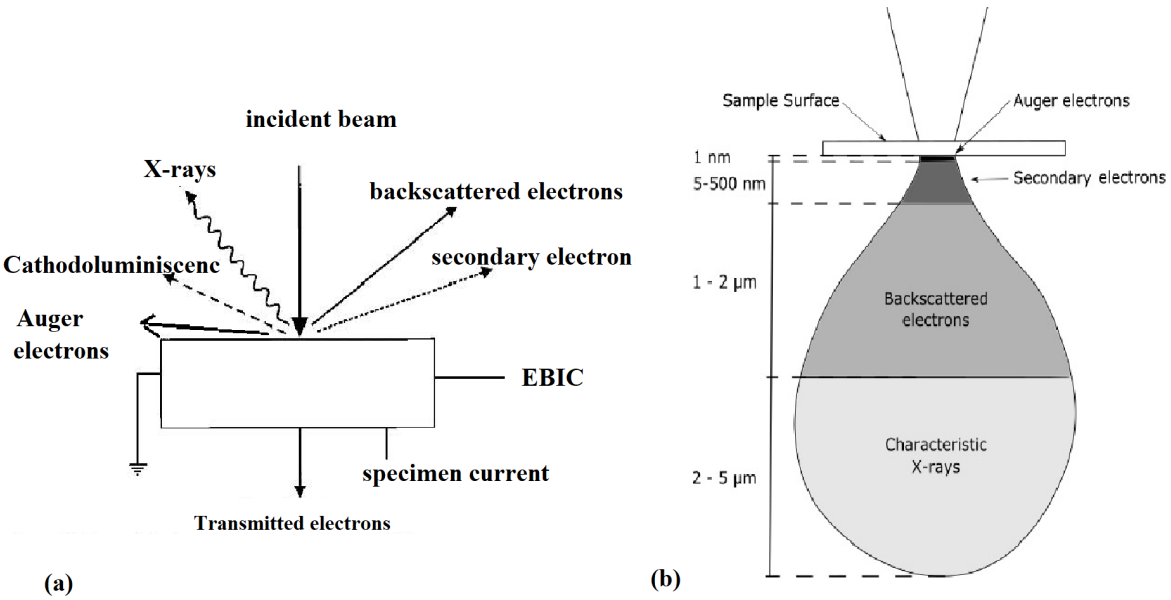

FIGURE 2.12: *(a) Schematic illustration of the interaction of an incident electron beam with the surface of a sample generating various signals; (b) The interaction volume and the regions from which the various signals can be detected.* Image adapted from Ref [166, 167].

2.3.1 Back Scattered Electron Imaging

Interaction of the focused incident beam of electrons with the surface of a sample results in the scattering of electrons which can be divided into elastic scattering and inelastic scattering. Elastic scattering is a consequence of the deflection of the incident electrons by atoms in the specimen. This kind of interaction results in a negligible loss of energy from the electrons during the collision and most of them deflect by angles of less than 90°. The small fraction of the incident electrons that are elastically scattered through an angle of more than 90° are

called backscattered electrons (BSE) and these can make their way out of the sample to a detector and are mainly used for compositional images. Their high energy enables them to escape from a much deeper level in the interaction volume, from depths of about 1 - 2 μm. The ratio of the number of backscattered electrons (n_{BSE}) emitted from the specimen to the number of incident electrons (n_i) is known as the backscattered electron coefficient (η),

$$\eta = \frac{n_{BSE}}{n_i}, \tag{2.4}$$

η is strongly dependent on the atomic number of the specimen. A specimen having higher atomic number, Z, emits a larger number of BSEs because of the lower penetration depth and significantly greater scattering near the surface, whilst lower Z materials have larger penetration depths, at which point electrons are considerably less likely to escape [163, 165]. An image formed by BSEs exhibits very useful compositional contrast if the specimen consists of more than one element. Any area in a specimen containing elements with higher atomic number will generate more BSEs therefore will be more bright. The difference in the number of BSEs collected by a detector will appear as differences in gray levels in a black and white image.

2.3.2 Secondary Electron Imaging

Secondary electrons (SEs) are weakly bound electrons ejected from atoms due to inelastic collisions of electrons in the incident beam within the specimen. The secondary electrons have an energy $E \leq 50$ eV, therefore, they can escape only from near the specimen surface with a depth of 5 to 500 nm, hence providing the primary source for surface topographic images. The average number of escaping SEs per incident electron is called the secondary-electron yield, δ, and is typically in the range from 0.1 to 10 depending on the energy of incident electrons E_0. δ decreases with increasing E_0 because higher energy electrons undergo more elastic scattering in comparison with inelastic scattering hence generating fewer SEs [165]. δ also depends upon the angle of the incident beam with the specimen surface, and is the lowest for perpendicular incidence, increasing with the angle between the incident beam and the surface. δ can be written in terms of the angle of the incident beam, ϕ as:

$$\delta(\phi) = \frac{\delta(0)}{cos(\phi)}. \tag{2.5}$$

Secondary electrons produced at lower depths are subject to further scattering from atomic nuclei and electrons, therefore can recombine with the holes resulting in a significantly lower probability of escape from the material. This causes the signal produced by secondary electrons to be highly surface sensitive and ideal for imaging raised or recessed features on surfaces. SEs are detected by a scintillator-photomultiplier system known as the Everhart-Thornley Detector or ETD. The secondary electrons strike a scintillator, e.g. a phosphor, which emits light which is then transmitted to a photomultiplier for generation of images [167]. Commonly, a topographic image is obtained by operating an SEM in SE mode.

However, it is possible to mix both SEs and BSEs to generate a mixed signal to contribute to topographic contrast, as used to image graphene by Yang *et al* [168].

2.3.3 FEI Helios NanoLab

To investigate the morphology, shape and particle size distribution of the flakes and deposited films presented in this thesis SEM was used. SEM images presented in the thesis are taken from the FEI-Helios Nanolab dual beam FIB/SEM system in the G.J. Russell Microscopy Facility at the University of Durham, figure 2.13. The instrument consists of a focused ion beam (FIB) column, an electron beam column, an evacuated chamber and a computer system. The sample is placed in an evacuated chamber on a stage and an electron beam is used to image the samples for this work (the FIB capability was not employed). A specialised software system was used for controlling the movement of the stage in the vacuum chamber, the current and voltage of the electron beam and the focussing of electron beam to a precise point on the sample. The Helios Nanolab system has thefacility to vary the incident beam from 350 eV to 30 keV with a maximum beam current of 22 nA, providing a resolution of 0.9 nm at a beam energy of 15 keV [169].

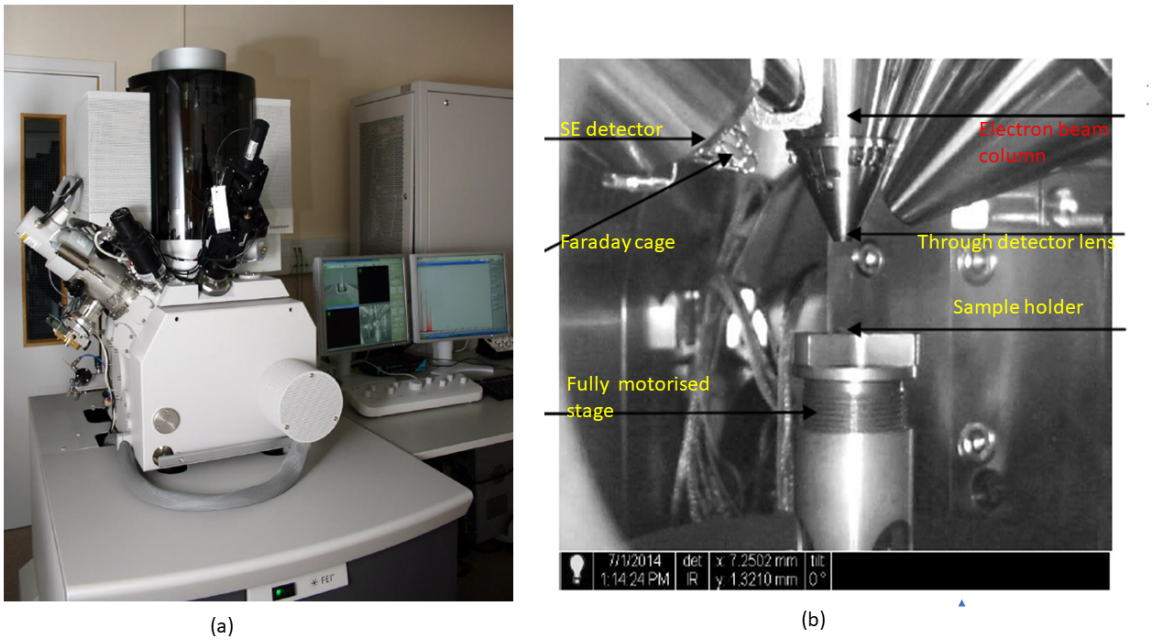

FIGURE 2.13: *(a) FEI Helios Nanolab system (b) Image of the vacuum (sample) chamber of the microscope.* Image adapted from Ref [169].

Chapter 3

Shear Exfoliation

The starting point for the deposition of thin films and heterostructures of 2DLMs by LB and LID is a suitable suspension (or solution) of platelets of the two dimensional solid of choice. As discussed in section 1.3 of chapter 1 there are a number of ways to achieve such materials, however, we adopt shear exfoliation [119–121] for the following reasons:

1. It is scalable and controlable as the concentration of dispersed material is dependent on the time for exfoliation and the initial amount of the materials such as graphite and surfactant [119, 120].
2. This method produces high quality graphene and in the literature it is found that no additional basal plane defects are introduced during exfoliation [119, 120].
3. Dispersions produced by shear exfoliation (in the presence of a surfactant in particular) are very stable, as thin platelets can be kept for years in suspension without precipitation [119].
4. It is a cost effective and cheap means of production as a liquid dispersion can be produced even using a simple kitchen blender and a common surfactant such as Fairy Liquid [119, 121].
5. It is generaliseable, as other layered materials beyond graphene can also be exfoliated by employing this method with little or no adaptation [119, 120].
6. Unexfoliated material or sediment can be recycled to maximize yield [119].
7. The method is environmentally friendly, as surfactant and solvent can be recovered with minimum loss, as shown by our work.

This chapter reports the production and analysis of surfactant stabilised solutions of graphene and presents initial data on the relationship between temperature, viscosity and concentration of exfoliated suspensions along with their interpretation. The exfoliation of

other two dimensional solids (MoS_2, $MoSe_2$, WS_2 and *h*-BN) used in this report was undertaken by A.G. Mathieson with Raman and SEM analysis performed by the author.

3.1 Shear Exfoliation of Graphene

Extending the work of Ref [170], surfactant stabilised dispersions of graphene were produced by shear exfoliation using a domestic blender. It has previously been demonstrated that concentration of shear exfoliated suspensions depend on: mixing time (t), rotation speed (N), mixing volume (V), rotor/blade diameter (D), and initial graphite concentration (C_i). However, Paton *et al* [119] concentrated their study on a limited number of organic solvents – N-methyl-2-pyrolidone (NMP) and N-cyclohexyl-2-pyrolidone (CHP), briefly studying surfactant stabilised aqueous solutions with sodium cholate as the (ionic) surfactant. Sodium-containing ionic surfactants have the major disadvantage that the sodium is very difficult to remove from nano-graphitic materials (M.R.C. Hunt, private communication) and may perturb their intrinsic properties. Hence a non-ionic surfactant was specifically chosen for this study. To the best of our knowledge there are no detailed studies of the influence of the concentration of non-ionic surfactants on shear exfoliated suspensions on graphene, so we use the parameters found in the limited study of Parka [170] as a starting point.

The influence of exfoliation time on graphene platelet size, as opposed to concentration has also been the subject of limited study. TEM studies of the mean length of shear exfoliated graphene platelets in NMP [119] show a small increase with exfoliation time but it is unclear how generalisable these results are to other solvents and solvent/surfactant systems. The effect of mixing time is investigated in this chapter and data indicate that there is an initial decrease in flake size with exfoliation time with flake size then remaining constant (albeit with considerable scatter in the data). In a similar vein, there has been little consideration of temperature/viscosity on the shear exfoliation process and an initial study, reported here, indicates the importance of this parameter in determining the concentration of shear exfoliated surfactant-stabilised graphene suspensions.

3.1.1 Dependence of Suspensions on Exfoliated Time

In order to investigate the effect of exfoliation time on graphene suspensions, they were prepared at ambient temperature (30 ±2°C). The initial mixture was prepared by adding 7.5 g of Triton X-100 to 1500 ml of ultra high purity (UHP with resistivity 18 MΩ cm) water in the pre-cleaned jug of a kitchen blender with four blades (Magimix 11610). 10 ml of this solution was seperated immediately for background subtraction to be performed during later characterisation of suspensions with UV-vis absorption and Raman spectroscopies. 120 g of graphite flakes (Sigma Aldrich, item number 332461) were added to the Triton - water solution. The mixture was exfoliated in the blender at the maximum rotor speed of 15000 rpm for 10 mins, after which 250 g of suspension was removed for characterization from the volume in such a way that the ratio of ingredients remained unchanged in the remaining

FIGURE 3.1: *(a) Magimix kitchen blender used for exfoliation (b) Exfoliated samples stored in 250 g bottles after 10 min steps in exfoliation time.*

suspension. High shear mixing in a kitchen blender can introduce changes in the temperature of the mixture [122, 170], therefore to avoid excessive heating, the blending was done for intervals of 1 min of blending with 5 mins of cooling between the blending intervals. The first batch consisted of four samples, exfoliated for 10, 20, 30 and 40 min, after which another 1.25 L of suspension having same ratios was blended to produce 50, 60 and 80 min samples.

Suspensions were left for 24 hrs to settle any heavier, unexfoliated flakes, after which the top 50 ml of the suspensions were transferred to centrufuge tubes of same capacity. These were centrifuged for 99 mins at 3500 rpm to remove heavier flakes. After centrifugation heavier and thicker unexfoliated material settled at the bottom of the centrifuge tubes, leaving lighter and exfoliated material in suspension. The colour of suspensions was observed, which vary from light grey to dark grey as the concentration of graphene changes. To determine the flake size, 5 ml of each suspension was carefully transferred to a pre-cleaned quartz cuvette for Raman characterisation. Samples were also investigated by UV-vis spectroscopy to determine graphene concentration using the approach of Paton *et al* [119] and material drop cast onto clean silicon substrates (with native oxide) for SEM studies.

Typical Raman spectra of graphite flakes and a graphene suspension shear exfoliated for 80 mins are shown in figure 3.2. The Raman spectrum of the graphite flakes (which form the starting material for the suspensions) shows a visible D peak at 1346.6 cm^{-1}, G peak at 1580 cm^{-1} and 2D peak at 2735 cm^{-1}, with a shoulder at 2705 cm^{-1}. The Raman spectrum from the graphite shows I_D/I_G = 0.10, which suggests a significant defect density within the initial material. The same Raman features can be seen in the spectra from the shear exfoliated suspensions, figure 3.2(b). However, there are two distinct differences between the spectra of shear exfoliated platelets and those of the starting material – the relative intensities of D and G lines and the shape of the 2D line – each of which will be considered in turn.

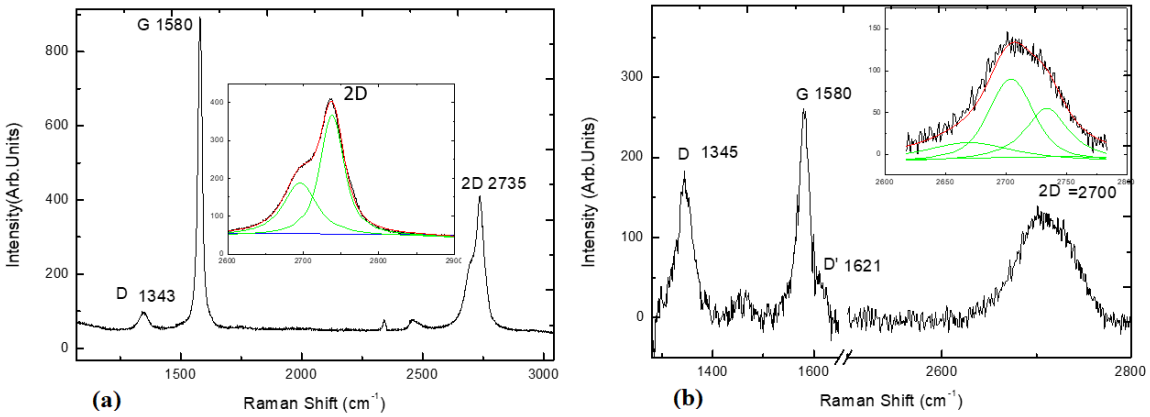

FIGURE 3.2: *(a) Raman spectrum of a graphite flake, inset is the best fit to the 2D peak; (b) Raman spectrum of a graphene suspension exfoliated for 80 mins, inset shows the best fit to the corresponding 2D peak.*

As discussed in Chapter 2, the D line in the graphene Raman spectrum is associated with defects. Hence, the ratio of the intensities of the D and G lines, I_D/I_G can be used to determine the (relative) defect density within a sample. If the density of defects is dominated by the edges of the graphite platelets it was shown, in a seminal study by Tuinstra and Koenig [153], later refined by Ferrari and co-workers [155], that it is possible to determine platelet dimensions, as discussed in Chapter 2. Using the Tuinstra and Koenig [153] relationship given by equation 2.1, the mean platelet size in the graphene suspensions was determined, as presented in table 3.1 and figure 3.3.

TABLE 3.1: Raman characterisation of exfoliated suspensions at room temperature

Raman Characterisation					
time(t) (mins)	I_D/I_G	I_{2D}/I_G	**FWHM(G) cm^{-1}**	**FWHM(2D) cm^{-1}**	**Flake size (nm)**
10	0.167 ± 0.003	0.92 ± 0.09	22.8	65.2	115 ± 2
20	0.86 ± 0.06	2.1 ± 0.2	20.18	63.92	22 ± 2
30	0.907 ± 0.004	1.40 ± 0.07	23.4	63.2	21 ± 1
40	0.60 ± 0.02	1.01 ± 0.03	27.2	58.8	32 ± 1
50	0.75 ± 0.03	1.21 ± 0.05	25.5	62.3	26 ± 1
60	0.714 ± 0.004	1.41 ± 0.05	24.4	64.7	26.9 ± 0.2
80	1.09 ± 0.03	1.28 ± 0.04	25.5	64.5	17.7 ± 0.5

The estimated platelet sizes are smaller than those previously reported for exfoliation in Triton X-100 by Parka [170], which could be related to the smaller concentration of surfactant (1 g/L) used in that work compared with the concentration used here (5 g/L). Paton *et al* [119], exfoliating in NMP, found a considerably larger platelet size but the differences in solvent and centrifuging protocol may explain this disparity. In determining the platelet size from the Tuinstra and Koenig [153] relationship, the initial I_D/I_G ratio of graphite flakes has been subtracted from the I_D/I_G ratio of the exfoliated suspensions of graphene. It is

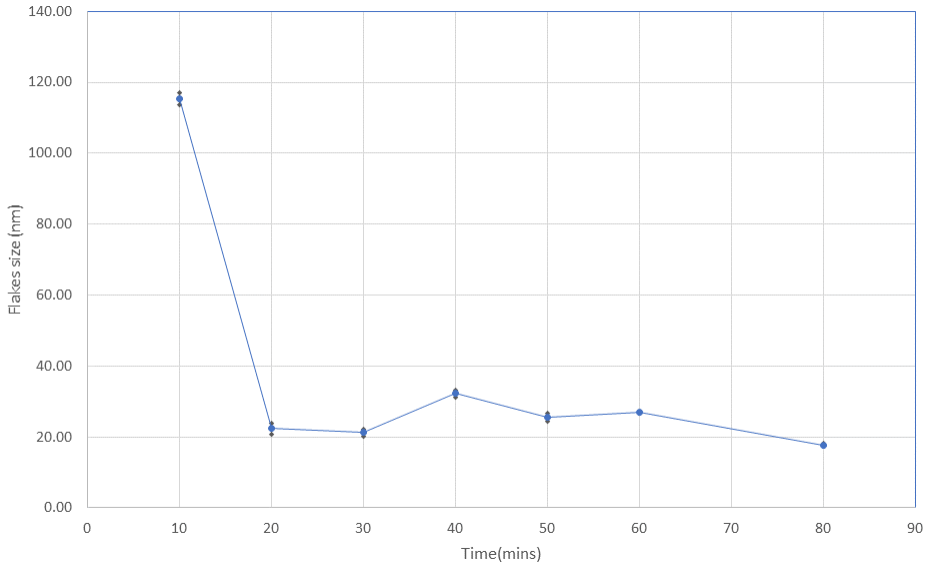

FIGURE 3.3: *Relationship between platelet dimensions and time of exfoliation.*

assumed from the work of Paton *et al* [119], that the additional defects introduced by shear exfoliation are of edge type (due to an increased number of edges in the suspended flakes). It is also possible that we have removed most of the larger platelets during centrifugation and are left with smaller size platelets having larger contribution from their edges. Figure 3.3 shows that the platelet size is largest after 10 mins of exfoliation, while it drops and the becomes nearly constant for an increase in exfoliation time to 20 - 80 mins. This might be due to less exfoliation in the first 10 mins, with most of the platelets coming from larger graphite flakes. The platelet size becomes smaller after further exfoliation as smaller flakes are disrupted.

SEM measurements were performed on platelets from selected exfoliated samples in order to confirm the conclusions drawn from Raman spectroscopy. Samples were drop-cast on Si substrates, pre-cleaned with isopropanol, acetone and UHP water and then dried under a steam of pure nitrogen to ensure the removal of all contaminants. Clear and transparent platelets, both isolated and in aggregation, could be observed, figure 3.4. From SEM analysis, it can be seen that few layer platelets are present in suspension including monolayers, and the area of most of the platelets is between 10 and 60 μm^2 (see flake size distribution chart in figure 3.4). The SEM analysis shows that the dimensions of the platelets in the suspensions are weighted towards smaller areas, which is consistent with the results obtained from Raman characterisation. The average size of platelets measured by SEM is significantly larger than that calculated from Raman analysis, which may be the result of insufficient statistics or the presence of non-edge defects in the material. The discrepancy between the two measurement techniques would repay investigation in future work.

As discussed in Chapter 2, the 2*D* line shape can provide valuable insight into the average number of layers of platelets in suspension and 2*D* lines from suspensions produced

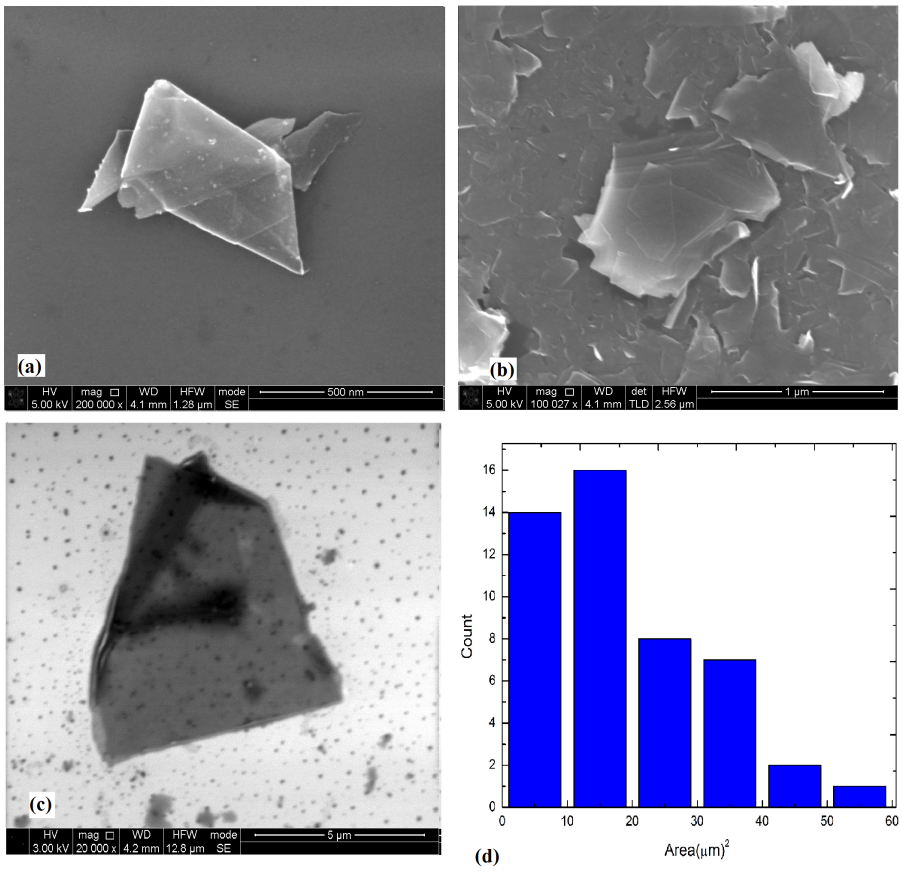

FIGURE 3.4: *(a) A folded monolayer platelet; (b) a monolayer platelet within the few layer material; (c) a bilayer platelet; (d) graphene platelet size distribution chart.*

at differing exfoliation times are shown in figure 3.5. The 2*D* peaks from all of our suspensions are best fitted with five Voigt (Gaussian-Lorentzian convolution) components. The 2*D* line shapes of our suspensions peak at around 2700 cm^{-1} and have a shoulder at the high frequency side at around 2725 cm^{-1}, similar to that suggested for trilayer graphene in Ref [147]. Therefore we conclude that these suspensions are mainly consist of trilayer platelets. Furthermore, we can rule out a significant presence of turbostratic graphite which would be fitted with single broad Lorentzian peak as discussed in chapter 2.

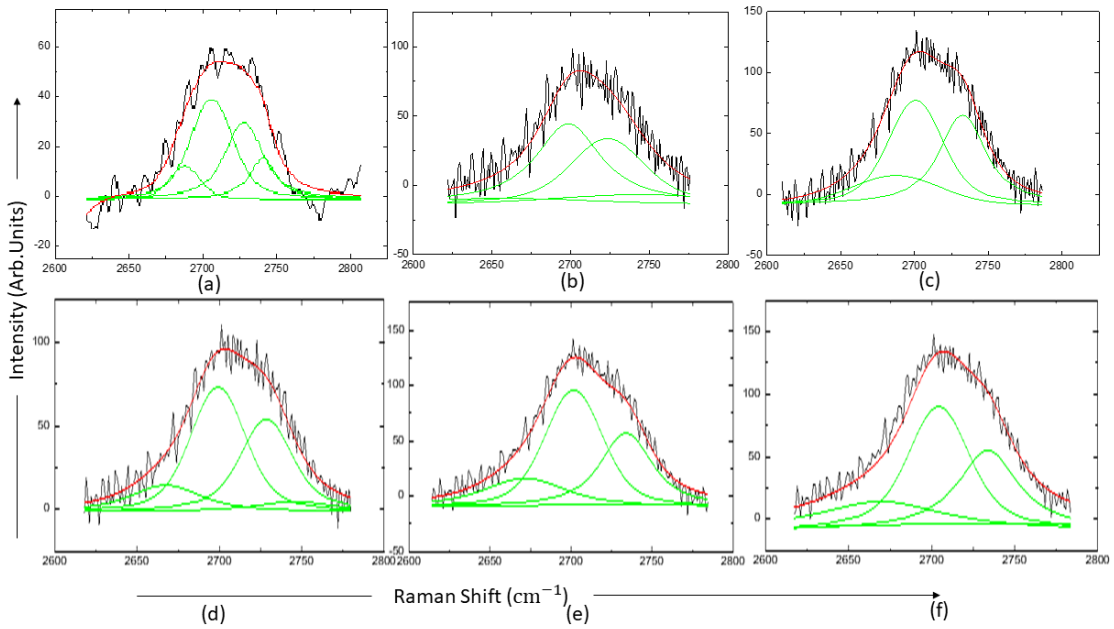

FIGURE 3.5: *Figure (a)-(f) 2D Raman lines of graphene in suspensions exfoliated for 10, 20, 40, 50, 60 and 80 mins respectively.*

The concentration of the suspensions were measured by UV-vis spectroscopy in the wavelength range 300-700 nm. For this purpose, 1 ml of centrifuged sample was diluted with 9 ml of UHP-water to prepare a 10% diluted sample before measurement in order to prevent the strong scattering which occurred from concentrated samples. The percentage transmission of light for each diluted sample was recorded at 660 nm using 10 mm glass cuvettes. (Note: the Triton-water solution was also diluted to 10% for background subtraction). Concentrations were calculated using the Lambert-Beer Law, as given by equations 2.2 and 2.3. The value of absorption coefficient α_{660} was taken as 6600 ml.mg^{-1}.m^{-1}, from Ref [121]. Figure 3.6 shows that the concentration of the suspensions increases with exfoliation time, which is consistent with the results of previous work [119, 121].

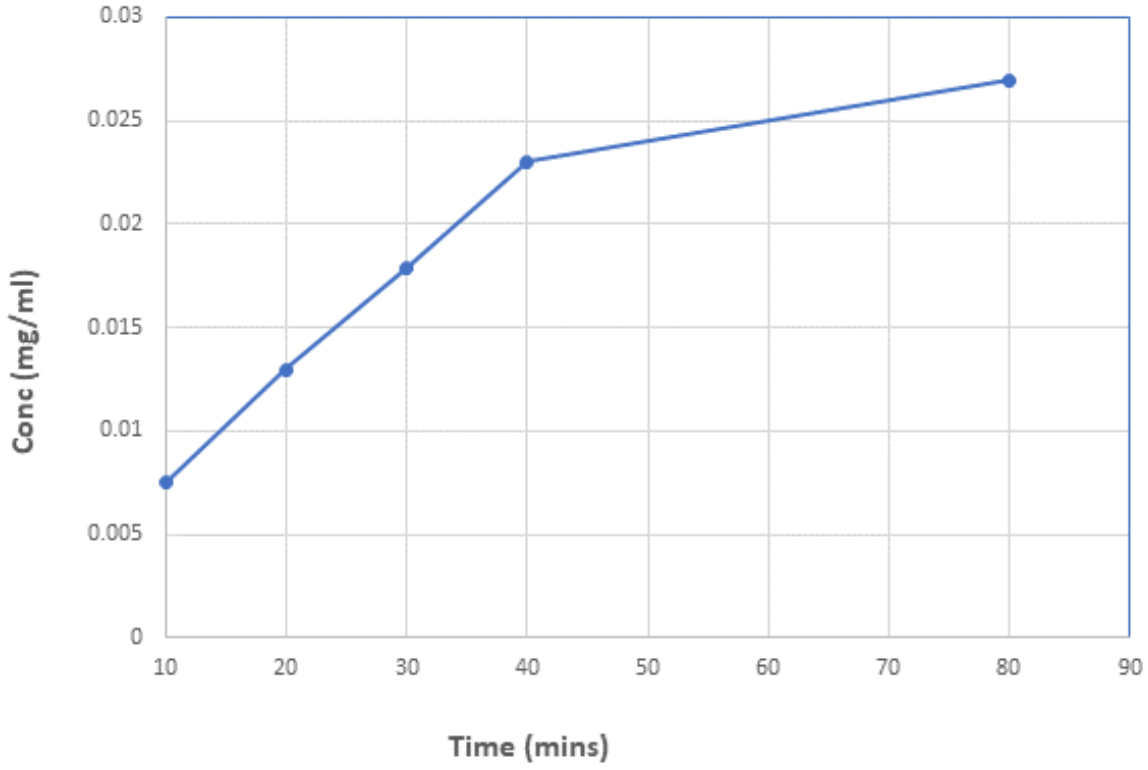

FIGURE 3.6: *Relation between concentration of suspension and time of exfoliation. The lines are a guide to the eye.*

3.1.2 Relationship between temperature, viscosity and concentration of shear exfoliated graphene suspensions

To understand the the influence of temperature and viscosity on the shear exfoliation of graphene a series of preliminary experiments were undertaken. As discussed above, there have not been any studies on the influence of viscosity on shear exfoliation, to the best of our knowledge. Since the viscosity of water is temperature dependent we examined exfoliation at 10°C and 50°C, with all other conditions constant. The temperature was recorded after each minute of exfoliation, and showed a 2°C rise in temperature after one minute of blending. An ice bath was used to keep the sample exfoliated at 10°C at a constant temperature. Similarly, to increase the temperature to 50°C a simple electric fan heater was used: This heater was placed at a distance of 30 cm from the jug and the temperature monitored. Both samples exfoliated in pure water were blended for 10-60 mins with identical parameters (i.e., one litre of UHP water , 5 g of Triton X-100 and 80 g of Graphite flake). 50 ml of suspension was removed after every 10 min of exfoliation for characterisation.

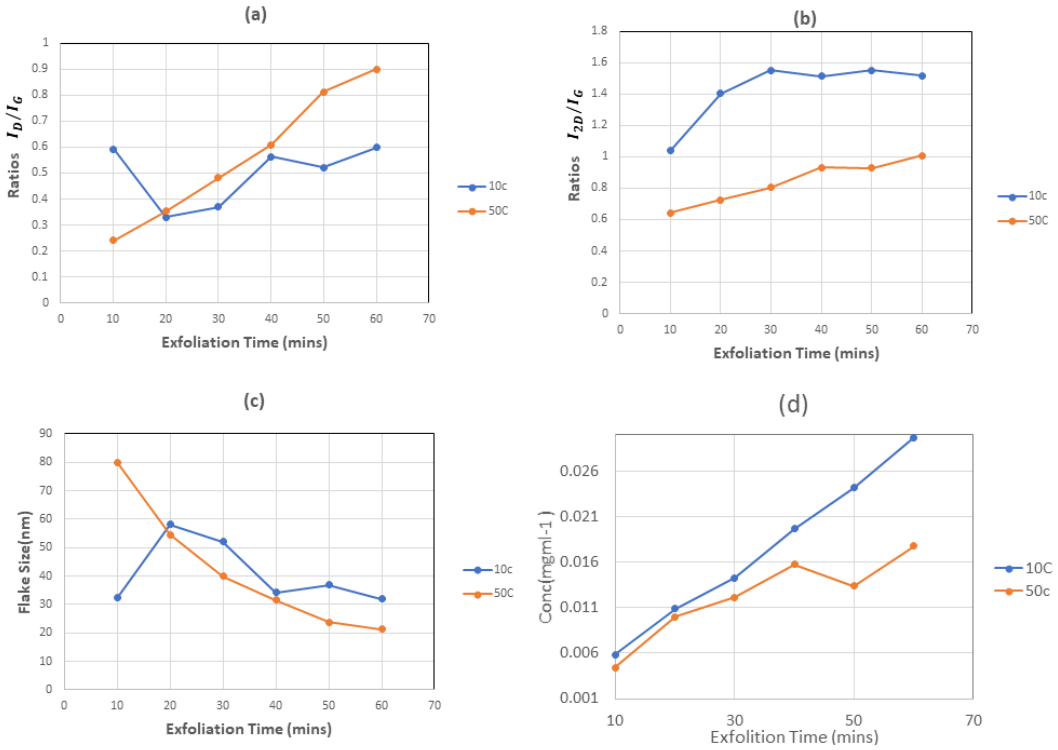

FIGURE 3.7: *(a).D/G ratios of exfoliated samples at different temperature obtained after Voigt fitting; (b) 2D/G ratio of exfoliated samples at different temperatures obtained after Voigt fitting; (c) Comparison of flake size and (d) Concentration of samples exfoliated at different temperatures. The lines are a guide to the eye.*

Figure 3.7 presents the I_{2D}/I_G, I_D/I_G ratios and concentrations for samples exfoliated in pure water at 10°C and 50°C. It is clear from figure 3.7 that at low temperature, both concentration and I_{2D}/I_G ratio is increased with respect to suspensions produced at higher temperature, while the I_D/I_G ratio is decreased. Therefore, it can be inferred that at lower temperature better quality suspensions with higher concentrations can be prepared. Hence the temperature affects both the quality and quantity of exfoliated flakes in the suspension.

TABLE 3.2: Viscosity vs concentration : All samples have been exfoliated for 20 mins.

Sample	**Temp±1 °C**	**Water (ml)**	**Glycerol (ml)**	**Viscosity (mPa.s)**	**Transmission (T) %**	**Conc (C) mg/ml**
I	10	500	0	1.3	91.42	0.0059
II	20	500	0	1.0	96.08	0.0026
III	20	250	250	6.9	98.33	0.0011
IV	20	450	50	1.2	92.54	0.0051

To determine if the effect is due to temperature or viscosity, aqueous solutions of different viscosities ranging from 1.00 - 6.90 mPa.s were prepared. In particular, a glycerol-water solution was chosen such that its viscosity at room temperature was similar to that for pure water at 10°C. UV-vis spectroscopy results obtained after centrifugation and diluting the

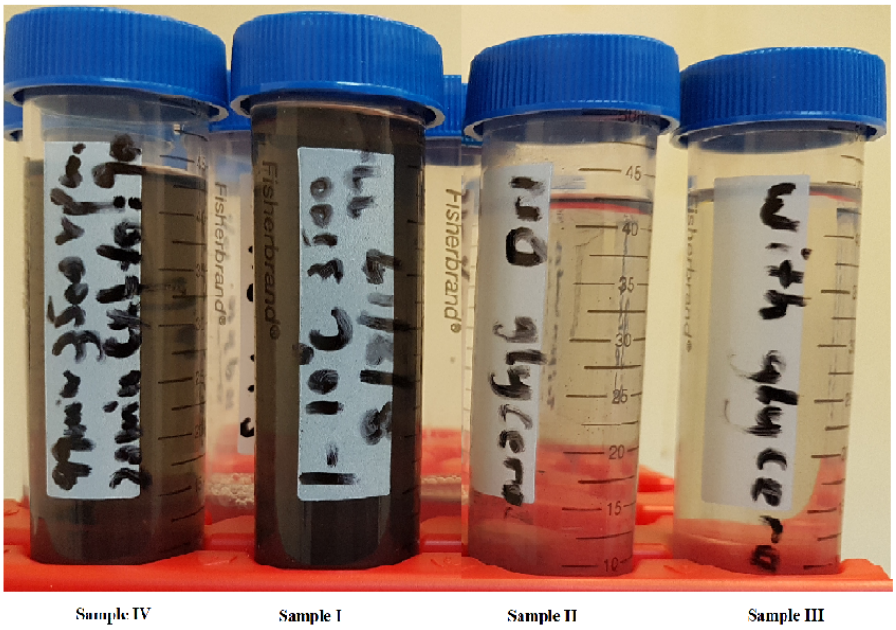

FIGURE 3.8: *Photographs of shear exfoliated graphene suspensions. Sample I and IV having nearly the same viscosity attained by different means show nearly same concentrations, while sample II is less concentrated and sample III, which is of very high viscosity shows a lower concentration still.*

samples (1:10) are given in table 3.2. From the table we can see that increasing viscosity initially leads to an increase in concentration of the suspension. The increase in concentration can be rationalised through the greater shear force that a more viscous liquid would exert upon the graphene flakes. Hence, an increase in viscosity should lead to an increase in exfoliation and therefore platelet concentration. That the variation is due to viscosity rather than temperature can be seen by the graphene concentrations obtained for pure water at 10°C and the glycerol-water concentration of similar viscosity produced at 20°C, which are in close agreement. However, at high viscosity the concentration of exfoliated material is observed to be reduced, and the origin of this phenomenon is explained below. This trend can also be determined qualitatively from the colour of the samples, as shown in figure 3.8.

The rotational speed of the blender was measured by reflecting a laser beam from a reflective tab on the blender shaft and detecting the reflected signals with a photodetector connected to an oscilloscope. This measurement showed no significant change in rotational speed (15,000 ± 100) of our kitchen blender with viscosity, leading to the conclusion that viscosity changes to this level do not change impeller speed. Table 3.3 shows the different parameters associated with the blender. To examine how the viscosity may ultimately suppress the shear exfoliation process we follow the analysis formulated by Paton *et al* [119], which is based on shear exfoliation induced by turbulent liquid motion: The Reynolds Number, Re, for a mixer, with impeller diameter d_i rotating at a rate N, with the associated flow of a fluid of density ρ and viscosity η is given by,

$$Re = \frac{\rho N d_i^2}{\eta}$$

.

Under the conditions of shear exfoliation used in our work $Re \gg 10^4$ indicating that flow is fully turbulent. Let us consider that all input power P is dissipated in turbulent eddies [119], the average shear rate in a fluid of volume V can be written as

$$\sqrt{\frac{P}{V\eta}} = \gamma.$$

In turbulent flow the power number of the mixer, N_P is constant, and is given by [171],

$$N_P = \frac{P}{\rho N^3 d_i^5},$$

therefore it can be shown [171] that

$$\gamma \propto \left(\frac{\rho}{\eta}\right)^{1/2}.$$

Using the values for the impeller diameter and rotational speed (which was found to be independent of viscosity over the range studied) and the measured power consumption of the mixer in 500 mL pure water at 25°C, $P_0 = 75$ W, we find an average shear rate $\gamma_{water} = 1.3 \times 10^4$ s^{-1}, which is a little above the threshold for shear exfoliation previously reported [119]. For a 90:10 water:glycerol mixture, $\eta = 1.2 \times 10^{-3}$ Pa s and density, $\rho = 1.03 \times 10^3$ kg m^{-3}, implying $\gamma = 1.1 \times 10^4$ s^{-1} , still around the threshold average shear rate. In a 50:50 water:glycerol mixture $\eta = 6.9 \times 10^{-3}$ Pa s and $\rho = 1.13 \times 10^3$ kg m^{-3}, hence $\gamma = 5.0 \times 10^3$ s^{-1} which is only about half the threshold shear rate required for exfoliation to occur, explaining the absence of a significant concentration of exfoliated graphene under these conditions.

TABLE 3.3: Key parameters associated with the blender.

Impeller diameter, d_i (m)	4.2×10^{-2}
Rotational speed (rpm)	15100 ± 100
Power consumption in H_2O at 25°C (W), P_0	75 ± 5
Power number, N_P	3.7×10^{-2}
Viscosity of pure water at 25°C (Pa s)	8.90×10^{-4}

3.2 Exfoliation of other 2D materials

It has been shown that 2D layered materials such as MoS_2, $MoSe_2$, WS_2 and h-BN can also be exfoliated by stablising in aqueous surfactant solution [119, 120]. Table 3.4 shows the parameter values for these TMDCs suspensions prepared in our laboratory at room temperature by Mr Angus Mathieson using the shear exfoliation approach described for graphene.

TABLE 3.4: Parameter values for exfoliation of 2D materials beyond graphene.

Material	Material weight (g)	Triton X-100 (g)	UHP water (ml)	Time (mins)
MoS_2	25	5	500	20
$MoSe_2$	5	1	100	10
WS_2	12.5	2.5	250	20
h-BN	12.5	2.5	250	20

Raman spectra for TMDCs were taken for bulk samples and exfoliated suspensions as shown in figure 3.9. The Raman spectra for the exfoliated material was taken after separation of unexfoliated and thicker flakes by centrifugation at 3500 rpm for 99 mins. The top 50% of the suspension from the centrifuge tube was transferred to a cleaned cuvette for characterisation. Figure 3.9(a) shows the Raman spectra of the bulk and exfoliated MoS_2. The increase in the frequency and intensity of E^1_{2g} Raman mode of the exfoliated material clearly show that exfoliation has occurred and few layer platelets are present in suspension [158–160]. Furthermore, the separation between the peaks A_{1g} and E^1_{2g} is also changes from 25 cm^{-1} to 22 cm^{-1} in going from the bulk to the exfoliated material. These results are in agreement with the already reported literature [158–160]. However, the positions of the peaks are slightly blue-shifted by ~3 cm^{-1} in our spectra and this shift is constant in the Raman spectrum of all of these samples. This could be the effect of aqueous surfactant solution, as the values reported in the literature [158] are derived from mechanical exfoliation.

Figure 3.9(b) shows the Raman spectra of exfoliated and bulk $MoSe_2$. An increase in the intensity of A_{1g} Raman mode indicates the presense of few layer flakes. A redshift in frequency is also evident for the A_{1g} Raman line, from 245.3 to 241.9 cm^{-1} which has previously observed between bulk and exfoliated material [161]. Likewise, the Raman spectra of bulk and exfoliated WS_2 reflects the change in intensity of E^1_{2g} Raman mode, figure 3.9(c). The high intensity of the E^1_{2g} mode in the exfoliated sample is an indication of the presense of few layer platelets in the suspension and is once more in agreement with the literature [162]. Hence, the Raman data show that surfactant stabilised suspensions of all these materials, suitable for thin film and heterostructure deposition as described in Chapter 4, can be produced by our shear exfoliation approach.

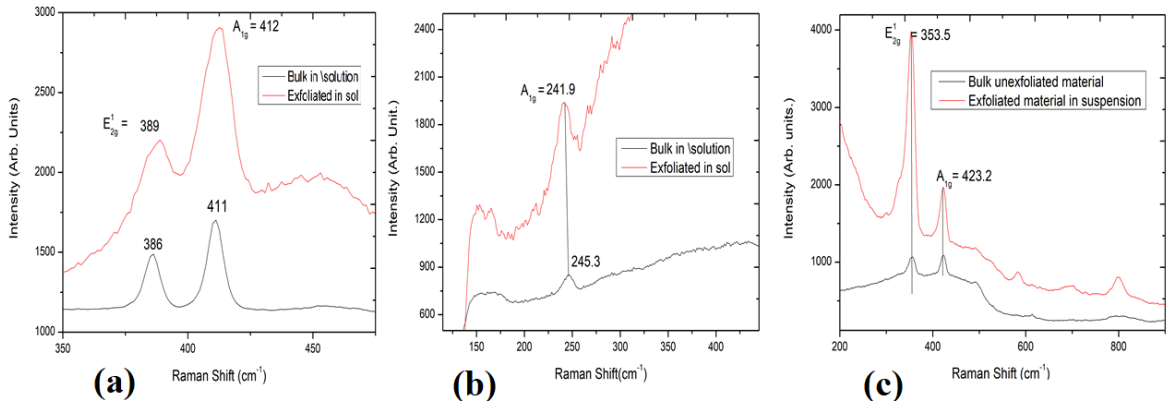

FIGURE 3.9: *Raman spectra of exfoliated and bulk materials of (a) MoS_2, (b) $MoSe_2$ and (c) WS_2.*

3.3 Conclusion

It can be concluded that shear exfoliation under the conditions used in this work can produce aqueous surfactant-stabilised suspensions of a broad range of 2DLMs. In the case of graphene, Raman spectroscopy indicates that the suspensions are dominated by trilayer material. The principal effect of increased exfoliation time is to increase the concentration of the suspensions and, although the concentration increases monotonically, there is evidence that the rate of increase with exfoliation time may saturate in the limit of very long timescales, which is worthy of further investigation. Platelet lateral dimensions, determined from Raman spectroscopy and supported by the results of SEM measurements, initially decrease and then saturate. The plate sizes are relatively small and for optimal use in thin film preparation work to increase platelet size would be valuable. It is shown that the concentration of shear exfoliated graphene is strongly influenced by the viscosity of the liquid used. In the case of water, the viscosity was controlled either by temperature or through the introduction of glycerol. An initial increase in concentration was observed with increasing viscosity, however, if the viscosity increased to the extent that the minimum shear rate could not be exceeded in the turbulent flow generated by the mixer impeller blades, exfoliation was suppressed. Hence, it is predicted that there is an optimum viscosity to maximise the concentration of shear exfoliated 2DLMs.

Chapter 4

Deposition of Thin Films and Heterostructures of 2DLMs

4.1 Introduction

As described in Chapter 1, there are many potential applications accessible for thin films and vdWHs of 2DLMs, especially if the production process is scalable, generic and uses easily produced precursors. For this purpose, two different approaches to film and heterostructure deposition were examined: Langmuir-Blodgett (LB) deposition and a new technique developed by us, termed "Liquid Interface Deposition" (LID) and described in Chapter 1. A patent has been applied for in respect of LID. Here we shall discuss the preparation of films by both of these techniques.

Before the deposition of the films suitable substrates were prepared. For LB deposition such preparation is a necessity, whereas work reported by Mathieson [122] has shown that minimal substrate cleaning is required for LID. Glass substrates were usually used for deposition of films as it is a transparent substrate and hence helpful in measurement of film thickness through transmission of light. However, glass is not suitable as substrate for use in SEM characterisation because of charging arising from its insulating nature. Therefore, samples for SEM characterisation were prepared on silicon (with native oxide) and copper substrates. The oxide layers on copper and silicon give better optical contrast hence improves the visibility of graphene on the substrate. Cleaning was performed to remove residues and makes the surface smoother for deposition, as untreated surfaces could alter the films by introducing ripples and wrinkles. Glass substrates were cleaned rigorously, first by detergent and water to degrease the surface of the slide. Slides were then rubbed by 'Kimwipes' soaked in dichloromethane (DCM). Next, the slides were sonicated in each of the following: DCM, isopropanol, UHP water, isopropanol again, each for 15 minutes. The slides were dried by a stream of pure nitrogen gas and then left in a solution of 2 g/L NaOH solution for 24 hours. This was done to render the glass slide hydrophilic which aids

the deposition of film on the surface in the LB process. Before depositing the film on the glass slide it was once again rinsed with UHP water and dried in a nitrogen gas stream. The surface of Si was cleaned by acetone, isopropanol and UHP-water, then etched in a Gatan Plasma cleaner for 10 mins in the mixture of Ar - O_2, followed exposing silicon wafer to native oxygen which introduced an oxide layer on the silicon. The surface of the Cu substrates were cleaned by sonicating in acetone and then isopropanol each for ten minutes, followed by a dip in acetic acid for 30 sec and washing with UHP water and finally driying with pure nitrogen. Acetic acid etches the copper surface by removing the oxides, furthermore, leaves the surface hydrophobic in nature.

4.1.1 Langmiur Blodgett Deposition

In LB deposition the substance which is to be deposited must be suspended in a solvent having a low boiling point and which is insoluble in water, which allows it to evaporate at room temperature from the water surface. The amphiphilic nature of graphene sheets [172] makes them suitable for depositing from the surface of the water, on to hydrophilic or hydrophobic substrates. Graphene can be directly be exfoliated in solvents such as NMP but these are not suitable for LB deposition because of the high boiling point of this solvent. Therefore, the graphene was exfoliated in a surfactant, which was then removed before resuspending the graphene in suitable organic solvent such as dichloromethane (DCM). The surfactant was removed by centrifuging the pre-prepared suspensions at 8500 rpm for 30 mins. This draws the nearly all of the exfoliated material to the bottom of the centrifuge tube leaving aqueous surfactant solution as the supernatant which is removed and discarded. The thick black material precipitated at the bottom of the centrifuge tube is re-dispersed in UHP water by sonication. The re-suspended material is again centrifuged to remove more surfactant and the process is repeated three times to remove the maximum quantity of surfactant possible. After the last washing step the precipitate is re-suspended in DCM (rather than water) by sonicating for 15-30 mins.

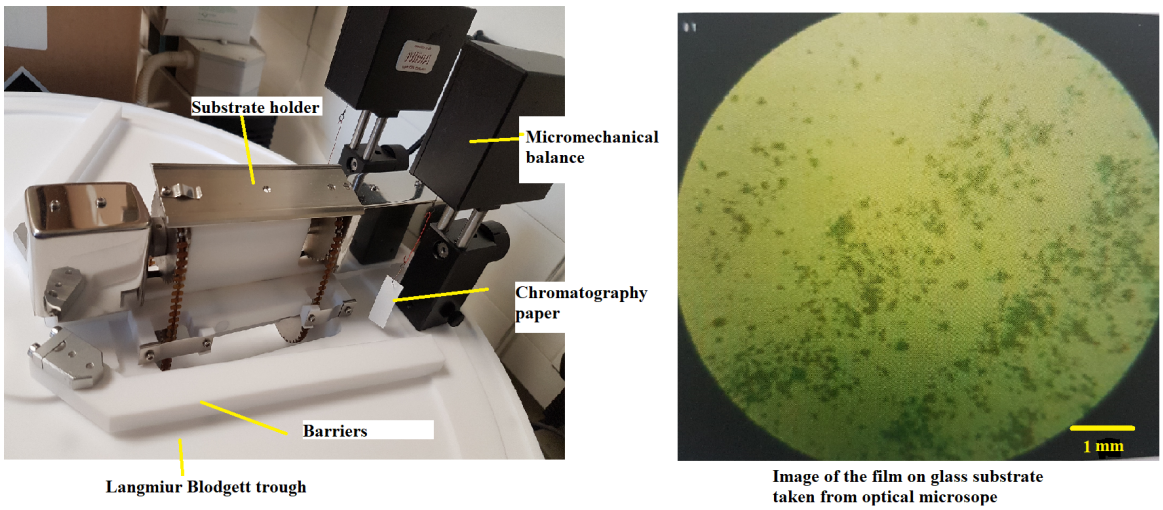

FIGURE 4.1: *Langmuir-Blodgett assembly used for deposition of graphene on glass slides.*

The Langmuir-Blodgett trough (fig 4.1) wasthoroughly cleaned for the deposition of thin films. The Nima technology trough was dis-assembled and the individual components cleaned first using iso-propanol and then UHP water with special purpose 'Kimwipes'. Nitrile gloves and clean-room clothing were worn throughout the deposition process to stop the introduction of unwanted particulates onto the surface of the water. After cleaning, the trough was re-assembled and filled with UHP water in such a way that the meniscus can be seen just over the level of the trough edge. The barriers were swept over the surface to check the surface pressure which was measured using Wilhelmy plates consisting of chromatography paper hanging on a very sensitive electronic micro balance and dipped into the surface of the water. The surface of the water was further cleaned to remove any remaining particles using an adapted vacuum pump, until the change in surface pressure upon closing the barriers became less than ± 0.1 m Nm^{-1}.

The DCM and graphene dispersion was slowly deposited evenly across the surface of the water using a micro-syringe. The trough was then left for 15 minutes to allow the DCM to evaporate from the surface, leaving only the graphene. The barriers were swept over the surface of water with a speed of 100 cm^2 min^{-1} to slowly compress the layer of graphene. Li *et al* [172] has reported a surface pressure of 27 mN m^{-1} to produce a dense film of graphene. However, we were only able to produce a maximum surface pressure of 19 mN m^{-1} before the Wilhelmy plate was pushed out of the sub-phase causing spillage and damaging the film. A pre-cleaned hydrophilic glass slide was placed under the water surface and brought up through the film once the maximum pressure in the solid film was achieved. A constant surface pressure of 19 mN m^{-1} was then maintained by pressure control function of the trough throughout the dipping procedure. The substrate was lifted vertically at a speed of 5 mm / min through the surface film which was then slowly deposited on glass slide. As more material was added the surface pressure eventually dropped below 19 mN m^{-1}. The desired number of layers can be achieved by setting the number of passes of the substrate through the surface and in this way 8 -10 layers of graphene platelets were deposited. Although graphene films could be deposited (figure 4.1), they were of low quality showing voids, non-uniformity and aggregation, which could not be eliminated by varying the parameters at our disposal. There were a number of reasons for the difficulties encountered in successful LB film deposition:

1. By removing all the surfactant, graphene flakes quickly re-aggregated making graphite-like particles which could not be dispersed in DCM even after sonicating for one hour. Some aggregates remained in suspension leading to non-uniformity in deposition.

2. Deposition is only possible if done shortly after dispersing in DCM because re-aggregation occurs quickly and reduces the control over concentrations.

3. It is necessary to remove the surfactant from the platelets before deposition for following reasons. First, if surfactant remained on the platelets, it increases the mass of platelets which sink in water instead floating on surface, preventing the formation of a continuous film on the water surface. Secondly, the presence of surfactant would

perturb the film properties. Third, the surfactant may prevent successful vdWH layer production due to its size and electrostatic properties.

4. The process is highly sensitive, as any slight disturbance or change in air pressure leads to a change in formation of the 2D film on water, resulting in the flakes sliding over each other and the film collapsing and sinking into the water after becoming heavier.

Langmuir-Blodgett deposition was also attempted for MoS_2 but was unsuccessful since it was not possible to suspend the MoS_2 in DCM. These difficulties, coupled with the lack of flexibility in substrate choice led to the development of a new deposition approach - LID.

4.1.2 Liquid Interface Dipping

As outlined in Chapter 1 **Liquid Interface Deposition** is a new technique which involves the assembly of a continuous film of platelets of 2DLM at the interface of a surfactant stabilised suspension and a carefully chosen 'seperation solvent'. The suspensions described in 3.1 are used as starting material for deposition of thin films. Some of the unique features of this method are given below:

1. The removal of surfactant from exfoliated platelets and the creation of the thin film is acheived simultaneously.

2. A continuous thin film is formed at the interface of two immiscible liquids, having a lateral extent only dependent on the amount of material used and the diameter of the centrifuge tube.

3. The number of layers can easily be controlled through the concentration of the suspension, although other ways have also been proposed – such as choice of 'separation solvent' – but are beyond the scope of this report.

4. The technique is generalisable to the whole range of layered materials from conductor to insulator, as is reported here.

5. The films obtained in this way can be deposited on wide range of substrates both hydrophobic and hydrophilic. Deposition on Si, Cu, glass and aluminium is reported in this work.

6. This is an environmentally friendly technique, as the surfactant and solvent are separated during centrifugation, and can be re-used atleast once without any further treatment and many times after purification by fractional distillation.

7. The method is cost effective, compared with CVD or MBE etc, as only simple equipment consuming little energy are required.

8. The method provides the solution for scalable production of thin films.

9. The method is highly suitable for creation of the heterostructures, as different films can be stacked on top of each other, in the manner proposed in Ref [31].

4.1.2.1 Liquid Interface Deposition of Graphene Films

In order to produce thin films of graphene, suspensions of surfactant stabilised few-layer platelets with predominantly <5 layers were prepared as described in Chapter 3. For thin film assembly, 2.5 ml of suspension was added to a centrifuge tube containing 10 ml of DCM using a syringe, which starts floating in the form of a large spherical "blob" at the surface of the DCM because the two liquids are immiscible. The centrifuge tube was shaken well, which turns the colour of the water blob from translucent to milky white, with a hint of grey indicating the presence of graphene platelets. This mixture was subsequentlly centrifuged for 25 mins at 10500 rpm stripping the surfactant molecules from the platelets, as described in Chapter 1 leaving a film of assembled platelets at the interface between the water and DCM. Thicker films can easily be seen without any optical aid around the blob of water sitting on the top of the DCM. A schematic illustration of the current understanding of the process of assembly of the thin films at the liquid interface is depicted in figure 1.9.

The stable film at the interface of liquids can readily deposited to any suitable substrate. In this work we use an approach which we term the inverse dipping technique. It is named "inverse" in that sense that it requires a substrate to move from the top, which upon lowering into water attracts the film towards it, where the film attaches to the substrate, while in Langmuir - Blodgett deposition, a hydrophilic substrate is brought from underneath the water-air interface. Other approaches have been developed by Mathieson [122] in order to transfer the interfacial films on to solid substrates and, whilst promising, these may not offer the control of inverse dipping, although they may offer greater flexibility in choice of substrate. An example of a modified form of the pouring technique adopted by Mathieson for deposition is given in appendix B of this report.

In order to deposit films by inverse dipping, a cleaned and hydrophillic glass microscope slide is slid into the centrifuge tube containing the film, whlie the tube is kept at angle of around 45°. Tilting provides more room to slide the substrate without touching the film, and if the substrate is slid vertically it goes through the middle, breaking the film, which is then sticks to both sides. If substrate is at lower angle to the interface the water is kept underneath the substrate and the film coats the lower side. Once the substrate is inserted the tube can be brought back to a vertical orientation gently and the substrate is moved steadly into the DCM . Only 10 ml of DCM was used while centrifuging, which does not give much space to fully dip the glass slide. Therefore, to completely recover the film from the water more DCM was be added to the tube at this stage, which lifts the film and water upwards. The DCM can be added until all the film is attached to glass substrate leaving the water on the top of DCM. The water is removed with a syringe before bringing the substrate out of the centrifuge tube. Once all the water is removed the substrate can be lifted out and dried. On evaporation of DCM we are left with a thicker fluid consisting of Triton-X100, entrapped water and excess flakes of graphene. DCM can be transferred to round flask, where after distillation pure DCM can be produced for re-use. A schematic illustration of the whole inverse dipping process is presented in figure 4.2.

Graphene films were deposited on silicon by repeating the procedure mentioned for

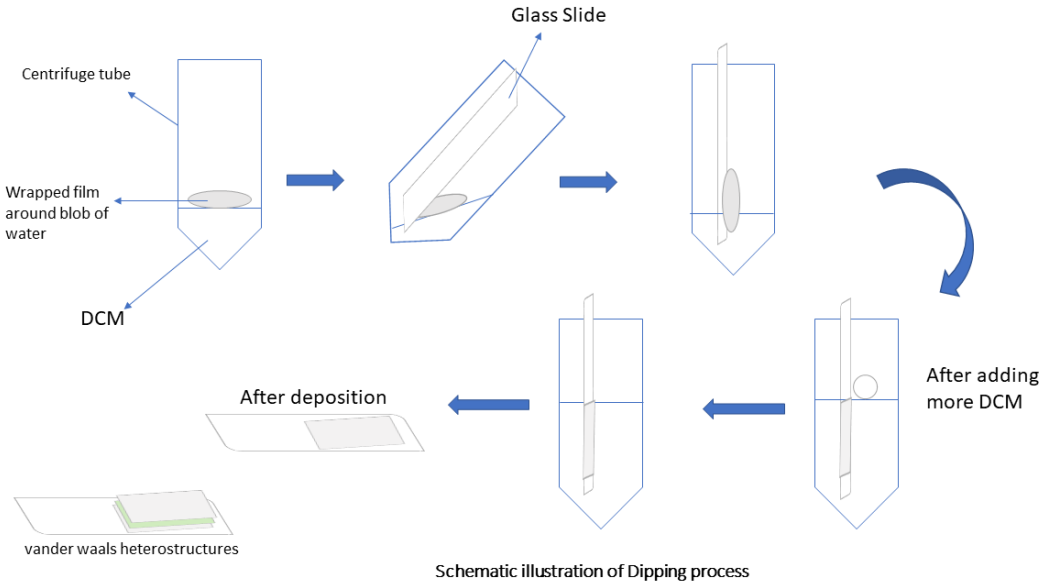

FIGURE 4.2: *Different stages of the dipping process*

the glass substrate above. While for deposition on copper and aluminium foil the pouring method described in appendix B was adapted (as we explored different techniques of film deposition from liquid-liquid interface, suitable according to size and type of substrate, and found that deposition on smaller sizes and hydrophobic substrates such as Cu could be acheived better by pouring rather than inverse dipping and more work is required such as substrate preparation prior to deposition, to improve deposition by inverse dipping on hydrophobic substrates). We used suspensions which contained a broad range of platelet thickness to verify our assumptions regarding buoyancy discussed in Chapter 1 and to simplify the deposition process. Suspensions were diluted by pre-determined ratios to control film thickness before being used for deposition. For deposition on glass slides, film thickness was determined through the transmission of light, figure 4.5(b).

The presence and nature of the films produced by inverse dipping and pouring were checked by Raman spectroscopy and SEM. Raman spectra of typical films deposited on different substrates are shown in figure 4.3(a). It is clearly seen that no peaks due to water or Triton X-100 are present, which indicates that pure graphene flakes have been deposited on the susbstrates. The similarity between the lineshapes and relative intensities of the graphene spectra from films on Al, Cu and Si with those from the suspensions indicates that no further defects are introduced during deposition. The smaller I_D/I_G ratio for films deposited on glass suggest that the hydrophhilic surface may attract larger and/or less defective platelets, which would benefit from further study. The table 4.1 reports the results of Raman analysis of the films deposited on different substrates.

Further analysis of the Raman spectra shows that the deposited films mainly consist of trilayer flakes, figure 4.3(b). The 2*D* lines of films are best fitted by five Voigt lines indicating trilayer flakes[156]. The shift in frequency of the 2*D* peak from 2735 cm^{-1} for graphite to 2704

TABLE 4.1: Raman peak positions for graphene suspension and films on different substrates and suspension

Substrate	D	G	G′	2D	I_D/I_G	I_{2D}/I_G	FWHM(G)	FWHM(2D)
Suspension	1347.2	1583.2	Not visible	2704.6	0.94	1.24	26	62.5
Glass	1345.7	1582	1621.1	2702.1	0.38	1.74	23.8	67.2
Copper	1345	1581	1622.8	2704.6	0.89	1.68	23.14	68.2
Silver	1345	1581	1619.4	2701.7	0.96	1.51	23.37	68.3
Silicon	1345	1582	1625	2701.7	0.76	1.79	22.8	63.2

cm^{-1} in bilayer or trilayer flakes also indicate the number of layers in flakes. For a monolayer this line should be below 2700 cm^{-1} with a sharp profile, which could be fitted by a single Lorentzian peak.

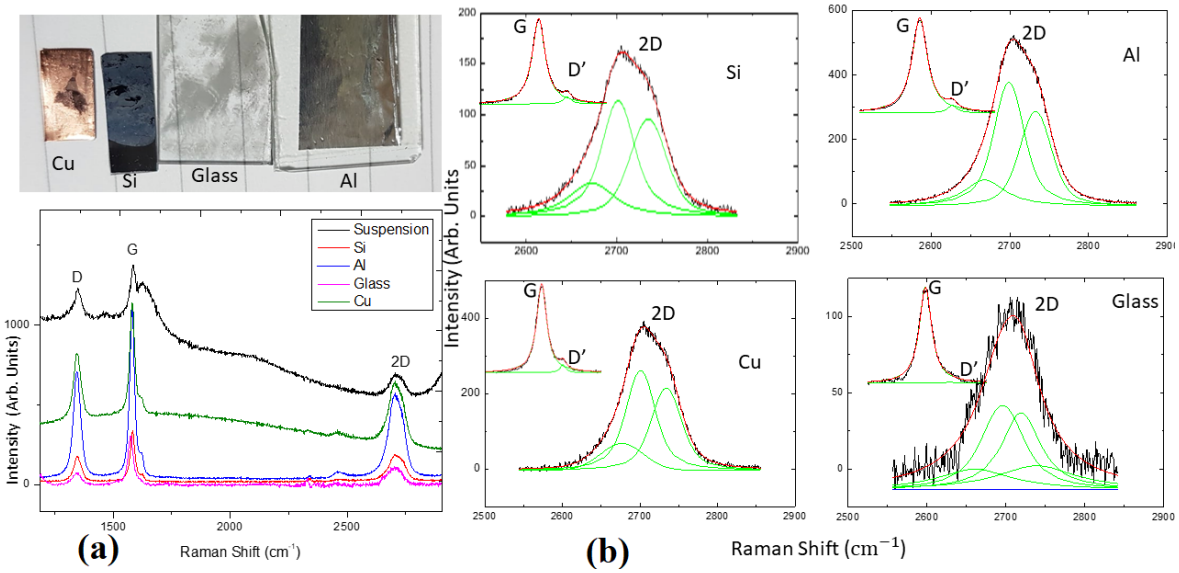

FIGURE 4.3: *a) Raman spectra of graphene films on different substrates; b) Comparison of 2D line profiles fitted with Voigt peaks on different substrates (inset shows the G and D′ bands of the corresponding films).*

Figure 4.4 shows the morphology of films of graphene on silicon. From figure 4.4 (a) and (b) it can be seen that films with lateral sizes up to few mm can be deposited by using liquid interface deposition without further optimisation. Figure 4.4 (c) - (f) are taken at different magnifications and it is evident from these images that deposited films are well connected with minimal gaps between the flakes. Furthermore the flakes are seen to overlap at the edges suggesting that they will be highly conductive. Breaks in the film seen in figure 4.4 (a) and (b) are believed to have occured while handling or shaking of tubes during the dipping process, and further optimisation of the inverse dipping process should substantially increase the continuous area of the films. Attempts were made to characterise films deposited on glass with SEM but these were not successful due to charging. The films produced by LID are significantly larger than those prepared by Langmuir-Blodgett deposition,

indicating the superiority of this approach.

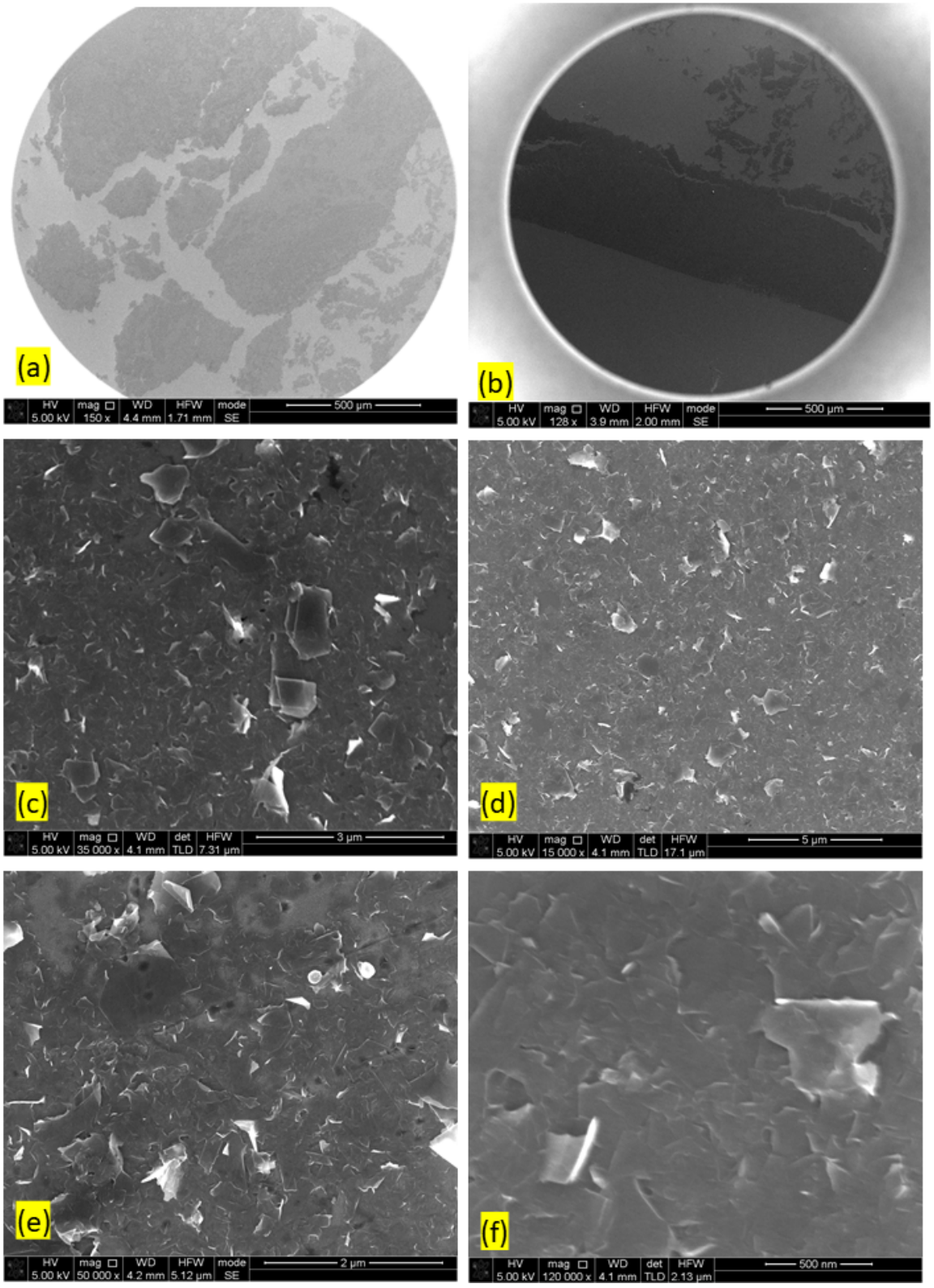

FIGURE 4.4: *SEM images of graphene films on silicon.*

4.1.2.2 Thickness control of liquid interface deposited graphene films

One means of controlling the thickness of films deposited by LID is through control of the amount of material allowed to deposit on the glass surface. We used top 50 % of 99 mins centrifuged and 80 mins exfoliated sample for deposition of these films. The figure 4.5(b) shows thin films in which thickness has been decreased by simply reducing the concentration of the suspension through adding UHP water by the ratios shown in table 4.2. From UV-vis spectroscopy, specifically the transmission through the film, one can measure the number of layers present on the surface of the glass slide. Before measuring the UV-vis spectrum two cleaned glass slides were placed in the spectrometer to get background data, which is stored internally and subtracted automatically from the spectrum of glass slides with material deposited on them. Five different spots were selected on each slide for the transmission of light in order to determine the average number of layers. As described in Chapter 1, a single layer of graphene absorbs 2.3% of light which is very useful to determine the number of layers. As we measured the percentage transmittance it was converted into percentage absorbance (100 - T%) to get values of the average number of layers in each sample. From table 4.2 it can be seen that the average number of graphene layers in the film decreases with decreasing concentration. The smallest number of layers corresponds to a single layer of the trilayer flakes present in the initial suspension. If suspensions of a single monolayer can be produced, this suggests that large area monolayer films may be deposited.

TABLE 4.2: Estimated number of layers in graphene thin films determined by optical transmission.

Suspension%	UHP-water %	Transmission T%	Number of layers(N)
100	0	65 ± 3	14 - 16
75	25	75 ±6	8 - 13
50	50	81 ±2	7 - 9
25	75	88 ± 1	4 - 6
10	90	91 ±2	3 - 5
5	95	96 ± 1	1 - 3

The Raman spectrum of all of the films mentioned above after background subtraction is given in figure 4.5 (a). The Raman spectrum of clean glass slide was taken and subtracted from the spectrum of films as the feature of glass slide is present around the 2D peak of the deposited films. This need to be get rid off before estimating the intensity and line shape of 2D peak. The peaks are integrated by fitting lorentzian peaks to estimate I_D/I_G and I_{2D}/I_G ratios, and the results obtained are also shown in table 4.3. The 2D peak is also zoomed and shown in inset of the Raman spectrum of corresponding thickness for viewing the actual shape and fitted with 5 components of viogt fit, the line shape of which shows the presence of trilayer material on glass slide. Here, we can see that I_D/I_G ratios are lower than those shown in table 3.1 for suspensions, this is due to the more continuous nature of the film resulting from reduction in edge defects due to overlapping of flakes. The I_{2D}/I_G ratio for the thickest film is the lowest as expected, while this is higher for thinner films deposited

from 90% and 95% diluted samples, which is also another indicator of the presence of few layers as predicted by UV-vis spectrometery. The flakes size in films is 37.67 ± 5.8 nm, which is nearly double the flakes size (17.65 nm) in the 80 min exfoliated suspension and consistent with the size reported by Bart [170].

TABLE 4.3: Raman analysis of different thickness of films deposited on glass by dilution

Suspension%	**UHP-water %**	$\mathbf{I_D/I_G}$	$\mathbf{I_{2D}/I_G}$	**Flakes size (nm)**	**FWHM(2D)** (cm^{-1})
100	0	0.46	1.38	41.79	66.0
75	25	0.50	1.54	38.44	63.7
50	50	0.60	2.13	32.04	60.8
25	75	0.56	1.88	34.33	65
10	90	0.41	2.11	46.88	59.0
5	95	0.59	1.97	32.58	63.2

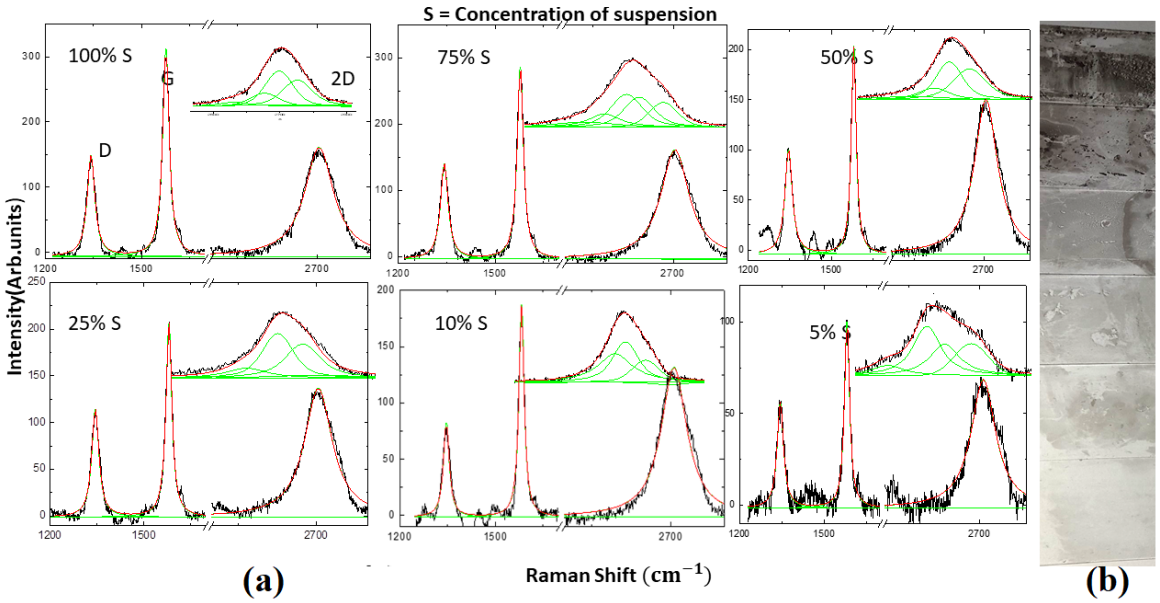

FIGURE 4.5: *(a) Raman spectra from different thickness of graphene films deposited on glass. Insets are the corresponding 2D peaks; (b) Photographs of the films on glass slides showing the decrease in thickness with dilution (increasing dilution from top to bottom).*

4.1.3 The deposition of other 2DLMs by liquid interface deposition

Figure 4.6 shows the step by step deposition of films of other 2DLMs by the approach described above, demonstrating the generalisability of our deposition technique. As we have shown in the previous section, control of thickness is possible by simply diluting the suspensions and it is not necessary to use surfactant free precursor material.

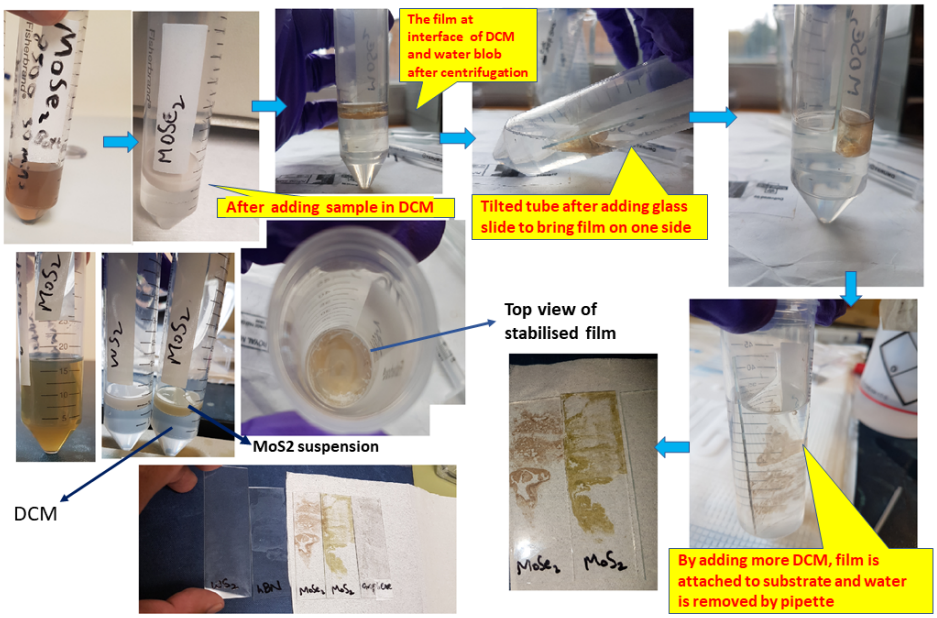

FIGURE 4.6: *From suspension to deposition step by step.*

The Raman and absorption spectra of thin films of TMDCs were measured and are shown in figure 4.7. The Raman spectrum of WS_2 (4.7(a)) shows that the difference between the E^1_{2g} and A_{1g} peaks is reduced to 68.9 cm^{-1} and 67.8 cm^{-1} for the films deposited on glass and silver substrates respectively, while that difference in the positions of those modes in the bulk material is 70 cm^{-1}. Moreover, the intensity of the E^1_{2g} Raman mode compared to the A_{1g} peak is substrantially larger in the films and exfoliated suspension in comparison with bulk flakes. The Raman data from the both exfoliated suspension and the as-deposited films indicates the presence of bilayer platelets of WS_2 [162].

The Raman spectrum of a $MoSe_2$ (4.7(b)) film shows the Raman-active A_{1g} band at 243.5 cm^{-1} and E^1_{2g} band at 289 cm^{-1}, a difference of 45.5 cm^{-1} between the two modes. The difference between A_{1g} and E^1_{2g} for bulk $MoSe_2$ is 44 cm^{-1} [173]. The increase in splitting of A_{1g} and E^1_{2g} modes indicates the presence of few layer nanosheets deposited on the glass slides. This behaviour is different in $MoSe_2$ as compared with MoS_2 where a decrease in the splitting between two modes is an indicator of decreasing thickness or number of layers [95]. Similarly, the position of E^1_{2g} Raman mode measured for the bulk $MoSe_2$ is 245.3 cm^{-1}, and for the film it is 243.5 cm^{-1}. The ~2 cm^{-1} redshift in frequency of the E^1_{2g} mode is another indicator of the presence of platelets having ≤3 layers [161]. The change in colour from the blackish grey of the bulk to light brown in the film is an additional indication of the presence of few layer platelets. The shiny brown colour is due to the transition from an indirect band gap to a direct band gap material, as described in section 2.2.1 Chapter2. This effect is reflected in the UV-vis absorption spectrum of the deposited film, which shows direct band gap transition for exciton A at 807 nm and B at 708 nm as shown in figure 4.7 [174] . This corresponds to the presence of trilayer material on the glass slide, as expected from the concentrated dispersion used to deposit the film.

The Raman spectrum of a MoS_2 (4.7 (c)) film deposited on glass is shown by the blue line in figure 4.7, which is compared with the bulk and shear exfoliated suspensions (black and red lines). The Raman spectrum of the deposited film on glass shows a decrease in the difference of frequencies between the A_{1g} and E^1_{2g} Raman modes from 25 cm^{-1} to 23 cm^{-1}, which once more indicates the presence of trilayer flakes [159]. The UV-vis absorption spectrum of MoS_2 (4.7 (d)) shows direct exitonic transitions A1 and B1, at 670 nm (1.9 eV) and 610 nm (2.1 eV) respectively, as shown in figure 4.7. The absorption arises from the transition from indirect band gap (1.29 eV) to direct bandgap material as one progressively decreases the number of layers from the bulk, and provides evidence for the presence of atomically thin material deposited on the glass surface. The presence of the B exitonic peak indicates the presence bilayer or trilayer material, as it is absent in monolayers or for material thicker than three layers [85, 86]. This direct bandgap transition is also responsible for PL and this effect can be seen by the naked eye as a bright yellowish-green colour (see colour of exfoliated sample in fig 4.6) as the films get thinner[122].

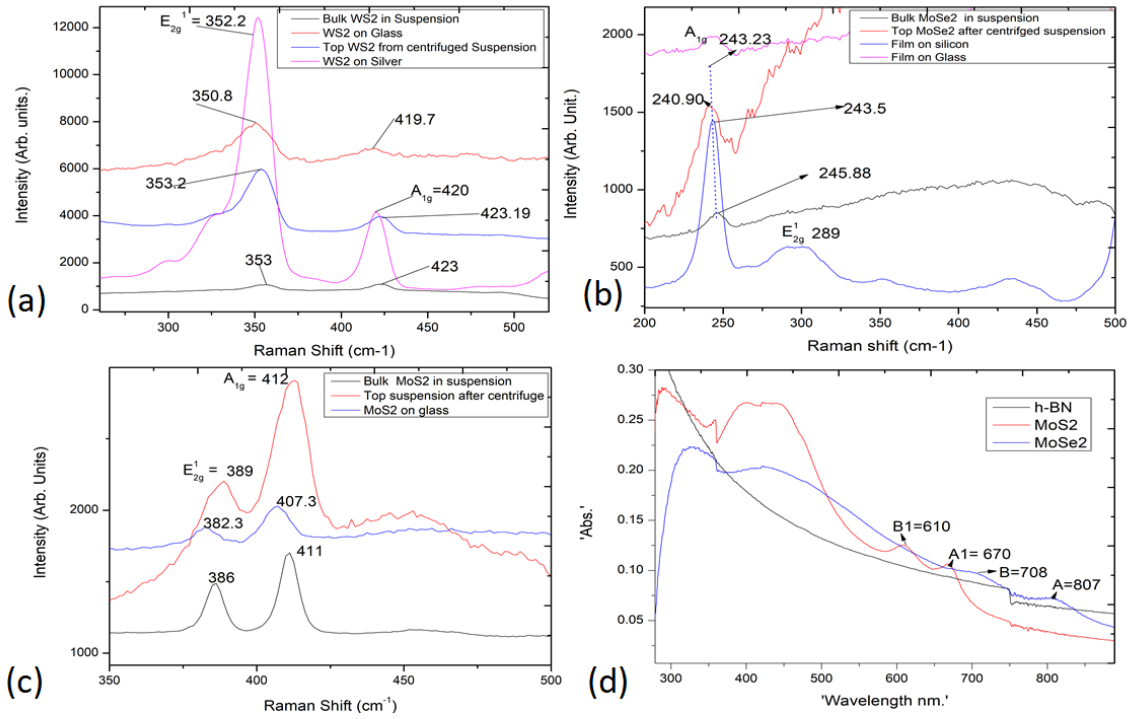

FIGURE 4.7: *Raman and Absorption spectra of thin films of TMDCs*

4.1.4 Van der Waals heterostructures of Graphene and MoS_2

Figure 4.8 shows Raman and UV-vis spectra from a heterostructure of graphene and MoS_2. The graphene and MoS_2 were deposited on the glass slide by the liquid interface deposition method. By depositing MoS_2 on graphene through repetition of the method described earlier, we have seen that no damage is done to the previously deposited layer and successful deposition of both layers resulted in the expected heterostructure. The presence of

both layers was confirmed by the Raman spectroscopy. The Raman spectrum of heterostructure shows the presence of Raman modes of MoS_2 along with the *D*, *G* and 2*D* peaks from graphene.

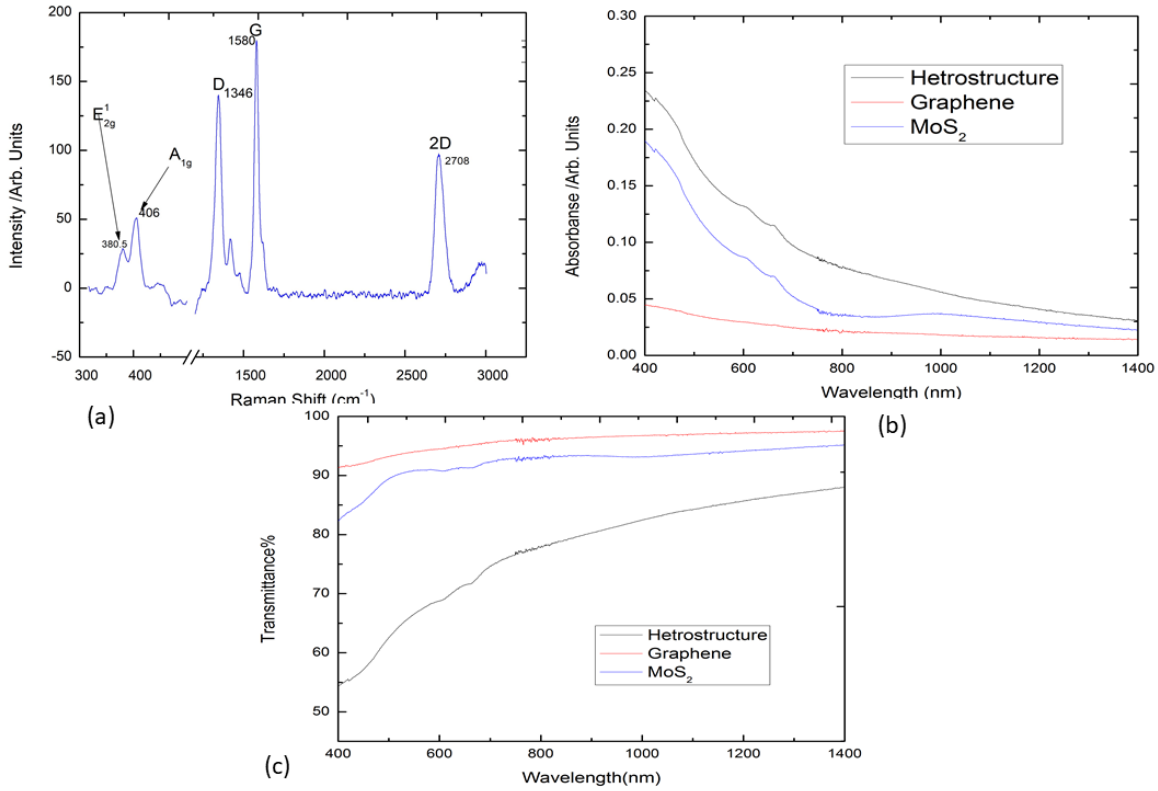

FIGURE 4.8: *(a) Raman spectrum of a heterostructure of graphene and MoS_2: (b) Absorption spectrum of the graphene, MoS_2 and their heterostructure; (c) Transmission spectrum of graphene, MoS_2 and their heterostructure.*

A transmission spectrum was taken for graphene and MoS_2 from the places on glass slide where individual layers do not overlap and then the spectrum again taken from the overlapped layers of graphene and MoS_2 forming the heterostructure. All three spectra are plotted and shown in figure 4.8(c). The spectrum of the heterostructure lies well below the spectrum of individual films which indicates the stacking of films at that particular location. Similarly, the absorption spectrum is also shown in figure 4.8 (b) and shows nearly same relationship. These results indicate that liquid interface dipping is capable of producing thin films which can be stacked in form of the heterostructures. Although the Raman and UV-vis spectroscopy indicate the presence of heterostructure, further characterisation by X-ray Reflectivity (XRR) and atomic force microscopy (AFM) required. Moreover, measurement of the thickness of individual layers and the quality of the deposited heterostructure are recomended for future work.

4.2 Conclusions

In this chapter the inverse dipping approach for deposition of thin films at a liquid-liquid interface - "Dipping LID" - has been succefully demonstrated. Films of a variety of 2DLMs of controllable thickness and excellent continuity have been demonstrated. Films of graphene, *h*-BN and $MoSe_2$ were also successfully deposited on silicon using inverse dipping. Thin films can also be deposited on Al and Cu by slightly varing the dipping procedure as described in appendix B. Hence it can be deduced that the deposition of large area thin films is possible using LID via inverse dipping and pouring with controlled thickness and continuity on various substrates. Furthermore, the LID is highly suitable method for constructing vdWHs, as confirmed by Raman and optical spectroscopy measurements. In order to develop the technique further optimization is required, for example by the development of a stable automated dipping system which should avoid some issues associated with film continuity which have arisen during deposition. In addition to the improvement of the film continuity and reduction of pinhole density, surface and (in the case of heterostructures) interface roughness needs to be measured and monitored, as this is likely to be a key parameter influencing the performance of any device produced by this route. Finally, electrical characterisation and optimisation of transport properties through improvements to the precursor materials and deposition approach is a necessity for any device applications of films and heterostructures produced by the methods reported here.

Chapter 5

Further Work

The aim of the research work reported in this thesis was to prove in principle that interface-based techniques could be used to deposit thin films of two-dimensional layered materials (2DLMs) in a controlled fashion. During the project a new method of film deposition, Liquid Interface Deposition (LID), was developed and the production of thin films and heterostructures by this technique was demonstrated. The work presented here has opened up new horizons that go well beyond the original scope of the thesis and there are many profitable directions in which future work can be taken.

In Chapter 3 shear exfoliation of 2DLMs was studied and, whilst preliminary results strongly indicate that the exfoliation process is influenced by the solvent viscosity, a more complete study is required to confirm this conclusion. It is suggested that a broader range of viscosities be achieved in the aqueous suspensions by undertaking measurements more temperature points for pure water and for further glycerol:water mixtures. In particular, the overlap between the two solvents should be made relatively large – agreement in the concentration of suspensions produced at the same viscosity by the two different routes for multiple viscosities will provide strong proof of the importance of this parameter.

It is expected that varying the viscosity of the exfoliation solvent may also influence the thickness of the 2DLM platelets. As described in Chapter 3, it is possible to determine the platelet thickness with Raman spectroscopy. Exfoliation at room temperature was found to produce predominantly trilayer material and it would be of great interest to discover whether other thicknesses predominate under differing conditions. Finally, the study of shear exfoliation was mainly focussed on graphene and an examination of the influence of viscosity and time on the shear exfoliation of other 2DLMs is necessary to discover how transferable the results from graphene might be.

In Chapter 4, the deposition of thin films and heterostructures of 2DLMs was presented. Although the LID method is proved in principle, there are still a variety of routes by which it may be optimised. For example, an automated, stable systems for inverse dipping should substantially improve film reproducibility and avoid film damage during the transfer process. It would be possible to use an automated system to explore the influence of dipping speed and insertion angle on the deposition process, which initial experiments indicate may be of importance. Other 'seperation solvents' than DCM can be tested to improve the quality of films and optimise the procedure. The influence of the precursor suspension of 2DLM platelets is also yet to be explored and materials produced by other exfoliation techniques

such as sonication and microfluidization [175] could be deposited using LID and characterised to get the best combination of exfoliation and deposition methods.

The films produced by LID consist of overlapping platelets of the 2DLMs and electrical characterisation is required to determine the conductivity and charge carrier mobility in these films. These would be important measurements to make, as the potential applications of the LID films and heterostructures will depend strongly on their electrical quality. Surface and interfacial roughness is also a key parameter determining device performance. Some preliminary X-Ray Reflectivity measurements (not reported in the thesis) have been made on heterostructures and the further use of XRR will be extremely important to characterise the buried interfaces formed in these materials. Atomic Force Microscopy can also be a valuable, at least for surface (rather than interface) roughness measurements and has the advantage of both high spatial resolution and direct imaging. Similarly, Raman mapping of films and heterostructures could provide rich information on the presence of defects, doping and interlayer interaction which have not been touched upon in any detail in this work.

Appendix A

Materials Specification

The table A.1 gives the specifications of the materials used in this work.

TABLE A.1: The starting materials used in this work

substance	Purity[a]	Particle Size[a]	Type	Product ID
Graphite	-	+100 mesh	flakes	332461
MoS_2	98.5%	6μm	powder	69860
$MoSe_2$	99%	-325 mesh	powder	778087
WS_2	99%	2 μm	powder	243639
h-BN	98%	1μm	powder	255475
Triton X-100	>97%	-	liquid	234729
Glycerol	>99%	-	liquid	134872

a As given by supplier's specification (Sigma Aldrich)

Appendix B

Liquid Interface Deposition via Pouring

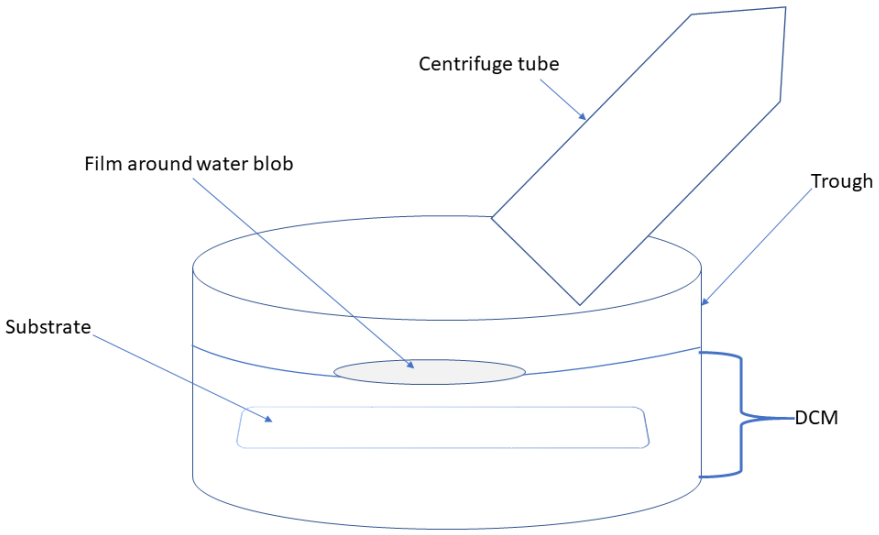

FIGURE B.1: *Schematic illustration of the deposition from liquid interface via pouring*

Figure B.1 provides a schematic of the approach to deposition via pouring. This technique has also been used successfully to deposit the stable film on a substrate from a 'blob' of water (see chapter 4). This approach could be described as a modified form of the LB method as the film is deposited from liquid interfaces instead of liquid -air interface. The trough must be filled with DCM in such quantity that it holda the water blob to float on the surface as is it is seen that blob quickly sinks and film attaches to the base of trough or substrate underneath. Furthermore, a glass trough cannot be used as it attracts the water blob hence films quickly stick to the side walls of trough. If the substrate is lifted up horizontally, it is seen that the film can be transferred to it by applying this technique. The film can be deposited on a specific region by this method, which is useful for creation of vdWHs.

Bibliography

1. Novoselov, K. S. *et al.* Electric field effect in atomically thin carbon films. *Science* **306,** 666–669 (2004).
2. Geim, A. K. & Novoselov, K. S. The rise of graphene. *Nature Materials* **6,** 183–191 (2007).
3. Mermin, N. D. Crystalline order in two dimensions. *Physical Review* **176,** 250 (1968).
4. Fasolino, A., Los, J. & Katsnelson, M. I. Intrinsic ripples in graphene. *arXiv preprint arXiv:0704.1793* (2007).
5. Venables, J., Spiller, G. & Hanbucken, M. Nucleation and growth of thin films. *Reports on Progress in Physics* **47,** 399 (1984).
6. Evans, J., Thiel, P. & Bartelt, M. C. Morphological evolution during epitaxial thin film growth: Formation of 2D islands and 3D mounds. *Surface Science Reports* **61,** 1–128 (2006).
7. Dresselhaus, M. S. & Araujo, P. T. *Perspectives on the 2010 Nobel Prize in Physics for graphene* 2010.
8. Xu, M., Liang, T., Shi, M. & Chen, H. Graphene-like two-dimensional materials. *Chemical Reviews* **113,** 3766–3798 (2013).
9. Wilson, J. & Yoffe, A. The transition metal dichalcogenides discussion and interpretation of the observed optical, electrical and structural properties. *Advances in Physics* **18,** 193–335 (1969).
10. Butler, S. Z. *et al.* Progress, challenges, and opportunities in two-dimensional materials beyond graphene. *ACS Nano* **7,** 2898–2926 (2013).
11. Hozoi, L., Siurakshina, L., Fulde, P. & Van Den Brink, J. Ab Initio determination of Cu 3d orbital energies in layered copper oxides. *Scientific Reports* **1** (2011).
12. Osada, M. & Sasaki, T. Two-Dimensional Dielectric Nanosheets: Novel Nanoelectronics From Nanocrystal Building Blocks. *Advanced Materials* **24,** 210–228 (2012).
13. Golberg, D. *et al.* Boron nitride nanotubes and nanosheets. *ACS Nano* **4,** 2979–2993 (2010).
14. Kim, K. K. *et al.* Synthesis of monolayer hexagonal boron nitride on Cu foil using chemical vapor deposition. *Nano Letters* **12,** 161–166 (2011).
15. Kong, D. *et al.* Few-layer nanoplates of Bi_2Se_3 and Bi_2Te_3 with highly tunable chemical potential. *Nano Letters* **10,** 2245–2250 (2010).
16. Liu, D. *et al.* Electronic origin of high temperature superconductivity in single-layer FeSe superconductor. *arXiv preprint arXiv:1202.5849* (2012).

17. Tang, H., Liang, D., Qiu, R. L. & Gao, X. P. Two-dimensional transport-induced linear magneto-resistance in topological insulator Bi_2Se_3 nanoribbons. *ACS Nano* **5,** 7510–7516 (2011).

18. Zhang, H. *et al.* Topological insulators in Bi_2Se_3, Bi_2Te_3 and Sb_2Te_3 with a single Dirac cone on the surface. *Nature Physics* **5,** 438 (2009).

19. Antunez, P. D., Buckley, J. J. & Brutchey, R. L. Tin and germanium monochalcogenide IV-VI semiconductor nanocrystals for use in solar cells. *Nanoscale* **3,** 2399–2411 (2011).

20. Do, D. T., Mahanti, S. D. & Lai, C. W. Spin splitting in 2D monochalcogenide semiconductors. *Scientific Reports* **5** (2015).

21. Fogel, N. Y. *et al.* Interfacial superconductivity in semiconducting monochalcogenide superlattices. *Physical Review B* **66,** 174513 (2002).

22. Li, W. & Li, J. Piezoelectricity in two-dimensional group-III monochalcogenides. *Nano Research* **8,** 3796–3802 (2015).

23. Zhuang, H. L. & Hennig, R. G. Single-layer group-III monochalcogenide photocatalysts for water splitting. *Chemistry of Materials* **25,** 3232–3238 (2013).

24. Balendhran, S., Walia, S., Nili, H., Sriram, S. & Bhaskaran, M. Elemental analogues of graphene: Silicene, Germanene, Stanene, and Phosphorene. *Small* **11,** 640–652 (2015).

25. Dávila, M., Xian, L., Cahangirov, S, Rubio, A. & Le Lay, G. Germanene: a novel two-dimensional germanium allotrope akin to graphene and silicene. *New Journal of Physics* **16,** 095002 (2014).

26. Mortazavi, B., Dianat, A., Cuniberti, G. & Rabczuk, T. Application of silicene, germanene and stanene for Na or Li ion storage: A theoretical investigation. *Electrochimica Acta* **213,** 865–870 (2016).

27. Xia, F., Wang, H. & Jia, Y. Rediscovering black phosphorus as an anisotropic layered material for optoelectronics and electronics. *Nature Communications* **5,** 4458 (2014).

28. Mas-Balleste, R., Gomez-Navarro, C., Gomez-Herrero, J. & Zamora, F. 2D materials: to graphene and beyond. *Nanoscale* **3,** 20–30 (2011).

29. Pop, E., Varshney, V. & Roy, A. K. Thermal properties of graphene: Fundamentals and applications. *MRS Bulletin* **37,** 1273–1281 (2012).

30. Kholmanov, I. N. *et al.* Improved electrical conductivity of graphene films integrated with metal nanowires. *Nano Letters* **12,** 5679–5683 (2012).

31. Geim, A. K. & Grigorieva, I. V. Van der Waals heterostructures. *Nature* **499,** 419–425 (2013).

32. Novoselov, K., Mishchenko, A, Carvalho, A & Neto, A. C. 2D materials and van der Waals heterostructures. *Science* **353,** aac9439 (2016).

33. Bonaccorso, F., Sun, Z., Hasan, T. & Ferrari, A. C. Graphene photonics and optoelectronics. *Nat Photon* **4.** 10.1038/nphoton.2010.186, 611–622 (2010).

34. Lopez-Sanchez, O., Lembke, D., Kayci, M., Radenovic, A. & Kis, A. Ultrasensitive photodetectors based on monolayer MoS_2. *Nature Nanotechnology* **8,** 497–501 (2013).

35. Du, F. *et al.* Preparation of tunable 3D pillared carbon nanotube–graphene networks for high-performance capacitance. *Chemistry of Materials* **23,** 4810–4816 (2011).

36. Fujita, D. Nanoscale synthesis and characterization of graphene-based objects. *Science and Technology of Advanced Materials* **12,** 044611 (2011).

37. Park, J. *et al.* Epitaxial graphene growth by carbon molecular beam epitaxy (CMBE). *Advanced Materials* **22,** 4140–4145 (2010).

38. Ma, Y. *et al.* Electronic and magnetic properties of perfect, vacancy-doped, and non-metal adsorbed MoSe 2, MoTe 2 and WS 2 monolayers. *Physical Chemistry Chemical Physics* **13,** 15546–15553 (2011).

39. Neto, A. C., Guinea, F. & Peres, N. M. Drawing conclusions from graphene. *Physics World* **19,** 33 (2006).

40. Bao, C. *et al.* Stacking-dependent electronic structure of trilayer graphene resolved by nanospot angle-resolved photoemission spectroscopy. *Nano Letters* **17,** 1564–1568 (2017).

41. Garlow, J. A. *et al.* Large-area growth of turbostratic graphene on Ni (111) via physical vapor deposition. *Scientific Reports* **6,** 19804 (2016).

42. Bernal, J. D. The Structure of Graphite. *Proceedings of the Royal Society of London. Series A, Containing Papers of a Mathematical and Physical Character* **106,** 749–773 (1924).

43. Malard, L., Pimenta, M., Dresselhaus, G & Dresselhaus, M. Raman spectroscopy in graphene. *Physics Reports* **473,** 51–87 (2009).

44. Lipson, H & Stokes, A. *The structure of graphite* in *Proceedings of the Royal Society of London A: Mathematical, Physical and Engineering Sciences* **181** (The Royal Society), 101–105.

45. Mak, K. F., Shan, J. & Heinz, T. F. Electronic structure of few-layer graphene: experimental demonstration of strong dependence on stacking sequence. *Physical Review Letters* **104,** 176404 (2010).

46. Wallace, P. R. The band theory of graphite. *Physical Review* **71,** 622 (1947).

47. Peierls, R. Quelques proprietes typiques des corpses solides. *Ann. IH Poincare* **5,** 177–222 (1935).

48. McClure, J. Energy band structure of graphite. *IBM Journal of Research and Development* **8,** 255–261 (1964).

49. Yamazaki, M. Electronic Band Structure in Graphite. *The Journal of Chemical Physics* **26,** 930–934 (1957).

50. Biró, L. P., Nemes-Incze, P. & Lambin, P. Graphene: nanoscale processing and recent applications. *Nanoscale* **4,** 1824–1839 (2012).

51. Neto, A. C., Guinea, F, Peres, N. M., Novoselov, K. S. & Geim, A. K. The electronic properties of graphene. *Reviews of Modern Physics* **81,** 109 (2009).
52. Allen, M. J., Tung, V. C. & Kaner, R. B. Honeycomb carbon: a review of graphene. *Chemical Reviews* **110,** 132–145 (2009).
53. Kalita, G. & Tanemura, M. in *Graphene Materials - Advanced Applications* (eds Kyzas, G. Z. & Mitropoulos, A. C.) Ch. 03 (InTech, Rijeka, 2017).
54. Novoselov, K. S. *et al.* Two-dimensional gas of massless Dirac fermions in graphene. *arXiv preprint cond-mat/0509330* (2005).
55. Morozov, S. *et al.* Giant intrinsic carrier mobilities in graphene and its bilayer. *Physical Review Letters* **100,** 016602 (2008).
56. Nair, R. R. *et al.* Fine structure constant defines visual transparency of graphene. *Science* **320,** 1308–1308 (2008).
57. Lee, C., Wei, X., Kysar, J. W. & Hone, J. Measurement of the elastic properties and intrinsic strength of monolayer graphene. *Science* **321,** 385–388 (2008).
58. Pierson, H. O. *Handbook of carbon, graphite, diamonds and fullerenes: processing, properties and applications* (William Andrew, 2012).
59. Geim, A. K. Graphene: status and prospects. *Science* **324,** 1530–1534 (2009).
60. Dikin, D. A. *et al.* Preparation and characterization of graphene oxide paper. *Nature* **448,** 457 (2007).
61. Elias, D. C. *et al.* Control of graphene's properties by reversible hydrogenation: evidence for graphane. *Science* **323,** 610–613 (2009).
62. Nair, R. R. *et al.* Fluorographene: A two-dimensional counterpart of Teflon. *Small* **6,** 2877–2884 (2010).
63. Balandin, A. A. *et al.* Superior thermal conductivity of single-layer graphene. *Nano Letters* **8,** 902–907 (2008).
64. Bunch, J. S. *et al.* Impermeable atomic membranes from graphene sheets. *Nano Letters* **8,** 2458–2462 (2008).
65. Lin, Y.-M. *et al.* 100-GHz transistors from wafer-scale epitaxial graphene. *Science* **327,** 662–662 (2010).
66. Ye, S. *et al.* Electro-absorption optical modulator using dual-graphene-on-graphene configuration. *Optics Express* **22,** 26173–26180 (2014).
67. Kim, K. S. *et al.* Large-scale pattern growth of graphene films for stretchable transparent electrodes. *Nature* **457,** 706 (2009).
68. Deng, M. *et al.* Electrochemical deposition of polypyrrole/graphene oxide composite on microelectrodes towards tuning the electrochemical properties of neural probes. *Sensors and Actuators B: Chemical* **158,** 176–184 (2011).

69. Yang, X. *et al.* Graphene uniformly decorated with gold nanodots: in situ synthesis, enhanced dispersibility and applications. *Journal of Materials Chemistry* **21,** 8096–8103 (2011).

70. Novoselov, K. S. *et al.* A roadmap for graphene. *Nature* **490,** 192–200 (2012).

71. Joshi, R. *et al.* Precise and ultrafast molecular sieving through graphene oxide membranes. *Science* **343,** 752–754 (2014).

72. Wang, J., Ma, F. & Sun, M. Graphene, hexagonal boron nitride, and their heterostructures: properties and applications. *RSC Advances* **7,** 16801–16822 (2017).

73. Pacile, D, Meyer, J., Girit, & Zettl, A. The two-dimensional phase of boron nitride: few-atomic-layer sheets and suspended membranes. *Applied Physics Letters* **92,** 133107 (2008).

74. Watanabe, K., Taniguchi, T. & Kanda, H. Direct-bandgap properties and evidence for ultraviolet lasing of hexagonal boron nitride single crystal. *Nature Materials* **3,** 404 (2004).

75. Lee, K. H. *et al.* Large-scale synthesis of high-quality hexagonal boron nitride nanosheets for large-area graphene electronics. *Nano Letters* **12,** 714–718 (2012).

76. Dean, C. R. *et al.* Boron nitride substrates for high-quality graphene electronics. *Nature Nanotechnology* **5,** 722–726 (2010).

77. Lee, C. *et al.* Frictional characteristics of atomically thin sheets. *Science* **328,** 76–80 (2010).

78. Laursen, A. B., K, S., Dahl, S. & Chorkendorff, I. Molybdenum sulfides—efficient and viable materials for electro-and photoelectrocatalytic hydrogen evolution. *Energy and Environmental Science* **5,** 5577–5591 (2012).

79. Puthussery, J., Seefeld, S., Berry, N., Gibbs, M. & Law, M. Colloidal iron pyrite (FeS_2) nanocrystal inks for thin-film photovoltaics. *Journal of the American Chemical Society* **133,** 716–719 (2010).

80. Feng, J. *et al.* Metallic few-layered VS_2 ultrathin nanosheets: high two-dimensional conductivity for in-plane supercapacitors. *Journal of the American Chemical Society* **133,** 17832–17838 (2011).

81. Chatzitheodorou, G, Fiechter, S, Kunst, M, Luck, J & Tributsch, H. Low temperature chemical preparation of semiconducting transition metal chalcogenide films for energy conversion and storage, lubrication and surface protection. *Materials Research Bulletin* **23,** 1261–1271 (1988).

82. Tang, X. *et al.* Preparation and thermoelectric transport properties of high-performance p-type $Bi_2Te_3$with layered nanostructure. *Applied Physics Letters* **90,** 012102 (2007).

83. Min, Y. *et al.* Solution-based synthesis of anisotropic metal chalcogenide nanocrystals and their applications. *Journal of Materials Chemistry C* **2,** 6222–6248 (2014).

84. Gourmelon, E *et al.* MS_2 (M= W, Mo) photosensitive thin films for solar cells. *Solar Energy Materials and Solar Cells* **46,** 115–121 (1997).

85. Splendiani, A. *et al.* Emerging Photoluminescence in monolayer MoS_2. *Nano Letters* **10,** 1271–1275 (2010).

86. Mak, K. F., Lee, C., Hone, J., Shan, J. & Heinz, T. F. Atomically thin MoS_2: a new direct-gap semiconductor. *Physical Review Letters* **105,** 136805 (2010).

87. He, Z. & Que, W. Molybdenum disulfide nanomaterials: structures, properties, synthesis and recent progress on hydrogen evolution reaction. *Applied Materials Today* **3,** 23–56 (2016).

88. Kuc, A., Zibouche, N. & Heine, T. Influence of quantum confinement on the electronic structure of the transition metal sulfide T S 2. *Physical Review B* **83,** 245213 (2011).

89. Li, T. & Galli, G. Electronic properties of MoS_2 nanoparticles. *The Journal of Physical Chemistry C* **111,** 16192–16196 (2007).

90. Coehoorn, R, Haas, C & De Groot, R. Electronic structure of $MoSe_2$, MoS_2, and WSe_2. II. The nature of the optical band gaps. *Physical Review B* **35,** 6203 (1987).

91. Yun, W. S., Han, S., Hong, S. C., Kim, I. G. & Lee, J. Thickness and strain effects on electronic structures of transition metal dichalcogenides: 2H-MX_2 semiconductors (M= Mo, W; X= S, Se, Te). *Physical Review B* **85,** 033305 (2012).

92. Yin, Z. *et al.* Single-layer MoS_2 phototransistors. *ACS Nano* **6,** 74–80 (2011).

93. Li, H. *et al.* Fabrication of single-and multilayer MoS_2 film-based field-effect transistors for sensing NO at room temperature. *Small* **8,** 63–67 (2012).

94. Tongay, S., Varnoosfaderani, S. S., Appleton, B. R., Wu, J. & Hebard, A. F. Magnetic properties of MoS_2: existence of ferromagnetism. *Applied Physics Letters* **101,** 123105 (2012).

95. Tongay, S. *et al.* Thermally driven crossover from indirect toward direct bandgap in 2D semiconductors: $MoSe_2$ versus MoS_2. *Nano Letters* **12,** 5576–5580 (2012).

96. König, M. *et al.* Quantum spin Hall insulator state in HgTe quantum wells. *Science* **318,** 766–770 (2007).

97. Fei, R., Li, W., Li, J. & Yang, L. Giant piezoelectricity of monolayer group IV monochalcogenides: SnSe, SnS, GeSe, and GeS. *Applied Physics Letters* **107,** 173104 (2015).

98. Bertolazzi, S., Brivio, J. & Kis, A. Stretching and breaking of ultrathin MoS_2. *ACS Nano* **5,** 9703–9709 (2011).

99. Bonaccorso, F. *et al.* Production and processing of graphene and 2d crystals. *Materials Today* **15,** 564–589 (2012).

100. Albaugh, K. B. Electrode phenomena during anodic bonding of silicon to sodium borosilicate glass. *Journal of the Electrochemical Society* **138,** 3089–3094 (1991).

101. Henmi, H, Shoji, S, Shoji, Y, Yoshimi, K & Esashi, M. Vacuum packaging for microsensors by glass-silicon anodic bonding. *Sensors and Actuators A: Physical* **43,** 243–248 (1994).

102. Moldt, T. *et al.* High-yield production and transfer of graphene flakes obtained by anodic bonding. *ACS Nano* **5,** 7700–7706 (2011).

103. Shukla, A., Kumar, R., Mazher, J. & Balan, A. Graphene made easy: High quality, large-area samples. *Solid State Communications* **149,** 718–721 (2009).

104. Gacem, K., Boukhicha, M., Chen, Z. & Shukla, A. High quality 2D crystals made by anodic bonding: a general technique for layered materials. *Nanotechnology* **23,** 505709 (2012).

105. Lee, K. & Ye, J. Significantly improved thickness uniformity of graphene monolayers grown by chemical vapor deposition by texture and morphology control of the copper foil substrate. *Carbon* **100,** 441–449 (2016).

106. Li, X. *et al.* Large-area synthesis of high-quality and uniform graphene films on copper foils. *Science* **324,** 1312–1314 (2009).

107. Han, G. H. *et al.* Influence of copper morphology in forming nucleation seeds for graphene growth. *Nano Letters* **11,** 4144–4148 (2011).

108. Cambaz, Z. G., Yushin, G., Osswald, S., Mochalin, V. & Gogotsi, Y. Noncatalytic synthesis of carbon nanotubes, graphene and graphite on SiC. *Carbon* **46,** 841–849 (2008).

109. Park, J. *et al.* Epitaxial graphene growth by carbon molecular beam epitaxy (CMBE). *Advanced Materials* **22,** 4140–4145 (2010).

110. Garcia, J. M. *et al.* Graphene growth on h-BN by molecular beam epitaxy. *Solid State Communications* **152,** 975–978 (2012).

111. Lalmi, B. *et al.* Epitaxial growth of a silicene sheet. *Applied Physics Letters* **97,** 223109 (2010).

112. Song, C.-L. *et al.* Topological insulator Bi_2Se_3 thin films grown on double-layer graphene by molecular beam epitaxy. *Applied Physics Letters* **97,** 143118 (2010).

113. Yu, Y. *et al.* Molecular beam epitaxy growth of atomically ultrathin $MoTe_2$ lateral heterophase homojunctions on graphene substrates. *Carbon* **115,** 526–531 (2017).

114. Lotya, M. *et al.* Liquid phase production of graphene by exfoliation of graphite in surfactant/water solutions. *Journal of the American Chemical Society* **131,** 3611–3620 (2009).

115. Chen, J. *et al.* A binary solvent system for improved liquid phase exfoliation of pristine graphene materials. *Carbon* **94,** 405–411 (2015).

116. Bourlinos, A. B. *et al.* Aqueous-phase exfoliation of graphite in the presence of polyvinylpyrrolidone for the production of water-soluble graphenes. *Solid State Communications* **149,** 2172–2176 (2009).

117. Hernandez, Y. *et al.* High-yield production of graphene by liquid-phase exfoliation of graphite. *Nature Nanotechnology* **3,** 563–568 (2008).

118. Khan, U., O'Neill, A., Lotya, M., De, S. & Coleman, J. N. High-Concentration Solvent Exfoliation of Graphene. *Small* **6,** 864–871 (2010).

119. Paton, K. R. *et al.* Scalable production of large quantities of defect-free few-layer graphene by shear exfoliation in liquids. *Nature Materials* **13,** 624–630 (2014).

120. Varrla, E. *et al.* Large-scale production of size-controlled MoS_2 nanosheets by shear exfoliation. *Chemistry of Materials* **27,** 1129–1139 (2015).

121. Varrla, E. *et al.* Turbulence-assisted shear exfoliation of graphene using household detergent and a kitchen blender. *Nanoscale* **6,** 11810–11819 (2014).

122. Mathieson, A. G. Reclaiming the third dimension for 2D materials: Developing simple approaches for the creation of heterostructures. *MPhy thesis, Durham University* (2017).

123. Paredes, J. *et al.* Environmentally friendly approaches toward the mass production of processable graphene from graphite oxide. *Journal of Materials Chemistry* **21,** 298–306 (2011).

124. Kim, H. *et al.* Optoelectronic properties of graphene thin films deposited by a Langmuir-Blodgett assembly. *Nanoscale* **5** (2013).

125. Gengler, R. Y. *et al.* Large-Yield Preparation of High-Electronic-Quality Graphene by a Langmuir–Schaefer Approach. *Small* **6,** 35–39 (2010).

126. Petty, M. C. *Langmuir-Blodgett films : an introduction* (Cambridge New York : Cambridge University Press, Cambridge New York, 1996).

127. Martin, P. & Szablewski, M. Langmuir-Blodgett Systems. *Nima Technology, Trough operating manual, Warwick, UK* (1992).

128. Li, C., Zhou, P. & Zhang, D. W. Devices and applications of van der Waals heterostructures. *Journal of Semiconductors* **38,** 031005 (2017).

129. Liu, Y. *et al.* Van der Waals heterostructures and devices. *Nature Reviews Materials* **1,** 16042 (2016).

130. Yu, G. *et al.* Interaction phenomena in graphene seen through quantum capacitance. *Proceedings of the National Academy of Sciences* **110,** 3282–3286 (2013).

131. Li, Q., Liu, M., Zhang, Y. & Liu, Z. Hexagonal Boron Nitride–Graphene Heterostructures: Synthesis and Interfacial Properties. *Small* **12,** 32–50 (2016).

132. Song, X. *et al.* Graphene/h-BN Heterostructures: Recent Advances in Controllable Preparation and Functional Applications. *Advanced Energy Materials* **6** (2016).

133. Choi, M. S. *et al.* Controlled charge trapping by molybdenum disulphide and graphene in ultrathin heterostructured memory devices. *Nature Communications* **4,** 1624 (2013).

134. Mishchenko, A. *et al.* Twist-controlled resonant tunnelling in graphene/boron nitride/graphene heterostructures. *Nature Nanotechnology* **9,** 808–813 (2014).

135. Lin, Y.-C. *et al.* Atomically thin resonant tunnel diodes built from synthetic van der Waals heterostructures. *Nature Communications* **6** (2015).

136. Britnell, L. *et al.* Strong light-matter interactions in heterostructures of atomically thin films. *Science* **340,** 1311–1314 (2013).

137. Wang, F. *et al.* Tunable GaTe-MoS_2 van der Waals p–n junctions with novel optoelectronic performance. *Nano Letters* **15,** 7558–7566 (2015).

138. Long, M. *et al.* Broadband photovoltaic detectors based on an atomically thin heterostructure. *Nano Letters* **16,** 2254–2259 (2016).

139. Smekal, A. Zur quantentheorie der dispersion. *Naturwissenschaften* **11,** 873–875 (1923).

140. Raman, C. V. & Krishnan, K. S. A new type of secondary radiation. *Nature* **121,** 501–502 (1928).

141. Smith, E. & Dent, G. *Modern Raman spectroscopy: a practical approach* 2–3 (John Wiley and Sons, 2013).

142. Gilson, T. R. & Hendra, P. J. *Laser Raman spectroscopy: a survey of interest primarily to chemists, and containing a comprehensive discussion of experiments on crystals* (John Wiley and Sons, 1970).

143. Cardona, M. & Peter, Y. Y. *Fundamentals of semiconductors* (Springer, 2005).

144. Ferraro, J. R. *Introductory Raman Spectroscopy* (Academic Press, 2003).

145. Dresselhaus, M., Jorio, A & Saito, R. Characterizing graphene, graphite, and carbon nanotubes by Raman spectroscopy. *Annu. Rev. Condens. Matter Phys.* **1,** 89–108 (2010).

146. Malard, L., Pimenta, M., Dresselhaus, G & Dresselhaus, M. Raman Spectroscopy in graphene. *Physics Reports* **473,** 51–87 (2009).

147. Nguyen, T. A., Lee, J.-U., Yoon, D. & Cheong, H. Excitation energy dependent Raman signatures of ABA-and ABC-stacked few-layer graphene. *Scientific reports* **4** (2014).

148. Beams, R., Cançado, L. G. & Novotny, L. Raman characterization of defects and dopants in graphene. *Journal of Physics: Condensed Matter* **27,** 083002 (2015).

149. Das, A. *et al.* Monitoring dopants by Raman scattering in an electrochemically top-gated graphene transistor. *Nature Nanotechnology* **3,** 210–215 (2008).

150. Ferrari, A. C. Raman spectroscopy of graphene and graphite: disorder, electron–phonon coupling, doping and nonadiabatic effects. *Solid State Communications* **143,** 47–57 (2007).

151. Ferrari, A. C. *et al.* Raman spectrum of graphene and graphene layers. *Physical Review Letters* **97,** 187401 (2006).

152. Ferrari, A. C. & Basko, D. M. Raman spectroscopy as a versatile tool for studying the properties of graphene. *Nature Nanotechnology* **8,** 235–246 (2013).

153. Tuinstra, F & Koenig, J. L. Raman spectrum of graphite. *The Journal of Chemical Physics* **53,** 1126–1130 (1970).

154. Yoon, D. *et al.* Interference effect on Raman spectrum of graphene on SiO_2/Si. *Physical Review B* **80,** 125422 (2009).

155. Casiraghi, C, Pisana, S, Novoselov, K., Geim, A. & Ferrari, A. Raman fingerprint of charged impurities in graphene. *Applied Physics Letters* **91,** 233108 (2007).

156. Park, J. *et al.* G' band Raman spectra of single, double and triple layer graphene. *Carbon* **47,** 1303–1310 (2009).

157. Eckmann, A. *et al.* Probing the nature of defects in graphene by Raman spectroscopy. *Nano Letters* **12,** 3925–3930 (2012).

158. Li, H. *et al.* From bulk to monolayer MoS_2: evolution of Raman scattering. *Advanced Functional Materials* **22,** 1385–1390 (2012).

159. Lee, C. *et al.* Anomalous lattice vibrations of single-and few-layer MoS_2. *Acs Nano* **4,** 2695–2700 (2010).

160. Zhao, Y. *et al.* Interlayer breathing and shear modes in few-trilayer MoS_2 and WSe_2. *Nano Letters* **13,** 1007–1015 (2013).

161. Tonndorf, P. *et al.* Photoluminescence emission and Raman response of monolayer MoS_2, $MoSe_2$, and WSe_2. *Optics Express* **21,** 4908–4916 (2013).

162. Zeng, H. *et al.* Optical signature of symmetry variations and spin-valley coupling in atomically thin tungsten dichalcogenides. *Scientific Reports* **3** (2013).

163. Zhou, W., Apkarian, R., Wang, Z. L. & Joy, D. in *Scanning microscopy for nanotechnology* 1–40 (Springer, 2006).

164. Bogner, A., Jouneau, P.-H., Thollet, G., Basset, D & Gauthier, C. A history of scanning electron microscopy developments: towards "wet-STEM" imaging. *Micron* **38,** 390–401 (2007).

165. Egerton, R. F. *Physical principles of electron microscopy* (Springer, 2005).

166. Goldstein, J. I. *Scanning electron microscopy and x-ray microanalysis : a text for biologists, materials scientists, and geologists* (New York : Plenum, New York, 1981).

167. Goodhew, P. J., Humphreys, J. & Beanland, R. *Electron microscopy and analysis* (CRC Press, 2000).

168. Yang, F. *et al.* A facile method to observe graphene growth on copper foil. *Nanotechnology* **23,** 475705 (2012).

169. Alluqmani, S. Growth and doping of Carbon Nanotubes and Graphene. *PhD Thesis, Durham University* (2014).

170. Parka, B. Reclaiming the third dimension for 2D materials: Developing simple approaches for the creation of heterostructures. *MPhys Thesis, Durham University* (2016).

171. Pérez, J. S., Porcel, E. R., López, J. C., Sevilla, J. F. & Chisti, Y. Shear rate in stirred tank and bubble column bioreactors. *Chemical Engineering Journal* **124,** 1–5 (2006).

172. Li, X. *et al.* Highly conducting graphene sheets and Langmuir–Blodgett films. *Nature Nanotechnology* **3,** 538–542 (2008).

173. Balasingam, S. K., Lee, J. S. & Jun, Y. Few-layered $MoSe_2$ nanosheets as an advanced electrode material for supercapacitors. *Dalton Transactions* **44,** 15491–15498 (2015).

174. Wang, K. *et al.* Broadband ultrafast nonlinear absorption and nonlinear refraction of layered molybdenum dichalcogenide semiconductors. *Nanoscale* **6,** 10530–10535 (2014).

175. Karagiannidis, P. G. *et al.* Microfluidization of graphite and formulation of graphene-based conductive inks. *ACS Nano* **11,** 2742–2755 (2017).